Chapter 12

Integrating InSAR and Landsat for Strategic Heritage Site Protection: EW Ground Analysis and Path Loss in Selinunte Park

* Salvatore Polverino

1. Introducing the central theme: deploying Information Age Warfare in collaboration with the protection of Heritage sites

In the rapidly evolving landscape of the digital age, domains across the spectrum are witnessing profound transformations, with heritage preservation and archaeological research being at a notably significant crossroads. Selinunte, nestled in the south-western confines of Sicily, serves as a vivid emblem of this transformation; this ancient city, not only one of the earliest Greek colonies in Sicily but also renowned for its vast temple ruins, encapsulates the essence of architectural and historical grandeur in the Mediterranean context: with its foundation laid in the seventh century B.C.E., Selinunte saw remarkable growth over the next two centuries along the coasts of southern Sicily.

Selinunte's architectural vestiges, as object of this research, are remarkable in the emerging context of modern Information age dominance: its Temple stands out, not just for its representation of ancient Greek architectural prowess but also as a beacon of the zenith of ancient architectural endeavors and as a beacon of Italian culture towards the tormented events of the Mediterranean and Middle East; its architectural vestiges stand solemnly in their current state of decay: the temple's inner colonnade, adorned with intricate designs, speaks volumes about the era's architectural brilliance and profound religious reverence.

As also focused by Giammusso's pioneering research (2012), for which central to this endeavor is the principle of Information Dominance, hence, beginning with an exhaustive archaeological examination, it delves deep into modern digital exploration, by harnessing tools like laser scanning, image-based modeling, and digital surveying; this convergence of historical insights and advanced techniques aims to breathe life into the temple through virtual anastylosis and digital restoration especially 3D modeling in a cutting-edge imagined context; the 18th and 19th centuries bore witness to a surge in virtual reconstructions, with the enthralling allure of Greek ruins being a significant driving force: these initial reconstructions, though manually crafted, showcased remarkable precision, anchored in comprehensive surveys.

Nonetheless, as we delve deeper into the intricate allure of Selinunte through modern, it becomes increasingly clear that traditional Information methods are insufficient for the demands of our era: in light of the rapid advancements in the modern age, there's an imperative to evolve and integrate contemporary defense and aerospace solutions; while the lessons from past events like earthquakes and battles between civilizations remain invaluable in the matter of visible antagonists, we are now advocated to bolster Heritage Protection by embracing and deploying these Electronic Warfare (EW) methodologies.

Corresponding Author: * Salvatore Polverino
Department Training and Internationalization c/o Ordine Architetti Pianificatori Paesaggisti Conservatori di Napoli e Provincia
Piazzetta Matilde Serao, 7, 80132 Napoli, Italy.
e-mail: formazione@napoli.archiworld.it polverinosalvatore@outlook.com

1.1.   Background, rationale, and relevance of the objective : Selinunte area park in Heritage Modelling

Selinunte's archaeological landscape, uniquely carved by the confluence of two rivers, presents a multifaceted backdrop for detailed research and exploration: the complex design and geological attributes of the park led scholars, particularly Schwellenbach I. et al. (2020), to delineate three distinct research zones within the confines encompassing its temples; these authors elucidated its morphological distinctions, notably the valleys of the Cottone and Modione Rivers, act as natural boundaries, partitioning the park into three separate archaeological segments.

The national borders of Italy, particularly the southern coast of Sicily which faces Libya, represent a sensitive and historically significant domain: Sicily not only holds strategic importance due to its geographical location but is constitutes the characteristic inner texture of Italy's heritage: preserving this area's heritage, given its proximity to another nation and the intersection of cultures, has been overviewed from a state perspective, it has historically served as a key instrument in fostering a cohesive "national" identity (C. Elizabeth and T. Maguire, 2018, M. Craith, 2008).
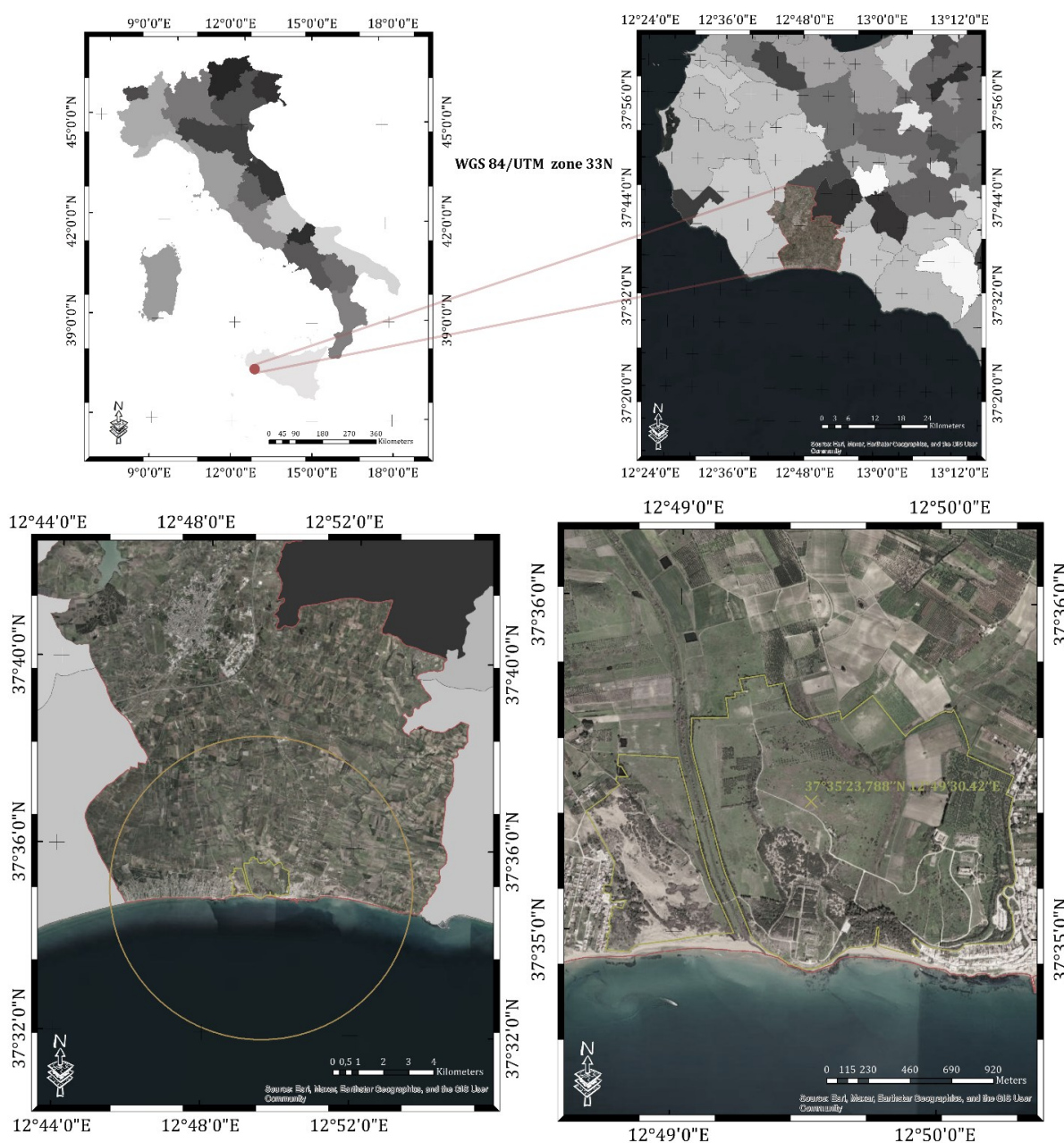
Figures 1: a-b-c-d. Aerial view (Google Earth imagery) priorly determined.

Fig. 2 (left). Arial Perspective: Entrance to the Temple of Selinunte captured via UAV. Credits: CC0 1.0 Universal. **Fig. 3 (right).** Remnants of Time: Scattered Capitals in Selinunte's Archaeological Park. Credits: CC0 1.0 Universal.

1.2. Cultural Heritage at the forefront : unexpected targeting and exploitation of archaeological sites in modern conflicts

Conflicts in recent times have increasingly placed cultural heritage at risk. In the era of cold and hot weapons, battles were characterized by direct confrontations. Recent events introduced to the general public, the concern with little to no direct visibility of each other's positions.

The deliberate targeting and exploitation of control of archaeological sites in contemporary Age Warfare has now shifted to gathering intelligence, managing information and executing precise, long-range strikes using advanced electronic systems: the research scope involved four steps in Electronic Support (ES): I) environmental data gathering, II) signal Time-of-Arrival (TOA) calculations, III) Electronic Intelligence (ELINT), and IV) Electronic Protection (EP).
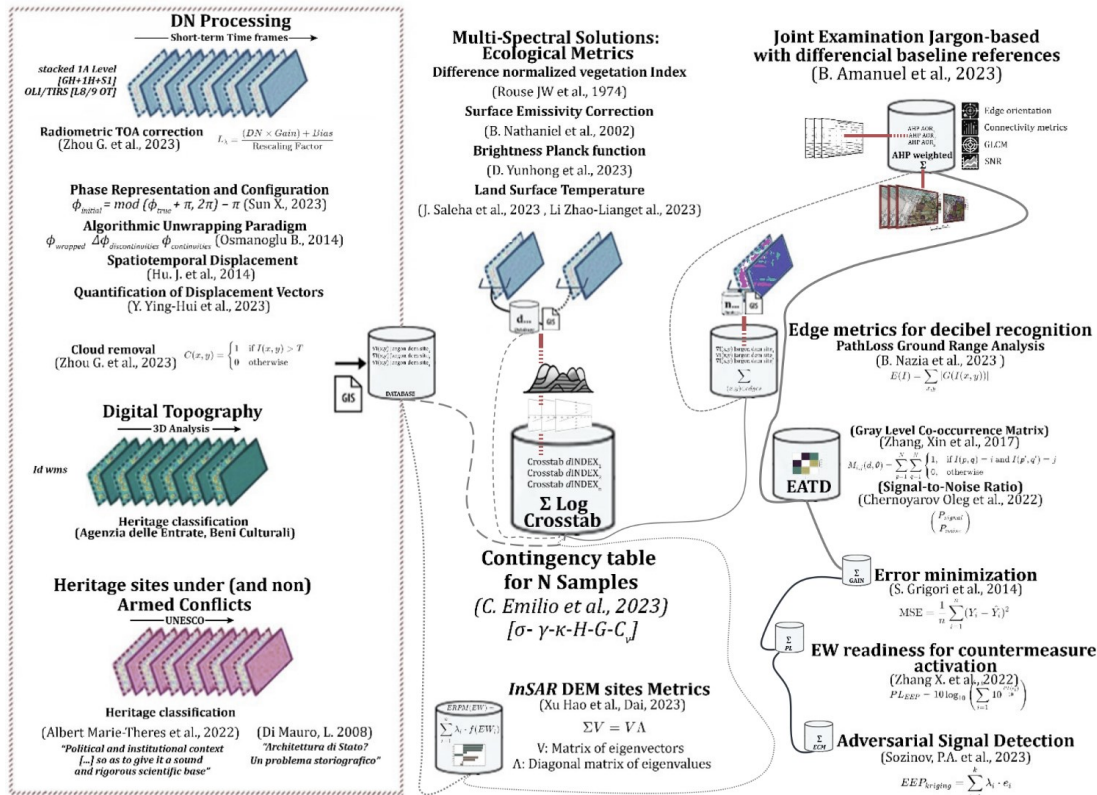

Fig. 4. Methodologies in research across EW doctrines.

2.   Materials and Methods

As underscored by recent studies, notably by Schwellenbach I. et al. (2020), the Digital Terrain Model (DTM) plays a fundamental role in deciphering both Selinunte and its surrounding areas, particularly when considering seismic hazards (Guidoboni E., 2002) and heritage preservation.

Recognizing the importance of seamlessly integrating an updated DEM_REM (Regional Elevation Model) dataset, priority was given to its most accurate version. Version 1.1, established in 2023, was formulated using the Triangulated Irregular Network (TIN) model; this dataset, refined under the guidance of the "*Istituto Nazionale di Geofisica e Vulcanologia*" (INGV) and with a native 10-meter resolution, was subsequently adapted to a 20-meter resolution for windPro processes.

Its vertical precision, as quantified by the RMSE, averages below 3.5 meters, fluctuating between 0.1 and 6.0 meters. Ground truth for this dataset was provided by LIDAR, with data presented in the ESRI ASCII Raster format. This dataset covers Italy and is specific to each region, and it also utilizes the WGS 84 UTM coordinate system for referencing.

Another significant segment of this study was addressed to the selection of valid imaging data aligned to the military doctrines in EW deterrence, primarily derived from the Sentinel-1A platform; unlike optical satellites, the *C*-SAR radar sensor of Sentinel-1A boasts the capability to capture pristine images irrespective of cloud cover or lighting conditions: this all-weather, day-and-night imaging proficiency stood in stark contrast to the challenges encountered by optical sensors, such as those on Landsat, which registered cloud covers of 0.00%, 32.65%, and 8.79% in successive captures, with land cloud covers of 0.00%, 22.03%, and 11.46%; this underscores the uninterrupted observational capability of Sentinel-1A, offering a consistent and dependable data source in scenarios where optical sensors falter due to atmospheric constraints.

To underpin the basis of the Rationale and maximize the potential of active remote sensing, our research focused on a carefully selected group of scientific instruments with established efficacy in both civilian and military contexts: among these, the Sentinel-1 initiative, a collaboration between the European Commission and the European Space Agency (ESA) under the Copernicus program, primarily targets environmental and civilian goals; yet, the inherent capabilities of the Synthetic Aperture Radar (SAR) extend its value significantly, making it especially relevant for military applications, resonating with the core objectives of our study.

While the initial overview provided a coherent framework, it lacked comprehensive detail, which was crucial for our study's depth and breadth: to address the limitations of Sentinel-1, the expansion of the scope starting from its Rationale, incorporated insights from other aerospace missions, notably the Landsat program; its proficiency in operating consistently across varied conditions by a larger research community elevates its role in surveillance and reconnaissance: particularly, its capabilities, including robust cloud correction and a wide array of sensing indexes, are essential for cross-referencing the outputs from different sensors; this is effectively achieved using tools from the SNAP and Esri® suites.

In the context of safeguarding Heritage from the threats of armed conflicts, especially considering UAV deterrence, the advanced capabilities of our tools greatly enhance Spatial Awareness. Specifically, in areas like the hills of Selinunte, the discernment of subtle alterations on the surface has been fully accomplished and putted into action; these changes may indicate activities such as the digging of trenches, subterranean movements, and the construction of fortifications due to the unique radar signatures provided by SAR, serving to identify potential threats or targets. Here's a refined version of the provided text:

From the viewpoint of the governmental Order of Architects, the demands set forth by various associated government entities are of paramount importance and necessitate clear guidance within the architectural profession: this mandate not only underscores the importance of preserving the landscape but also directs the strategic positioning of antenna infrastructures; in essence, the final Scope is to bolster surveillance capabilities without compromising the integrity of heritage sites.

This strategy is in line with the clearance directives from the Ministry of Defense, which focus on precise and swift identification of adversarial UAV entities but to address this, we are advocated to correspond fined-up land-use integrations that are minimally invasive bridging the priorities of the Ministries of Defense, i.e. telecommunications and signal disturbance, with Cultural Heritage' visual preservation portraited by Heritage theories for the Landscape Architecture.

To achieve this degree of data fusion, considerable emphasis was placed on employing premier visual imaging techniques, within designated sites designated to be evaluated, transitioning to sophisticated Heritage Modelling, and the culmination of insights from these diverse methods integrated into a cohesive, singular manifold.

2.1. Integrating Multi-Index analysis with Digital Elevation models for prime buffer site identification across EW doctrines

In the EW domain particularly for the strategic deployment of antenna sites, the utilization of advanced remote sensing techniques, including differenced indices such as Δ Normalized Vegetation Index (ΔNDVI), Δ Water Index (ΔMNDWI), Δ Enhanced Vegetation Index (ΔEVI), and Δ Soil-Adjusted Vegetation Index (dSAVI), is crucial.

These indices, established on the groundbreaking work of researchers like Rouse JW, McKenna P, X. Hanqiu (2006), Liu H.Q. (1995), and Huete A.R., enable an in-depth analysis of environmental variables crucial for optimal antenna site selection while minimizing ecological impacts. Leveraging the spatial ($\Delta\xi$) and spectral ($\Delta\varphi$) resolution of Landsat's Operational Land Imager (OLI), this integrated approach ensures a comprehensive assessment of potential sites, taking into account factors such as vegetation density (ρ veg), proximity to water bodies (δ water), urban development (Ψ urban), and soil characteristics (σ soil).

In the versatile EW environment, the application of these indices is multifaceted and varies according to different military doctrines:

I) Western Military Doctrines: these doctrines focus heavily on technological superiority and precision: the use of ΔNDVI is crucial for identifying areas with minimal vegetation density, ensuring clear signal transmission and optimal operational efficacy of antenna systems, i.e. Szabó S. et al. (2016) demonstrated, short-term analysis of ΔNDVI is particularly effective in transitional environmental periods for identifying optimal antenna sites;

II) Eastern military doctrines for emphasizing terrain adaptability and camouflage: the ΔMNDWI's ability to delineate water bodies is valued for avoiding areas prone to flooding or waterlogging, which could compromise the structural integrity and functionality of EW installations; this approach is crucial in regions where terrain can be a critical factor in such engagements;

III) guerrilla warfare tactics: the scope of unconventional warfare methods prioritize stealth and the element of surprise: ΔEVI, with its enhanced sensitivity to vegetation dynamics, offers indeed a refined assessment of vegetation health, aiding in the selection of sites that are less likely to undergo significant ecological changes, thereby maintaining cover and concealment for extended periods;

IV) urban warfare strategies: these strategies focus on integrating EW systems into urban settings without disrupting the urban fabric; indices like ΔNBR and dSAVI are invaluable for understanding urbanization patterns and the impact of soil brightness on vegetation, crucial for the strategic placement of electronic warfare assets in urban and semi-urban environments; overall, these remote sensing indices facilitate are yearly reviewed by experts to discern environmental systems (Ω environment), supporting informed decision-making (λ decision), nonetheless limitedly in the deployment of infrastructure. Besides, one considers that their application ensures that antenna installations are operationally effective and environmentally considerate (ε environmental), maintaining a balance (ζ balance) between technological needs and ecological preservation at the panchromatic scale of 15 meters.

Name	Formula	Reference
Δ Normalized vegetation Index	$\Delta NDVI = \left(\frac{NIR_{t2} - RED_{t2}}{NIR_{t2} + RED_{t2}}\right) - \left(\frac{NIR_{t1} - RED_{t1}}{NIR_{t1} + RED_{t1}}\right)$	Rouse JW et al., (1974), McKenna, P. et al., (2018)
Δ Water Index	$\Delta MNDWI = \frac{(GREEN_{t2} - SWIR_{t2})}{(GREEN_{t2} + SWIR_{t2})} - \frac{(GREEN_{t1} - SWIR_{t1})}{(GREEN_{t1} + SWIR_{t1})}$	Xu, Hanqiu (2006)
Δ Enhanced Vegetation Index	$\Delta EVI = G \times \frac{NIR - RED}{NIR + C_1 \times RED - C_2 \times BLUE + L}$	Liu H.Q. & Huete A.R., (1995)
Δ Normalized Difference Built-up Index	$\Delta NBR = \frac{(SWIR_{t2} - NIR_{t2})}{(SWIR_{t2} + NIR_{t2})} - \frac{(SWIR_{t1} - NIR_{t1})}{(SWIR_{t1} + NIR_{t1})}$	Y., J. Gao, e S. Ni. (2003)
Δ Soil-Adjusted Vegetation Index	$SAVI = \frac{(1 + L) \times (NIR - RED)}{NIR + RED + L}$	Huete, A.R. (1988)

Chart 1. Spectroradiometrics.

2.2. Land Surface Temperature: TIRS metrics to validate broadband ε

In the specialized field of remote sensing applied to EW doctrines in archaeological areas, the analysis and quantification of land surface temperature (LST) are crucial; this process, augmented with mathematical symbols and equations, offers significant advantages in understanding and mitigating EW challenges in these sensitive sites.

The process commences with the Difference Normalized Vegetation Index (dNDVI), conceptualized by Rouse JW et al., the dNDVI is mathematically expressed as "NDVI = *gain × DN + bias*", providing a fundamental assessment of vegetation health and density, crucial in areas with archaeological significance.

Advancing from dNDVI, the Surface Emissivity Correction, developed by Fuqin Li et al. (2004), refines additionally the LST analysis: this correction calculates the emissivity, represented as "ε = a + b × NDVI", where "*a*" and "*b*" are coefficients. This step is essential for precise LST determination, especially in diverse vegetative terrains often found in archaeological sites.

The next fundamental step involves the application of the Brightness Planck function, detailed by Lin & Yuanzhi Zhang (2011). It is given by "T_b = *ln* (($L \lambda K1 + 1$)/$K2$)", where "T_b" is the brightness temperature, "L_λ" is the spectral radiance, and "*K1*", "*K2*" are calibration constants. This function effectively converts spectral radiance into a quantifiable temperature metric.

The culminating step is the calculation of LST itself, as per Mumtaz Faisal et al. (2020) methodology, formulated as "LST = $(1 + (\rho \lambda \times T_b) \times ln(\varepsilon))/T_b$", where "$\rho \lambda$" represents the wavelength; this comprehensive formula incorporates brightness temperature with surface emissivity and wavelength, providing an in-depth measure of the land surface temperature.

In archaeological contexts, the application of these methods and formulas offers several key advantages for Electronic Warfare:

   a)   enhanced predictive analysis: by accurately assessing LST, strategies can be developed to protect archaeological sites from electronic threats effectively;

   b)   strategic environmental understanding: knowledge of LST and associated variables allows for better planning and execution of EW operations, minimizing risks to archaeological integrity;

   c)   improved operational efficacy: understanding the thermal dynamics of a site aids in the optimization of EW tactics, ensuring effective deployment and reduced collateral damage;

   d)   decision-making precision: the integration of advanced remote sensing techniques with mathematical rigor enables more accurate and strategic decisions in EW contexts.

This approach exemplifies the application of complex mathematical and scientific methods in modern EW, highlighting the crucial role of environmental and mathematical intelligence in preserving archaeological heritage while navigating challenges.

Name	Formula	Reference
Difference normalized vegetation Index	$L_\lambda = gain \times DN + bias$	Rouse JW et al., (1974)
Surface Emissivity Correction	$\varepsilon = a + b \times NDVI$	Fuqin Li et al. (2004)
Brightness Planck function	$T_b = \dfrac{K_2}{ln\left(\frac{K_1}{L_\lambda} + 1\right)}$	Lin & Yuanzhi Zhang (2011)
Land Surface Temperature	$LST = \dfrac{T_b}{1 + \left(\lambda \times T_b / \rho\right) \times ln(\epsilon)}$	Mumtaz Faisal et al. (2020)

Chart 2. Spectral analysis and Thermal modeling.

2.3.1. SAR Data with $\Delta\phi$ integration : utility from processed ground range

In the domain of EW multi-domain, the precision and reliability of SAR (Synthetic Aperture Radar) data, symbolized as SAR_{data}, are fundamental, especially when formulating strategies across diverse military doctrines. This study utilized the Sentinel Application Platform (SNAP) for preprocessing SAR data, incorporating mathematical and matrix-based symbols for enhanced geospatial analysis. Critical steps included updating product metadata with precise satellite position (p-vector) and velocity (v-vector), essential for accurate geolocation and effective SAR interferometry.

The preprocessing involved filtering out thermal noise in Level-1 GRD products and converting digital numbers to backscatter coefficients (σ_0) through radiometric calibration. This process, crucial for cross-sensor comparability, also involved speckle noise reduction in SAR images using filters like Lee or Gamma Map. The transformation from slant range (S_r) to ground range (G_r) using a Digital Elevation Model (DEM) was fundamental, ensuring pixel values (P_{ij}) accurately represented ground reflectivity.

In the context of SAR implementations:

A. western military doctrines: processed SAR data (SAR processed) are invaluable for doctrines emphasizing precision and technological superiority; the enhanced imagery aids in identifying strategic locations for deploying electronic equipment, optimizing signal transmission (τ signal), and ensuring operational efficacy (η operation);

B. eastern military doctrines: these doctrines benefit from SAR's detailed topographical data (D topo), aiding in terrain adaptability and camouflage strategies. The data provide insights into terrain features (θ terrain), crucial for camouflaging EW assets;

C. guerrilla warfare tactics: SAR data (D SAR) offer insights into remote terrains, essential for guerrilla tactics where stealth (ψ stealth) and surprise are key. This facilitates the strategic placement of electronic devices in less detectable locations;

D. urban warfare strategies: SAR data's ability to capture urban landscape details (L urban) supports strategies for integrating electronic systems into urban settings without major disruptions; the processing pipeline included steps like S1 TOPSAR split (Split_TOPSAR), orbit file application (App_orbit), and SNAPHU (SNAPHU_unwrap), a software for phase unwrapping in InSAR applications, adhering to the principles of interferometric synthetic aperture radar and phase analysis.

Name	Formula	Reference
Change in phase	$\Delta\phi^{2,1} = w\,\{\phi_2 - \phi_1\}$	Wu S. et al. (2023)

Chart 3. SAR imagery phase differential discrepancies.

$SAR_{\text{image1}}(\theta, \lambda)$ and $SAR_{\text{image2}}(\theta, \lambda)$ are the phase information of the first and second InSAR images; Φ_{atm1} and Φ_{atm2} represent the atmospheric phase delays for each image, accounting for the variability in atmospheric conditions between the two acquisitions. Φ_{topo1} and Φ_{topo2} are the topographic contributions to the phase of each image, reflecting the terrain-induced phase differences. N_1 and N_2 denote the noise components in each InSAR image, including system noise and random atmospheric variations.

$$\text{IFG} = [SAR_{image1}(\theta, \lambda) + \Phi_{atm1} + \Phi_{topo1} + N_1] - [SAR_{image2}(\theta, \lambda) + \Phi_{atm2} + \Phi_{topo2} + N_2]$$

Equation 1. Retrieval of Ground Target Deformation employed by Sentinel 1-A's sensor.

$$\text{IFG} = w\,\{\Delta\phi_{total}\}$$

Where w stands for the phase wrapping operation which wraps the interferometric phase into $(-\pi, \pi]$

$$\Delta\varphi_{total} = \Delta\phi_{flat}^{1,2}$$
$$\Delta\phi_{1,2} = w\,\{\phi_1 - \phi_2\} = w\,\{\Delta\phi_{1,2}{}^{flat} + \Delta\phi_{1,2}{}^{topo} + \Delta\phi_{1,2}{}^{defo} + \Delta\phi_{1,2}{}^{APS} + \Delta\phi_{1,2}{}^{noise}\}$$

Equation 2. Phase wrapping operation employed by Sentinel 1-A's sensor.

2.3.2. Geocoding and Terrain Correction

Errors in the Digital Elevation Model (DEM), which are fundamental for terrain correction in SAR imagery analysis, can significantly impact the accuracy of final displacement measurements; when the extent of these DEM errors is known or can be reasonably estimated, a correction factor becomes essential as a phase adjustment within the interferogram counterbalancing the inaccuracies introduced by the DEM errors and ensuring a more accurate representation of the ground displacement in the processed SAR data.

Name	Formula	Reference
Conversion to Line-of-Sight Displacement	$D_{LOS} = \dfrac{\Delta\phi \times \lambda}{4\pi}$	Krieger G. et al. (2010)

Chart 4. Translating SAR phase shift multiplication into Line-of-Sight measurements.

2.3.3. LIDAR hydrological modeling : landslide risk and sensor factors

The Topographic Wetness Index (TWI), an integral concept in hydrological modeling, was notably discussed by Beven, K. J., and M. J. Kirkby in their seminal work in 1979; this index is a critical tool for quantifying the effects of topography on the distribution and accumulation of surface water; derived from a calculation that factors in both the slope and the upstream contributing area of a specific point in the landscape allows a further calculation of the TWI consisting of two variants:

Name	Formula	Reference
Topographic Wetness Index (TWI)	$\text{TWI} = \ln\left(\dfrac{Flow\ Accumulation}{Slope}\right)$	Cheng-Zhi Qin T. et al. (2010)

Chart 5. Logarithmic Ratios of Flow Accumulation and Slope.

In this context, Flow symbolizes the upstream area contributing to a particular point, and β represents the slope at that point ($\tan\beta$); this index is crucial in hydrological models for predicting the distribution of wetness and identifying potential areas of saturation within a landscape, i.e. soil moisture, landslide risk and water flow patterns for agricultural planning; TWI insights of characteristics of a terrain make was priorly conceptualized for hydrological modeling, whose focus is highlighted by the authors Cheng-Zhi Qin T. et al. (2010).

Data_type_source	Version	Methodology	Resolution	Vertical Accuracy
DEM_REM	1.1 (2023)	TIN	Native: 10 m; Resampled in windPro: 20 m	RMSE

Ground_Truth	Format	Data_Cfr_	UTM	Coverage
LIDAR	ESRI ASCII Raster	1,98	WGS 84	Italy

Chart 6. DEM dataset: *REM (Regional Elevation Model); Version 1.1 (Generated/interpolated from a Triangular Irregular Network model); RMSE Average: <3.5m; Range: 0.1m-6.0m).

PLATFORM_ID	Mission	SENSOR_ID	Tier	Ground Range Detected	Checksum	Orbit_number	S2 Level-1C Product ID	Sensing time (UTC)
Sentinel-1A	0608F8	C-SAR	GRD	Horizontal	7A38-GRD_HD	050144	S1A_IW_GRDH_1SDV_20230902T051320_20230902T051345_050144_0608F8_7A38-GRD_HD	2023-09-02 T05:13:20.256Z
Sentinel-1A	060C22	C-SAR	1SDV	Horizontal	FB98	050239	S1A_IW_GRDH_10SDV_20230908T170456_20230908T170521_050239_060C22_FB98	2023-09-08 T17:04:56.073Z
Sentinel-1A	S1	IW	SLC	1SDV	060EAC_FCE5	050312	S1A_IW_SLC__1SDV_20230908T170455_20230908T170521_050239_060C22_6018	20230913T171316_20230913T171342
Sentinel-1A	S1	IW	SLC	1SDV	060C22_6018	050239	S1A_IW_SLC__1SDV_20230920T170455_20230920T170522_050414_061219_C515	20230908T170455_20230908T170521

Chart 7. Sentinel products overview and sensors.

PLATFORM_ID	STATION_ID	SENSOR_ID	Tier	TARGET_WRS_PATH	TARGET_WRS_ROW	Level 2 Surface Reflectance	Sensing time (UTC)	CLOUD_COVER	CLOUD_COVER_LAND
LANDSAT_8	LGN	OLI_TIRS	T1	190	34	LC08_L2SP_190034_20230817_20230822_02_T1	2023-08-17 09:48:20.262	0.00	0.00
LANDSAT_8	LGN	OLI_TIRS	T1	190	34	LC08_L2SP_190034_20230902_20230912_02_T1	2023-09-02 09:48:22.965	32.65	22.03
LANDSAT_9	LGN	OLI_TIRS	T1	190	34	LC09_L2SP_190034_20230910_20230912_02_T1	2023-09-10 09:48:26.616	8.79	11.46

Chart 8. Landsat 8-9 Operational Land Imager and Thermal Infrared (TIRS) Collection 2 Level-2.

2.4. Maximizing signal efficacy in hostile environments : EW intersections in τ reference

To establish references through : i) the geodesic equation, ii) Path Loss, and iii) the Fresnel equation, a coordination to validate as whole these formulas was conferred: For a) the motion of a particle along the shortest path in curved spacetime it is expressed as:

$$\frac{d^2 x^\mu}{d\tau^2} + \Gamma^{\alpha}_{\beta\mu} \frac{dx^\alpha}{d\tau} \frac{dx^\beta}{d\tau} = 0$$

Equation 3. Whereby x^n is the spacetime coordinates, τ is the proper time,
and $\Gamma^{\alpha}_{\beta\mu}$ are the Christoffel symbols representing hypothetical spacetime curvature.

A fundamental scope of the research ultimately aimed at delivering distributed results in the heritage site, on the basis of $PL(dB)$, the ii) in decibels, PL_0, which is the Path Loss (PL) at a reference distance d_0, n, the PL exponent indicating how the signal strength decays with distance d, and X_σ, which accounts for random variations premised.

$$PL(dB) = PL_0 (dB) + 10 \cdot n \cdot log_{10}\left(\frac{d}{d_0}\right) + X_\sigma$$

Equation 4. The subsequent component of the equation, $10 \cdot n \cdot log_{10}\left(\frac{d}{d_0}\right)$, intricately captures the distance-dependent aspect of signal decay added to X_σ term which is incorporated to account for the stochastic or random variations.

The sum of the reflection and transmission coefficients equals 1 in a lossless medium, signifying energy conservation and concerning their application for iii), these equations are crucial in designing optical systems, understanding the behaviour of radar and sonar waves at different interfaces, and in various applications in general telecommunications.

$$R = \left|\frac{n_1 \cos(\theta_i) - n_2 \cos(\theta_t)}{n_1 \cos(\theta_i) + n_2 \cos(\theta_t)}\right|^2 (1) \; ; \; T = \left|\frac{2n_1 \cos(\theta_i)}{n_1 \cos(\theta_i) + n_2 \cos(\theta_t)}\right|^2 (2)$$

Equation 5. Whereby (1) n_1 and n_2 are the refractive indices of the first and second medium, respectively, θ_i is the angle of incidence (the angle at which the wave strikes the interface), θ_t is the angle of transmission (the angle at which the wave passes through the interface) ; (2) The relationship between the angles of incidence and transmission is governed by Snell's Law, which is $n_1 \sin(\theta_i) = n_2 \sin(\theta_t)$.

2.4.1. Harnessing complexities of spacetime in EW for stealth and detection in parkland zoning and synchronized SAR operations

Each formula mentioned in the previous paragraph is fundamental within its field, general relativity, telecommunications, and optics: however, their interrelation is minimal as they operate under different principles and scales.

With regard of the primary scope, to assess a proper non-destructive geospatial exploration in heritage studies, the case is nestled on the southwestern coast of Sicily, Selinunte, an ancient Greek city, becomes the focal point of our: this archaeological wonder, home to an expansive park dotted with remnants of temples, altars, and relics of a classical age, beckons the need for modern-day conservation, resilient through advanced technology.

Recognizing the delicate balance between preservation and the pressures of modernity, the aim is addressed to create a comprehensive geospatial blueprint of Selinunte; this map, a fusion of history and technology, will spotlight both the preserved structures and any nuances that might hint at erosion, or unauthorized intrusions punished under its different surveillance bodies.

The expanse around Selinunte, particularly a rough 6 km radius with designated landmarks like the southern temple at its heart, holds untold stories and hidden threats. Through Sentinel-1's SAR capabilities, the aspiration is addressed to unveil both: detecting the whispers of past civilizations and the potential anomalies of the present, be it clandestine excavations or encroachments.

Harnessing the prowess of tools like SNAP and ArcGIS®, the raw data undergoes a transformation, evolving from pixelated imagery to a detailed cartographic representation of Selinunte's legacy.

At this stage, shall we agree to merely consider this research an academic exercise? The layers of insights derived hold profound implications for both civilian governance and defense sectors. It's not anymore, a matter ultimately towards sustainable tourism, but as an infrastructure that bows to heritage, with even strategic insights given Selinunte's geographical

placement in the Mediterranean area. Beyond the data and the tools lies our overarching vision: a world where the past's grandeur isn't shadowed by the present's ambitions: through this effort, the hope is given to echo the sentiment that sites like Selinunte aren't just relics to be observed but heritage to be preserved.

2.5. Data sources and their ethical utilization

The research relied on data acquired from both I) Landsat and II) Sentinel-1 satellite platforms: I), a joint initiative between the U.S. Geological Survey (USGS) and NASA, has been capturing Earth observations since 1972; all I) data is available under the U.S. Government's open data policy, meaning users can freely access, modify, and share this data for any purpose.

The II) mission, on the other hand, is part of the Copernicus program led by the European Commission in partnership with the European Space Agency (ESA). Sentinel-1's data, particularly noteworthy for its Synthetic Aperture Radar (SAR) capabilities (f = 5.405 GHz and λ = 0.0555 meters), is similarly available under an open access policy, making it free for commercial, scientific, and educational purposes.

To process and analyze the vast datasets from these satellites, specialized software tools are indispensable: SNAP (Sentinel Application Platform) is one such tool, designed primarily for the processing of Sentinel data; developed by ESA, SNAP provides a comprehensive array of tools for processing and computing Sentinel data, among other satellite datasets. While its primary focus is on the Copernicus Sentinel missions, it also supports data from other sensors; as with the data, SNAP is available under an open-source license, allowing for modifications and customizations by the user community.

Another tool in this research employed was ®ArcGIS, a geographic information system (GIS) developed by ®Esri: ®ArcGIS offers capabilities for mapping, spatial reasoning, and analysis, making it indispensable for handling geospatial data; while the software itself is proprietary, ®Esri provides licenses for academic, non-profit, and commercial use, each with its own set of terms and conditions; users must ensure compliance with ®Esri 's licensing agreements, particularly when disseminating results or derived products. It's essential to acknowledge that while these platforms and tools provide vast amounts of data and processing capabilities, each comes with its own set of terms, conditions, and copyrights. Users must remain vigilant and adhere to these stipulations, ensuring ethical and lawful utilization of the resources; additionally, while the data is often free, users should always credit the respective agencies (USGS, NASA, ESA, ®Esri) when publishing or presenting research findings derived from their datasets or tools.

2.6. Literature survey of morphological analysis applications

Morphological Analysis (MA) is a systematic technique designed to dissect complex, multi-dimensional problems, offering insights into possible solutions. Its applications span across an array of fields. In image processing and computer vision, MA-driven operations such as dilation and erosion have been crucial for tasks like noise reduction and image enhancement, as meaningfully detailed by Gonzalez and Woods (2008).

Linguistically, MA assists in the decomposition of words into fundamental units, morphemes, illuminating facets of language evolution and semantics, a concept explored by J. Carrier, and M. Aronoff (1979): from an environmental perspective, scientists have employed MA to classify and analyse landforms, e.g. Pike R. (1988), who showcased its taxonomy in Martian surface texture characterization; additionally, its role in risk assessment is noteworthy, aiding in the deconstruction of intricate systems and scenarios, a *concept-structuring method,* Ritchey (2006), who formulated sociological implications to structuring Generical Morphological Analysis (GMA), towards multifaceted decision-making problems.

In the realm of cryptography, MA's principles have been tapped into for designing cryptographic algorithms, with Mather (1999) shedding light on its relevance in digital watermarking. The medical field, particularly cellular biology, utilizes MA for quantifying and analyzing cellular structures and patterns, as discussed by Vincent and Soille (1991) by computing watersheds in digital gray-scale images.

Nonetheless, the broad applicability of MA doesn't render it without challenges: a notable limitation is the potential for combinatorial explosion with an increase in variables, which can lead to an overwhelming number of unprecedented solutions; moreover, MA's expansive scope of exploring possibilities doesn't inherently offer prioritization among these solutions, a feature often sought in real-world scenarios. In essence, MA's versatility, as supported by extensive literature, underscores its significance in structuring and interpreting intricate problems across diverse disciplines.

2.6.1. Military Archaeology and Industrial Military Archaeology : *ubi sumus in pacis tempore*? Sicily as a living testament to Heritage at the forefront

In the realm of archaeological studies, the intersection of military archaeology and industrial military archaeology poses unique challenges and opportunities, especially in the context of ensuring accurate and unbiased data interpretation; the latinist question, "*ubi sumus in pacis tempore* ? " or "*Where are we in times of peace* ? " becomes pertinent, highlighting the juxtaposition of past conflicts with present tranquility: Sicily, with its layered soil of historical events and artifacts, serves as a living testament to this dynamic, placing heritage at the forefront of academic and strategic interest.
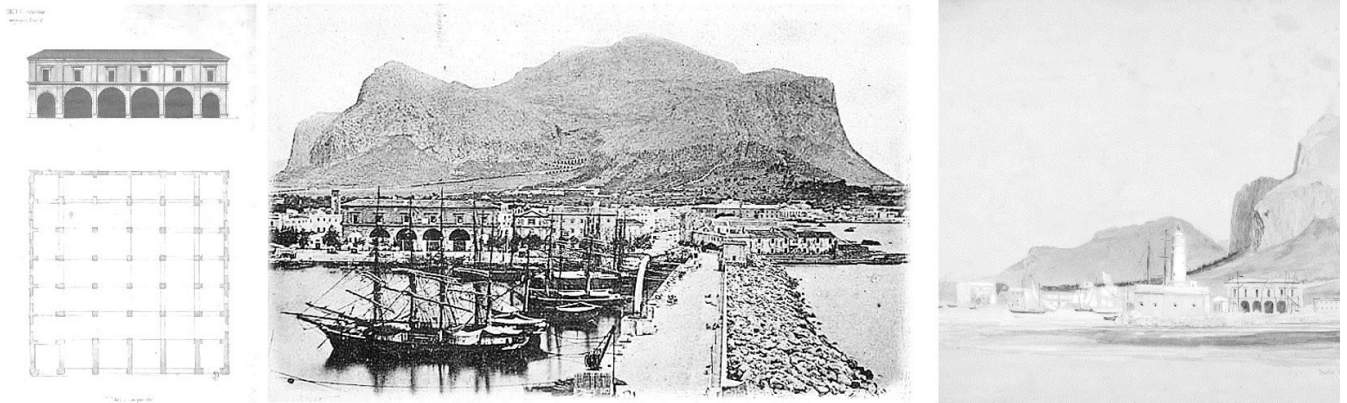
Fig. 5. Palermo's Maritime Tapestry: The Arsenale in Questel's 1831-1832 Voyage and the Architectural Evolution of the 17th Century Waterfront. Source: http://www.museodelmarepalermo.it/. Credits: CC0 1.0 Universal. **Fig. 6.** The *Regio Arsenale* of Palermo: An Emblem of Urban Evolution and Maritime Prowess. Around 1900. Palermo, Italy. Source: Biblioteca Comunale Palermo (flickr.com). Credits: CC BY SA 4.0. **Fig. 7.** The *Arsenale* Captured: Miner Kilbourne Kellogg, *Moli at Palermo*, pencil and watercolor on paper, sheet: 9 x 12 in. (22.9 x 30.5 cm), Smithsonian American Art Museum, Bequest of Martha F. Butler, 1991.56.50. 1854. Palermo, Italy. Source: https://americanart.si.edu/. Credits: CC0 1.0 Universal.
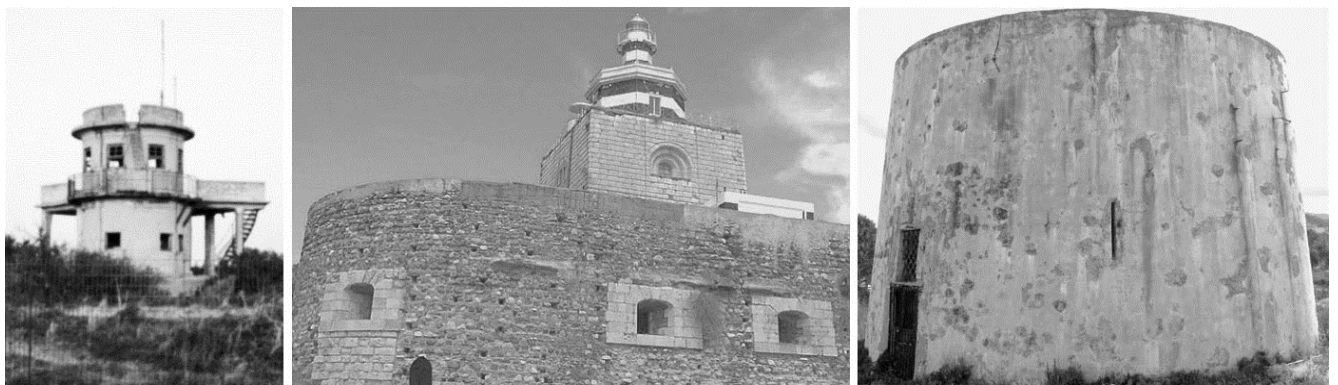
Fig. 8. Maritime Communication Legacy: Forte Spuria's Semaphore in Granatari, Messina - A Radiotelegraphic Marvel from the 19th Century, Elevated at 98 Meters. Championed by Guglielmo Marconi in 1906, this beacon established robust data links with Monte Mario Station in Rome, operating under the aegis of the Italian Navy until the 1970s. Item ID: U_13 (fortistrettomessina.it). Source: Unplash.com. Credits: CC0 1.0 Universal. **Fig. 9.** *Torre della Lanterna Montorsoli* in Messina: a 16th-Century Navigational Landmark and its Historical Significance in Maritime Telecommunications from Past to Present. 2003. Photo by: Simon Praud. Source: wikimedia.org. Credits: CC0 1.0 Universal. **Fig. 10.** *Torre Martello* (Donato A. & Teramo A., 2014). Source: Unplash.com. Credits: CC0 1.0 Universal.

2.6.1.1. Emerging scope of deterrence in Heritage protection: Electronic Warfare's *Monte Cassino* influence through times

The evolving landscape of global defense and security, characterized by the rapid integration of cutting-edge EW technology and counter-strategic jamming modelling (Zhang X. et al., 2022), necessitates a unified harmonization of tradition with modernity: Self-Determination in maintaining Heritage preserved by outer forces and internal groups, will lead to active change in today's democratic societies, gaining added significance when viewed through the lens of Active Citizenship Silliman W. (2007) in such a volatile environment at the expenses of neglected cultural Heritage (Belal A., et al., 2019, Barakat S., 2021).

Sicily, with its intricate blend of historical richness and contemporary evolution, exemplifies this intricate simulation between the past and the present: the showcased prowess of the U.S. RQ-7B Shadow UAS, the RQ-21A STUAS, and the E-3 AWACS are an example of UAV exercises enrolled into electronic deterrence and epitomize the melding of modern small-scale warfare techniques with strategies deeply rooted in centuries-old defense traditions retrieved from digital sensing (Juhász, A. et al., 2016, UNESCO & UNITAR, 2018).

The incorporation of clearance-level technological instruments presents a counterintuitive dilemma: the encroaching menace of covert adversaries, equipped with sophisticated EW capabilities, aiming to penetrate and extract confidential data. Notably, Heritage inventories (Brosché J. et al., 2016), which serve as repositories of a nation's cultural and historical last storeroom, are now susceptible to these cyber ambushes (Freedberg S., 2012) that challenge with Riegl's assertion, emphasizing the evolving nature of EW landmarks as modern monuments (Cunliffe E., 2020): "*The sense and meaning of a monument do not belong to the works by virtue of their original purpose; it is rather we, the modern subjects, who attribute them*" (Meyer A., 2013).

Fig. 11. Bunker, Sant'Agata, Sicily, Italy. Photo by: USA Army. 1944 (?). Source: Birtle, J. (1993) p.25. Credits: Public Domain Mark 1.0. **Fig. 12.** *Favigna Castello*, Santa Caterina, Sicily, Italy. Photo by: Gabriella Panareo, April 27, 2018. Source: wikimedia.org. Credits: CC BY-SA 4.0 DE DEED.

As our dependence on volatile storage surges, there emerges an undeniable urgency for robust surveillance and EW defense mechanisms: these mechanisms are designed to pre-emptively counter any electronic espionage attempts, ensuring that well known in ancient fortifications (ICOMOS, 2021) "*zone d'ombra*", or shadowed recesses, remain susceptible to breaches; such strategies are not only about preserving physical assets but are also about safeguarding the intangible ethos they enshrine.

Historical landmarks like *Monte Cassino* in Italy and *Tas-Silġ* in Malta, which have experienced the tumultuous ebb and flow of counter-offensives, retreats, and ambushes, underscore the feeble but anticipatory connection EW interchange introduced by portable broadcasting equipment, between volatile environments and Heritage monuments (Rennie K., 2021).
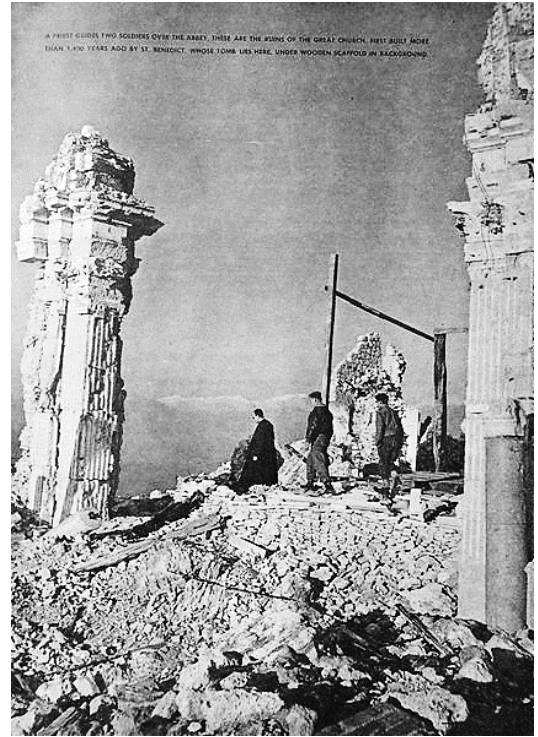
Fig. 13. *"The ruined monastery at Cassino, Italy"*, Lazio, Italy. May 19, 1944. Author: Sgt McConville, No 2 Army Film & Photographic Unit. Source: Imperial War Museum on the IWM Non-Commercial Licence. Credits: Public Domain.
Fig. 14. "*Ruins of Abbey of Monte Cassino, Priest Guides Two Soldiers Over the Abbey. These are The Ruins of The Great Church, First Built More Than 1,400 Years Ago by St. Benedict, Whose Tomb Lies Here, Under Wooden Scaffold in Background"*, Lazio, Italy. February 9, 1945. Author: U.S. Army, Yank photographer. Source: Yank, The Army Weekly. Credits: Public Domain.

Figure 15. Signallers of the 6th Battalion Royal West Kent Regiment using a radio in a dugout on Monastery Hill during the Second Phase, 15 February - 10 May 1944. Photo by: Sergeant W. E. McConville, No. 2 Army Film and Photo Section, Army Film and Photographic Unit. Production date: 1944-03-26. Material: Nitrate. Catalogue number: NA 13363. Credits: IWM Non-Commercial Licence. © IWM NA 13363. **Figures 16-17.** The Type 13 CMH (CentriMetric Heightfinder) Radar: The R.A.F.'s first centimetric radar, designed to enhance height data at Ground Controlled Intercept (GCI) stations. Introduced with dual vertically mounted cheese antennas, a narrow 1.5° vertical beam nodded between -1° and +20° elevation, and a 7.5° horizontal beam width. Its primary display was an E-scope, used for measuring aircraft height. Developed in 1942, it underwent various modifications with the Type 13 Mk V featuring an improved antenna similar to the Type 14 Mk VI. Key specifications include an S-Band frequency, 500 Hz pulse repetition frequency, pulse widths of 0.6 or 1.9 μs, and a peak power of 500 kW. Pictured: Type 13 Mk5 radar, with an antenna measuring 20 feet by 5.5 feet. Location: Malta, *Tas-Silġ* no 21033 A.M.E.S TYPE 13, a significant multi-period sanctuary site. Photo: via Subterranea Britannica Research Study Group. Publisher: Christian Wolff. Credits: GNU Free Documentation License & Creative Commons Attribution-Share Alike 3.0 Unported license.

2.6.1.2. *Monte Cassino* abbey backdrop: theoretical aspects of early EW pulse modulation

The Battle of *Monte Cassino* was primarily a ground battle, characterized by intense infantry and artillery combat; while radar and radio communications played a role in broader strategic operations, the direct application of radar technology, such as (Δt) pulse modulation in its periodic waveform, and jamming at the battlefront was more limited compared to their use in aerial or naval warfare contexts: the interception of Nazi communications during the *Monte Cassino* campaign involved radio intelligence, such as listening to enemy broadcasts and decoding messages while repositioning.

Nonetheless this was a separate domain from radar technology and involved different sets of equipment and expertise, primarily focused on signal interception, cryptography, and intelligence analysis, these technological Limitations, while advanced for its time, showed confines in terms of the sophistication and integration of radar jamming and signal interception; specifically, the equipment was often bulky, uncomplicatedly to modern standards fabricated on Ohm's Law ($V = IR$) and basic circuit theory; i.e. a superposition, where two or more waves (original signal and jamming signal) superimpose to form a resultant wave and the techniques required considerable skill and often depended on the strategic positioning of forces and intelligence assets.

Fig. 18. "*Monte Cassino, Fallschirmjäger in Höhle*" ("Paratrooper in cave"), Lazio, Italy. March 7, 1944. Image retrieved from the German Federal Archives as part of a cooperation project. Photographed by: Engel. Photo ID: Bild 183-J16902. Accessed in October, 2023. Source German Federal Archives Credits: CC-BY-SA 3.0. **Fig. 19.** "Bei *Monte Cassino, Fallschirmjäger auf Beobachtung*" ("Paratrooper on observation"), Lazio, Italy. March 7, 1943. Image retrieved from the German Federal Archives as part of a cooperation project. Photographed by: Haas. Photo ID: Bild 101I-578-1932-11A. Accessed in October, 2023. Sourc: German Federal Archives. Credits: CC-BY-SA 3.0.

2.6.2. SAR-UAV technologies in Heritage defense and multi-domain threats

In the quest of SAR and Unmanned Aerial Vehicles (UAVs) stand out as prime examples of these advances. SAR, known for its capacity to deliver high-resolution imagery irrespective of atmospheric conditions, paired with UAVs' flexibility, provides an unparalleled advantage in monitoring historical sites for various reasons periodically.

Recent field training exercises, such as the U.S. Air Force Reserve-U.S. Army Reserve's Global Medic, have been essential in illuminating these challenges. As seen in **Fig. 20**, Maj. David Hernandez demonstrates the potential of a 4G battlespace using commercially available technologies. This type of innovation is not limited to ground operations. In **Fig. 21**, U.S. Army Spc. Corey Lee launches an RQ-11 Raven UAV, which showcases the real-time airborne surveillance capabilities crucial for heritage defense.

Nonetheless, as these technologies evolve, so do the threats they face and the stealth capabilities of EW can potentially jam or deceive signals from SAR-UAV systems. This cat-and-mouse game between technological progress and its associated threats emphasizes the need for ongoing research and adaptation. The F-35C Lightning II, depicted in **Fig. 22**, is a testament to this dynamic. Equipped with cutting-edge EW hardware, it carries an Electro Optical Targeting System (EOTS), Active Electronically Scanned Arrays (AESA) radar, Distributed Aperture System (DAS), and

a Helmet Mounted Display System, which enhances the pilot's geospatial awareness, ensuring consistent deterrence during crises.

The quest for technological superiority doesn't end there: **Fig. 23** illustrates the XMQ 13 Instant Eye Unmanned Aerial System (UAS), a testament to the U.S. 5th Fleet's commitment to staying ahead of potential electronic adversaries. This continuous evolution underscores the balance between innovation and vigilance in the mission to protect our invaluable cultural heritage.

Fig. 20. Maj. David Hernandez, Deputy Branch Chief for Future Capabilities Assessment Branch, provides a capabilities demonstration of the 4G battlespace utilizing off-the-shelf technologies at Muscatatuck Urban Training Center in Butlerville, Ind. Photo by: Sgt. 1st Class Brad Staggs, June 13, 2012. Photo ID: 120613-Z-YX241-067. Credits: Public Domain. **Fig. 21.** U.S. Army Spc. Corey Lee, a military police officer with the 603rd Military Police Company, launches an RQ-11 Raven unmanned aerial vehicle at Fort Hunter Liggett, Calif. Global Medic, June 23, 2012. Photo by: Sgt. Erica J. Knight. Photo ID: 120623-F-AB151-271. Credits: Public Domain.
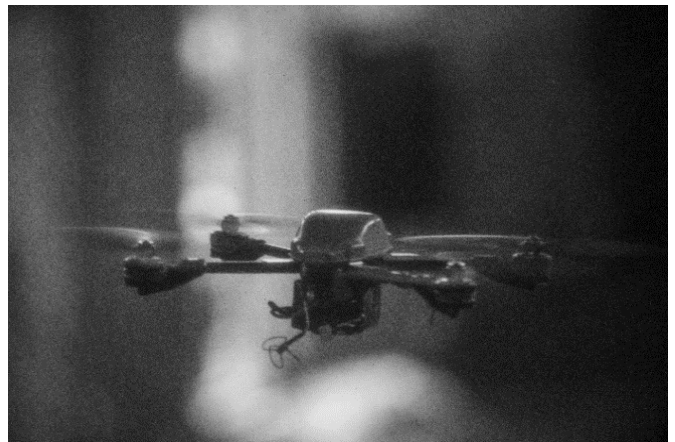
Fig. 22. A F-35C Lightning II equipped with in EW hardware likely carrying Electro Optical Targeting System (EOTS), Active Electronically Scanned Arrays (AESA) radar, Distributed Aperture System (DAS), and Helmet Mounted Display System augmenting geospatial awareness to the pilot, by enduring deterrence consistency throughout crisis scenarios. Photo by: Chief Mass Communication Specialist Shannon E. Renfroe, U.S. Navy. Item ID: 181116-N-FC670-040. Credits: Public Domain. **Fig. 23.** XMQ 13 Instant Eye Unmanned Aerial System (UAS) tested by the U.S. 5th Fleet, May 11, 2018. Photo by: Cpl. Jered T. Stone, U.S. Marine Corps. Item ID: 180511-M-WP334-0008. Credits: Public Domain.

2.6.3. Modern intrusions : rise of Electronic Warfare antennas and their physical presence, juxtaposed against the traditional Italian landscape

Italy, renowned for its sweeping landscapes, historical monuments, and rich cultural tapestry, finds itself at a crossroads of tradition and modernity: the radiation pattern of an antenna, which is critical for its functionality in EW, can be represented as $E(\theta, \phi)$ or $H(\theta, \phi)$, where E and H are the electric and magnetic fields, and θ and ϕ are the angular coordinates in spherical coordinates: the gain of an antenna, a measure of its ability to direct or concentrate radio wave energy, is denoted as $G(\theta, \phi)$.

Signal processing, a crucial aspect of EW, involves Fourier transforms (FT) to analyze signal frequencies: $F(\omega) = \int f(t)e^{\wedge}\{-i\omega t\}\, dt$, where $F(\omega)$ is the FT of the signal $f(t)$.

Filtering and noise reduction, essential in EW, can be represented by convolution operations: $f * g = \int f(\tau)g(t - \tau)d\tau$.

Regarding Electromagnetic Wave Propagation, the Maxwell's equations govern the behavior of electromagnetic waves, which are fundamental to EW antennas: $\nabla \cdot E = \rho/\varepsilon_0, \nabla \cdot B = 0, \nabla \times E - \partial B/\partial t, \nabla \times B = \mu_0 J + \mu_0\, \varepsilon_0\, \partial E/\partial t$.

Health and Environmental Impact Considerations were also considered: concerns about the health impacts of electromagnetic fields (EMF) involve understanding the intensity of these fields, represented as E (electric field strength) and B (magnetic flux density); albeit these advancements, the power density of an electromagnetic wave, a factor in assessing potential health risks, is given by $S = E \times H$, where S is the *Poynting* vector representing power per unit area.

This symbolic representation of Italy's struggle to balance its rich past with modern technology could be metaphorically represented by the wave-particle duality in quantum mechanics, symbolizing the dual nature of preserving history (particle-like, discrete and localized) while embracing the wave-like spread of technology and progress.
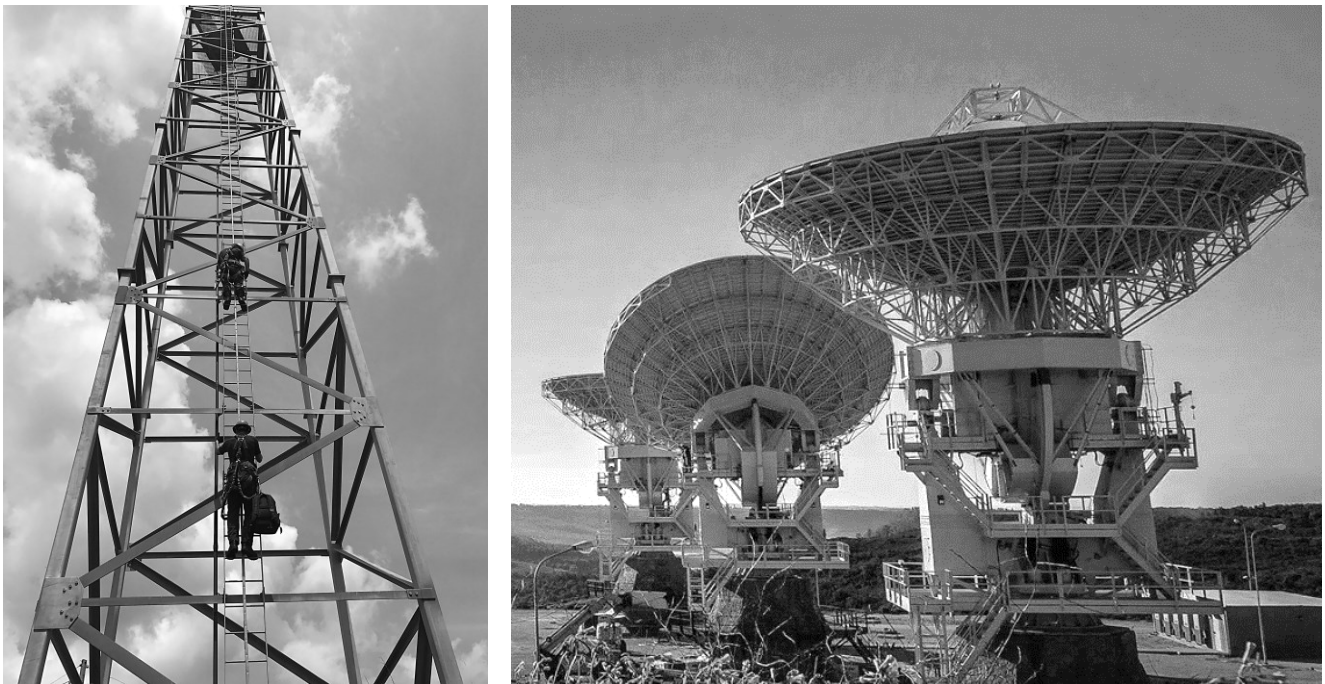
Fig. 24. U.S. Coast Guard Petty Officer 3rd Class Zachary Hensley and Petty Officer 3rd Class Conner Johnson, Coast Guard Aids to Navigation Team Galveston. Climbing a Range Light: Recovery Efforts after Hurricane Harvey on Bolivar Peninsula. Bolivar Peninsula, Texas. Sept. 3, 2017. Photo by: U.S. Coast Guard photo by Petty Officer 3rd Class Jordan Akiyama. Photo ID: 170903-G-ED165-077. Source: U.S. Coast Guard Archives. Credits: Public Domain. **Fig. 25.** U.S. Naval Radio Transmitter Facility, Niscemi, Italy. Photo by: U.S. Navy photo/Released, March 13, 2018. Source: wikimedia.org. Photo ID: 180313-N-JQ378-003. Credits: Public domain.

2.6.4. Augmented Vision : the paradox of fluid tactics in critical environments with the unmatched dichotomy of swiftness and preservation

This duality presents unique challenges. How does one innovate at breakneck speeds while ensuring that core systems, many of which may be legacy platforms, remain secure and intact? How does a nation protect its digital heritage from adversaries' intent on rewriting or erasing it? And how do defence strategies balance the need for rapid action with the patience and meticulousness required for preservation?

In essence, the digital EW landscape is a dance of contrasts, it's a realm where the swift currents of offense and defence meet the steadfast anchor of preservation. It can be interpreted as such according to the Differential Game Theory Model in which two are the key players in this dichotomic paradigm, Speed versus Meticulousness, A (Agility) and P (Preservation): $dSA/dt = fA(SA, SP)$ and $dSP/dt = fP(SA, SP)$.

Understanding and navigating this paradox is critical for any nation aiming to secure its place in the $\Delta\Psi$ representing the ever-changing state of cyber tactics in EW, where Ψ symbolizes the tactical landscape.

The rate of change $d\Delta\Psi/dt$ epitomizes the rapid evolution of strategies, mirroring the chaotic and dynamic nature of cyber warfare. Visualize a vector field $\vec{F}(x, y, z, t)$ in a multidimensional strategic space, where each vector represents a potential tactical move at any given point in time and space.

Encryption Integrity plays a fundamental role in Information domain control, whereby $E(M, K)$ represent the encryption of message M with key K, and the inverse function $E - 1(C, K)$ for decryption.

Digital Heritage can be also be interpreted as a Fractal Construct, considering the digital heritage as a fractal $D(z)$, where each iteration represents layers of historical and cultural data together with the Quantum Analogy whereby Quantum Superposition of Offense and Defence: EW strategy is recognized as $\Psi EW = \alpha|O\rangle + \beta|D\rangle$, where α and β are complex probability amplitudes.

Fig. 26. U.S. Army Pfc. Cole Burkhead and Pfc. Wyatt Jester, Infantrymen of Able Company, 2nd Battalion (Airborne), 503rd Infantry Regiment "*The Rock*", 173rd Airborne Brigade. Scanning for Targets: The U.S. Army's Contingency Response Force in Action at the Gunfighter Gym. Vicenza, Italy. June 22, 2018. Photo ID: 180622-A-LJ797-910. Source: Department of Defense, Current Photos. Credits: Public Domain. **Fig. 27.** U.S Army Sgt. Sara Cashdollar, Charlie Company 7, 158th GSAB, Colorado Springs, Colo." Scouting from an HH-60M Black Hawk: Exercise Patriot Warrior and Interlinked Training Exercises in Action. Volk Field Air National Guard Base, Wis. Aug. 18, 2017. Photo by Staff Sgt. Corban Lundborg. Photo ID: 170818-F-IZ285-0003. Source: U.S. Air Force Archives. Credits: U.S. Air Force. Credits: Public Domain.

The Sierpinski Triangle, for instance (Falconer K., 2003), is a classic example of a fractal, constructed using an Iterative Function System (IFS) with contraction mappings: $f_1(x, y) = \left(\frac{x}{2}, \frac{y}{2}\right)$; $f_2(x, y) = \left(\frac{x+1}{2}, \frac{y}{2}\right)$; $f_3(x, y) = \left(\frac{x}{2}, \frac{y+1}{2}\right)$; by iteratively applying these functions, a self-similar fractal pattern traced so that the telecommunications design, has been moved towards firm triangulation techniques which are essential for determining the location of a signal source by measuring angles or distances from multiple known points throughout the EW infrastructure designated; this plotted across this tridimensionality process has utilized geometric principles, starting from the Law of Cosines (Bronshtein, I.N., 2015) and perpetuating with fine-tuned evaluative patterns.

3. Results from the short-term EW analysis in Heritage park preservation

The integration of InSAR (Interferometric Synthetic Aperture Radar) technology, with a specific focus on the mm/rate Line-of-Sight (LOS) spectrum, in geospatial science represents a multifaceted and open advanced approach; this methodology is crucial for monitoring subtle terrain changes, especially in sensitive areas like heritage parks, where such changes could indicate potential threats or unauthorized activities.

3.1. Incorporating mm/short-term *LOS* Spectrum in InSAR rate

Specifically, topographic phase shifts observed through *VV* polarization, sophisticated mathematical techniques are employed: the symbolic matrix M represents these phase shifts, with each element M_{ij} reflecting specific values adjusted for the mm *LOS* spectrum: the diagonalization of this matrix into D through eigenvalue decomposition, along with the application of Fourier Transform, provides a quantitative understanding of the phase shifts and their implications on the landscape; additionally, a correlation matrix C is derived, providing insights into the interconnectedness of topographic patterns.

The capabilities of InSAR addressed to the research topic, augmented by the mm *LOS* spectrum focused on this short-term evaluation, are demonstrated through visual representations: **Fig. 28** showcases VV Polarization Topographic Phase Shifts, while **Fig. 29** represents the spectrum of Interferometric Phase Shifts in *VV* Polarization, incorporating the *LOS* spectrum analysis; these visualizations provide a comprehensive understanding of the landscape dynamics, highlighting the application of InSAR in such multi-domain and its significance in preserving the cultural and historic value of heritage parks.

Important monitoring ground movements have been finally analysed according to the Singular Value Decomposition (*SVD*) of *VV* Polarization Phase Matrix: applying singular value decomposition to the matrix of *VV* Polarization phase shifts, this subsection has dissected the data into singular vectors and values, which elucidated the most significant modes of topographic variation captured during the measurement period denoting Interferometric Wide swath mode and capturing wide-range high-resolution imagery for the premised scope.

3.2. Deploying Phase Information: unwrapping "modulo 2π" : *C*-band 5,55 cm wavelength

In the domain of InSAR (Interferometric Synthetic Aperture Radar) analysis, the unwrapping phase is indeed a critical vectorial operation that intricately translates the wrapped phase constituents, ϕ wrapped, derived from a dual SAR image dataset, into a continuous phase space ϕ continuous: this operation is crucial for extracting precise geophysical displacement vectors D from the interferometric phase data $\Delta \phi$.
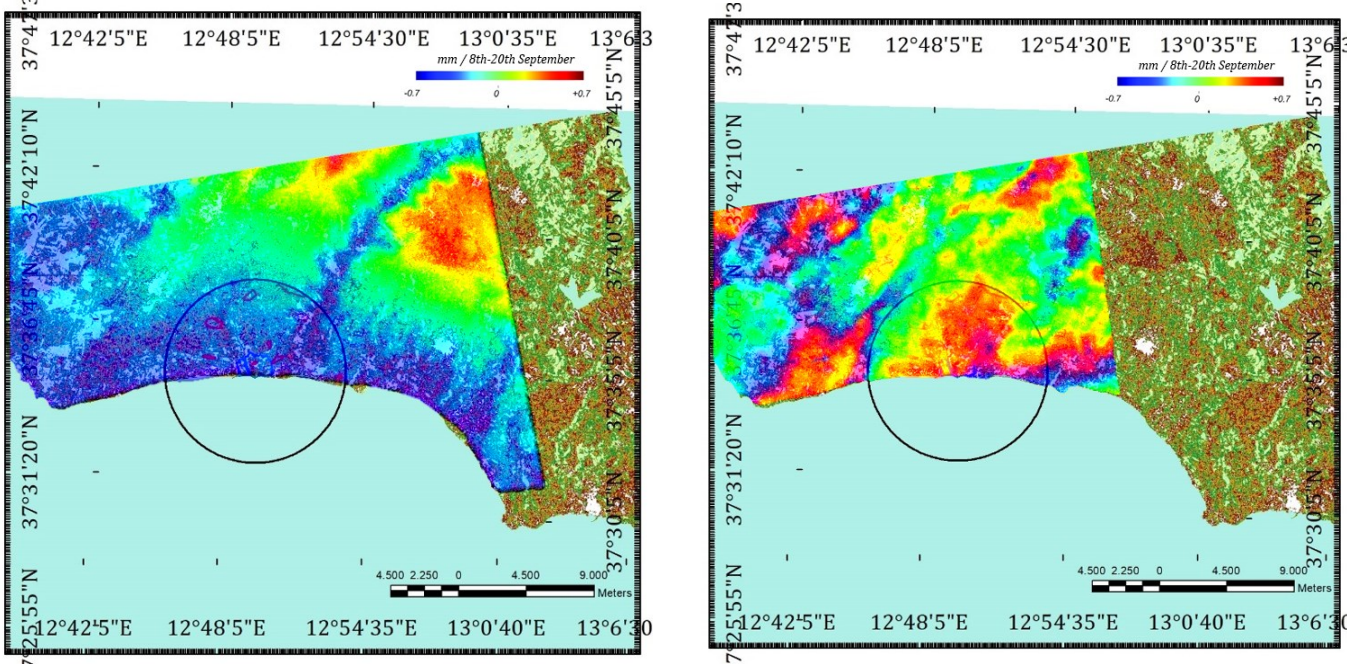
Fig. 28. Orthorectified topographic phase shifts: this vector is predominantly aligned with the radar's line of sight, LOS, and quantified in the electromagnetic wavelength λ. Similarly, to all *C*-band SAR systems with $f \approx 5.405$ GHz, the displacement vector D was formulated as $D = (4\pi/\lambda) \Delta \phi$ continuous. This process necessitated incorporating the satellite's orbital vector O and imaging geometry G, along with necessary atmospheric and environmental corrections.

The resultant displacement vector *D* final was thus a product of these calculations and corrections following quantification of displacement vectors. **Fig. 29 (right) and 30 (below).** Orthorectified algorithmic post-unwrapping employment: interferometric phase shifts in *VV* Polarization: the continuous phase ϕ continuous was transformed into a quantifiable physical displacement vector *D*.

The initial phase modulation, ϕ initial, encompassed within the interferogram, adheres to a periodic structure confined within $[-\pi, \pi]$: this phase representation is inherently topologically analogous to a toroidal surface, necessitating the application of a complex unwrapping algorithm to resolve the true geophysical displacement magnitudes; the phase values are thus defined as ϕ initial = mod (ϕ true + π, 2π) − π, where ϕ true represents the actual phase shift due to ground displacement. Additionally, the unwrapping procedure, denoted by the function *U* (ϕ wrapped), involves the employment of advanced algorithmic structures: these algorithms are tasked with the identification and rectification of phase discontinuities, symbolized by Δ ϕ discontinuities, which are indicative of the inherent -π to π phase jumps.
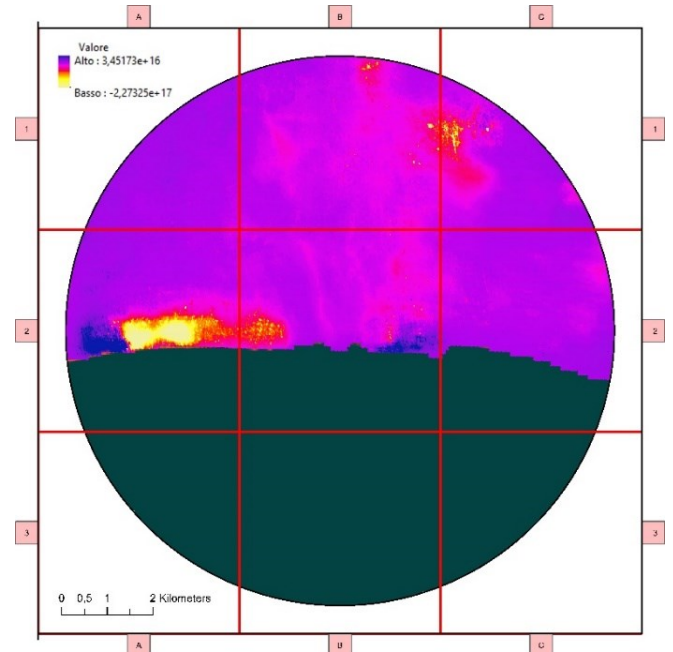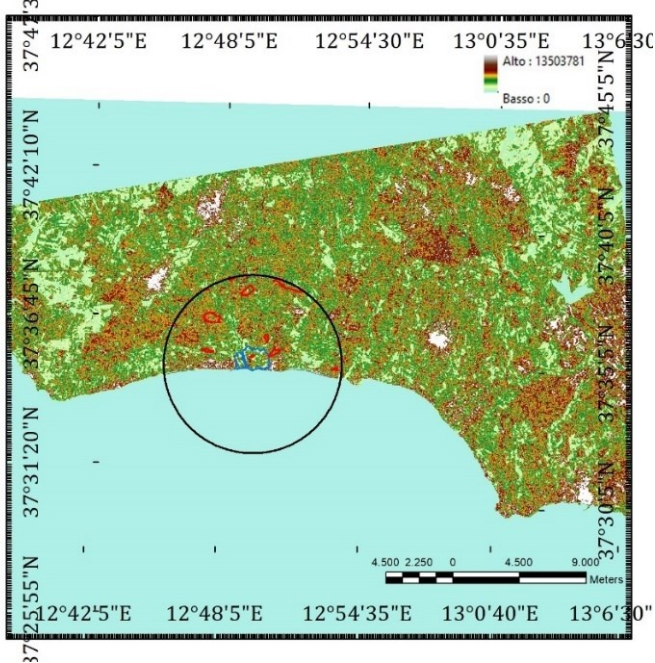
Sub-centimetres level terrestrial movements, essential for strategic applications in various scientific and surveillance domains of target area. **Fig. 31.** Horizontal *VV* polarization for both signal and reception. **Fig. 32 (below).** Optical Imaging fusion: near-infrared infrared (circa 0,851 to 0,879 μm) λ_5 (341 to 352 THz), short-wave green (0,533 to 0,590 μm) λ_3 (507 to 566 THz) and *C*-band. Visual configuration: λ_3 stacked with *C*-band-*C*-band.
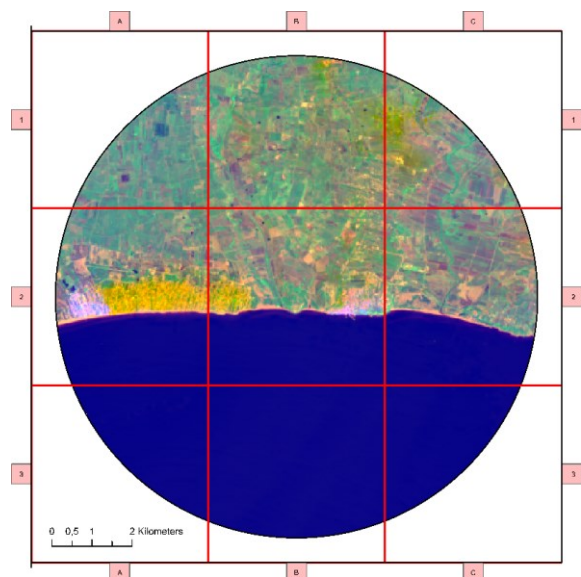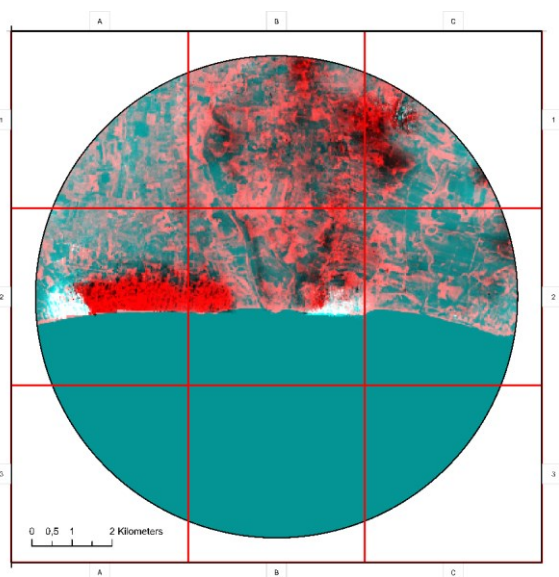
Fig. 33. Optical Imaging fusion: short-wave red (0,636 to 0,673 μm) λ_{red} (446 to 471 THz), near-infrared spectrum (0,851 to 0,879 nm) λ_{NIR} (341 to 352 THz), short-wave infrared region (1,566 to 1,651 μm) λ_{TIRS} (181 to 192 THz) and C-band. Visual configuration: red band stacked with NIR-C-band.
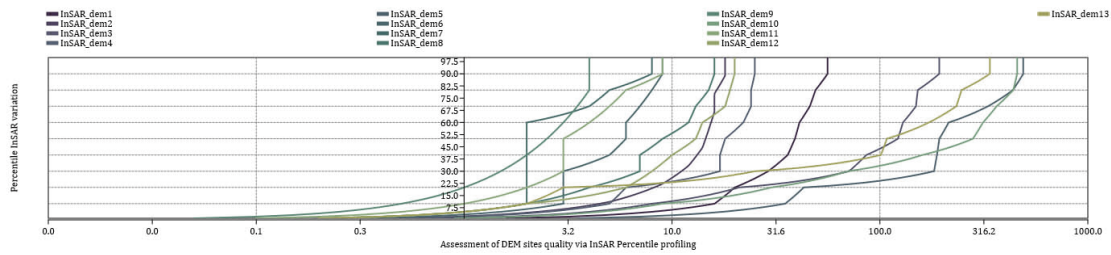
Fig. 34. Synthetic Aperture Radar unwrapped imagery Percentile profiling of the evaluated sites.
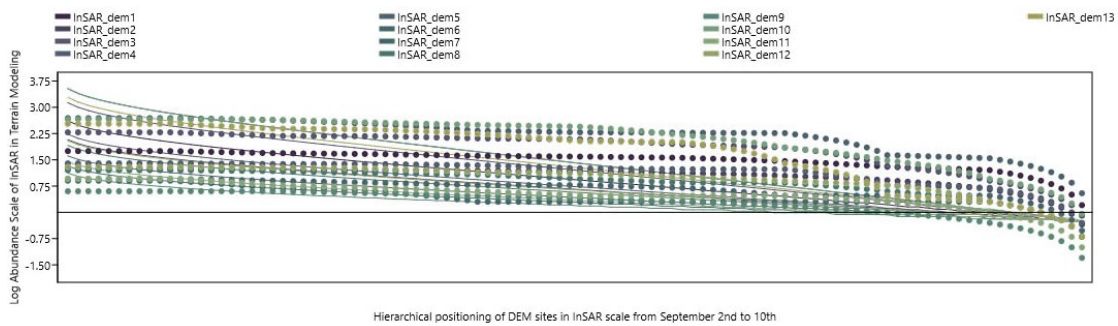
Fig. 35. Crosstab of Synthetic imagery Log scale from the Percentile variation.

	I	II	III	IV	V	VI	VIII	X	XI	XII	XIII
Taxa_S	100	100	100	100	100	100	100	100	100	100	100
Individuals	3591	1238	10343	1689	23766	523	317	904	204	23697	378
Dominance_D	0,01134	0,01065	0,01352	0,01142	0,01438	0,01011	0,01149	0,01177	0,008791	0,01507	0,01143
Simpson_1-D	0,9887	0,9893	0,9865	0,9886	0,9856	0,9899	0,9885	0,9882	0,9912	0,9849	0,9886
Shannon_H	4,523	4,553	4,38	4,507	4,359	4,589	4,553	4,491	4,638	4,286	4,53
Evenness_e^H/S	0,921	0,9491	0,7982	0,9064	0,7819	0,9838	0,9496	0,8924	1,033	0,727	0,9272
Brillouin	4,354	4,14	4,321	4,226	4,329	3,889	3,686	3,99	3,063	4,259	3,584
Menhinick	1,66	2,8	0,9819	2,413	0,6482	4,266	5,472	3,265	6,428	0,6492	4,942
Margalef	12,09	13,9	10,71	13,32	9,825	15,82	17,19	14,54	18,62	9,828	16,68
Equitability_J	0,9821	0,9887	0,9511	0,9787	0,9466	0,9964	0,9888	0,9753	1,007	0,9308	0,9836
Fisher_alpha	19,03	25,41	15,34	23,15	13,36	35,78	48,37	28,33	63,82	13,37	42,17
Berger-Parker	0,01544	0,01411	0,01861	0,01456	0,02055	0,01638	0,02395	0,01706	0,01653	0,01926	0,02198
Chao-1	100	100	100	100,5	100	100	100	100,5	100,5	100	100,5
iChao-1	100	100	100	100,6	100	100	100	100,6	100,5	100	100,5
ACE	100	100	100	100,5	100	100	100,5	100,6	100,5	100	100,5

Chart 9. Synthetic imagery-based ecological diversity assessment:
Σ Log scale analysis of percentile variation in taxonomic indices.

The ecological diversity assessment employs a range of taxonomic indices to analyze species diversity and distribution. Dominance (D) is calculated as $D = \sum_{i=1}^{S}\left(\frac{n_i}{N}\right)^2$, while Simpson's Index (1 - D) and Shannon-Wiener Index (H) provide insights into species evenness and richness, with Evenness measures how evenly individuals are distributed among species; Fisher's Alpha for sample XII is remarkably high at 63.82, indicating significant species richness: these indices, analyzed matricially, leverage log scale analysis for percentile variation, enhancing the precision of biodiversity assessments.
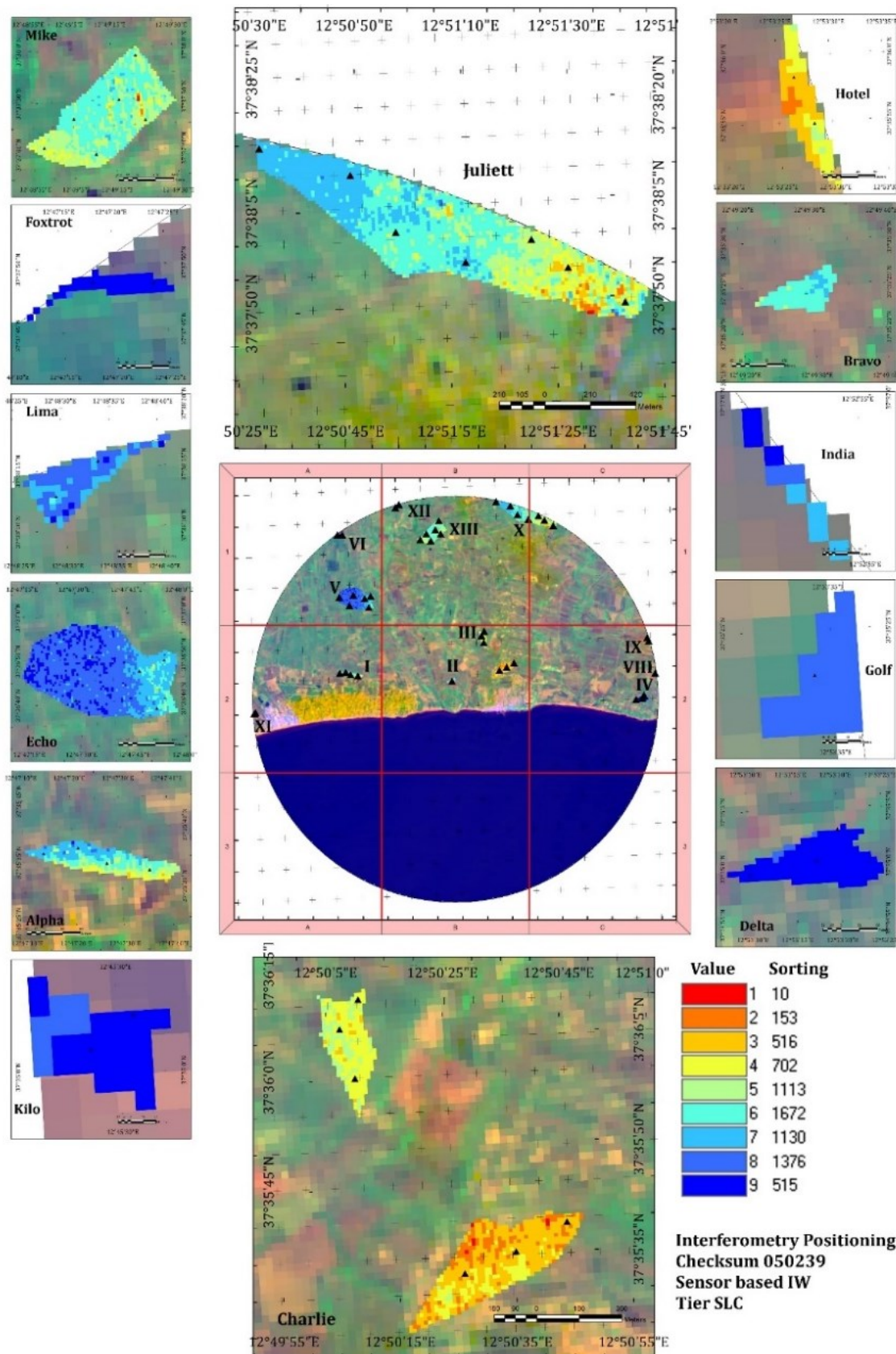
Fig. 36. Prospected assignation: Short-Term SAR interferometric analysis across strategic locations.

Sector	Jargon	Sub-Category	Lan	Long	Landmark
A-02	I-Alpha	01	37°35'36.83"N	12°47'20.78"E	Tree crops
		02	37°35'32.78"N	12°47'35.26"E	Tree crops
		03	37°35'36.07"N	12°47'13.71"E	Barren land (desert)
		04	37°35'34.13"N	12°47'26.64"E	Barren land (building)
B-02	II-Bravo	01	37°35'24.21"N	12°49'28.61"E	Barren land (desert)
B-02	III-Charlie	01	37°35'35.45"N	12°50'35.19"E	Barren land (building)
		01	37°35'32.69"N	12°50'26.25"E	Tree crops
		02	37°35'39.16"N	12°50'44.12"E	Tree crops
B-02	IV-Delta	01	37°35'59.81"N	12°50'8.73"E	Tree crops
		02	37°36'6.63"N	12°50'6.44"E	Barren land (desert)
		03	37°36'10.65"N	12°50'9.79"E	Tree crops
C-02	V-Echo	01	37°35'24.11"N	12°49'28.59"E	Barren land (desert)
		01	37°35'0.27"N	12°53'17.06"E	Horticolture
		02	37°34'59.27"N	12°53'9.59"E	Tree crops
A-01	VI-Foxtrot	03	37°35'3.03"N	12°53'19.57"E	Horticolture
		01	37°36'48.89"N	12°47'54.33"E	Tree crops
		02	37°36'37.92"N	12°47'51.74"E	Tree crops
		03	37°36'46.60"N	12°47'47.24"E	Tree crops
		04	37°36'40.42"N	12°47'28.74"E	Tree crops
		05	37°36'50.16"N	12°47'33.90"E	Tree crops
A-01	VII-Golf	06	37°36'48.74"N	12°47'16.76"E	Tree crops
		01	37°37'48.34"N	12°47'23.31"E	Barren land (desert)
C-02	VIII-Hotel	02	37°37'48.59"N	12°47'17.50"E	Forest
C-02	IX-India	03	37°35'24.88"N	12°53'31.31"E	Horticolture
		01	37°35'58.32"N	12°53'26.11"E	Barren land (desert)
C-01	X-Juliett	02	37°35'54.85"N	12°53'27.86"E	Forest
C-01		01	37°37'49.29"N	12°51'38.29"E	Herbaceous crops
C-01		02	37°37'59.25"N	12°51'21.11"E	Tree crops
B-01		03	37°37'56.23"N	12°51'8.65"E	Tree crops
B-01		04	37°38'1.09"N	12°50'55.69"E	Barren land (desert)
B-01		05	37°38'9.87"N	12°50'47.61"E	Horticolture
B-01		06	37°38'14.44"N	12°50'30.66"E	Tree crops
A-02	XI-Kilo	07	37°35'0.45"N	12°45'28.77"E	Barren land (desert)
		08	37°35'1.29"N	12°45'30.11"E	Barren land (desert)
B-01	XII-Lima	09	37°38'12.63"N	12°48'28.73"E	Tree crops
		10	37°38'15.42"N	12°48'28.73"E	Tree crops
B-01	XIII-Mike	01	37°37'58.41"N	12°49'20.45"E	Tree crops
		02	37°37'49.85"N	12°49'15.96"E	Tree crops
		03	37°37'45.79"N	12°49'22.25"E	Barren land
		04	37°37'46.44"N	12°49'4.74"E	Tree crops
		05	37°37'39.34"N	12°49'9.91"E	Tree crops
		06	37°37'41.00"N	12°48'57.18"E	Forest

Chart 10. Array of designed short-duration spatial dynamics with key-features points.
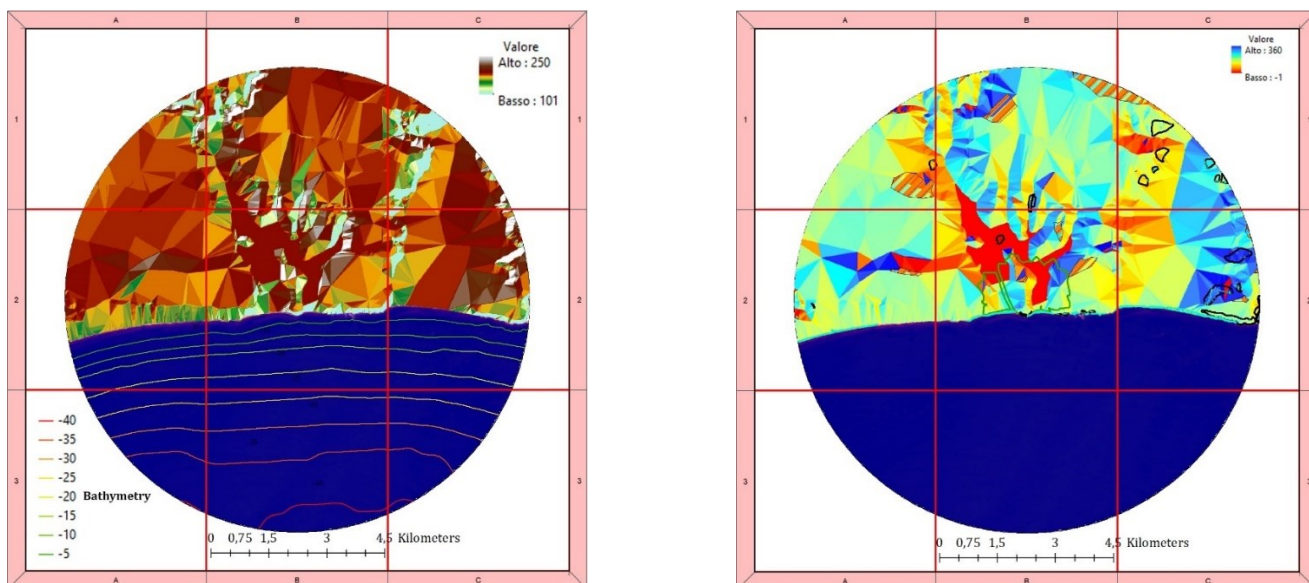
Fig. 37. 3D scale recognition : reconnaissance of shadows and highlights with bathymetric Area of Interest. **Fig. 38.** Terrain from microclimate from microclimate variances: directions [360 to -1] compassing emerging necessity of environmental field remote sensing.
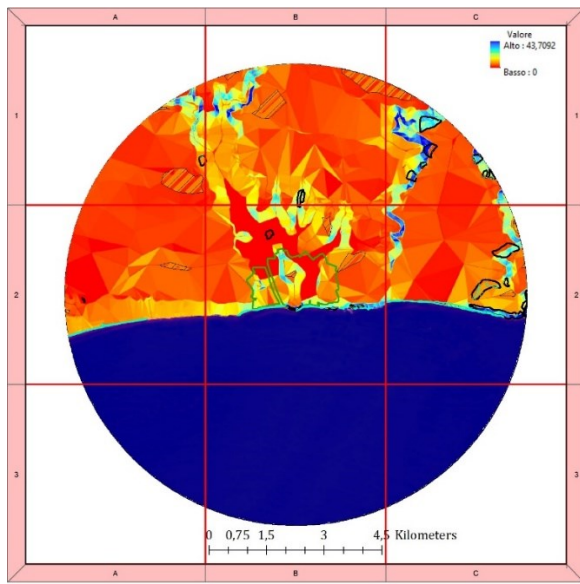
Fig. 39. Slope (43,7092 to 0). **Fig. 40.** 150 x 150 pattern overlay on hillshade model (Mean 196,8497 – Kurtosis 1,05254). **Fig. 41.** Slope (Mean 146,5307 – Kurtosis -0,3433341). **Fig. 42.** Aspect (Mean 198,5729 – Kurtosis 22,61299).
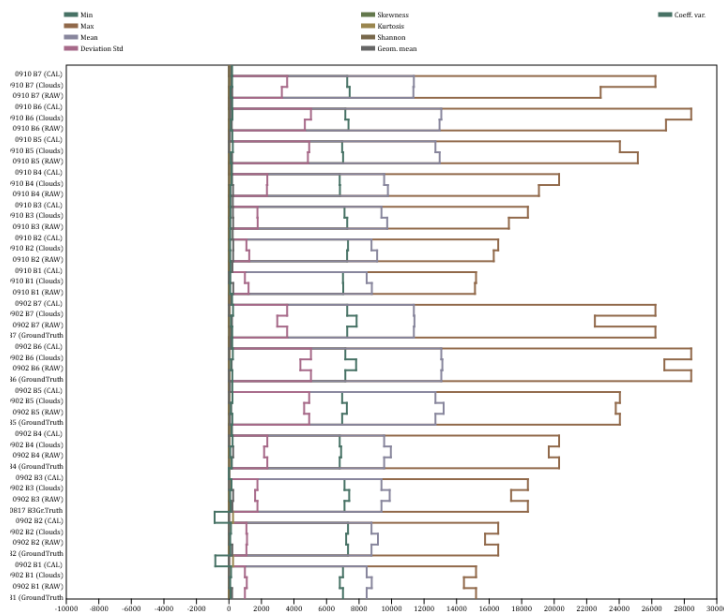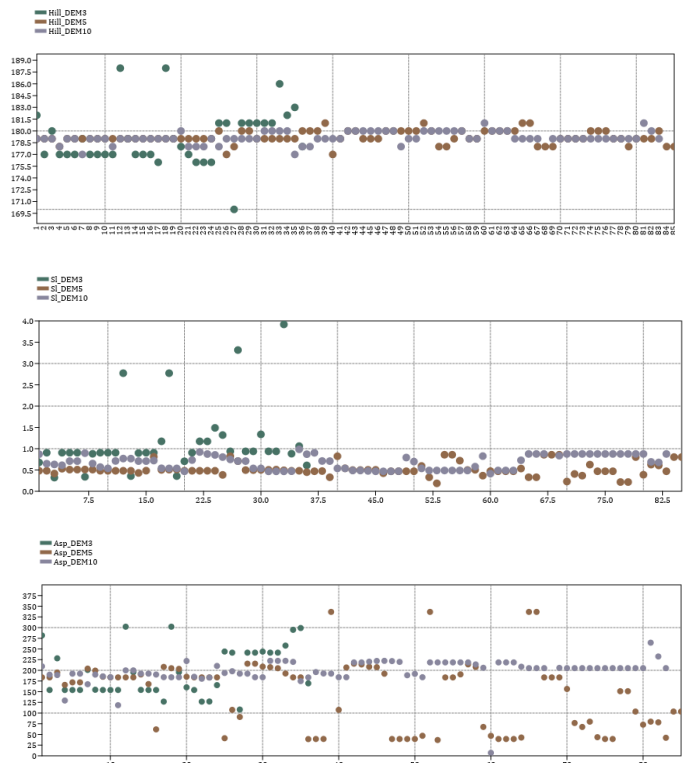

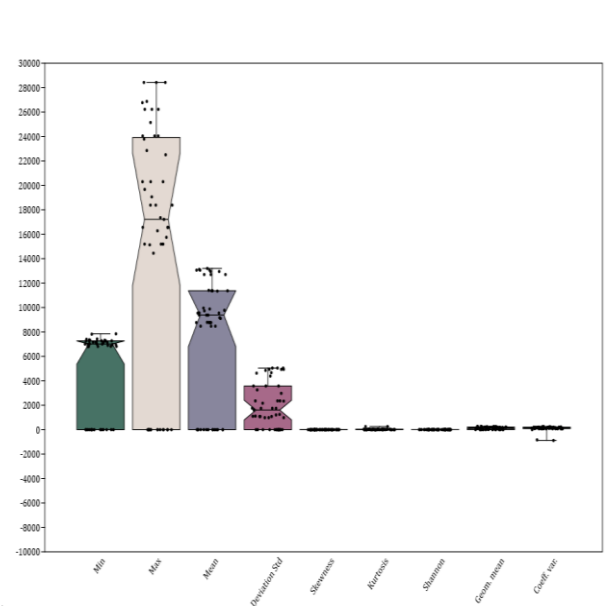**Fig. 43.** Graphical Multispectral Band statistics.

Fig. 44. Box plot of Multispectral Band statistics.

Bands	ϵ	Ω	μ	σ	γ	κ	H	$\bar{G}$	Cv
0817 CoAe (GT)	7011,00	15192,00	8472,85	983,46	0,848997	-0,7678329	5,039	197,1931	101,8783
0902 CoAe (RAW)	6817,00	14449,00	8777,74	1097,82	0,360476	-1,03935	8,284	13,67823	76,66139
0902 CoAe (Clouds)	7011,00	15192,00	8472,93	983,46	2,410191	7,934875	7,86	10,74627	129,2168
0902 CoAe (CAL)	-0,2052	-0,0405	-0,0699	0,0198	-16	256	2,874737E-05	0	-833,234
0817 Blue (GT)	7322	16561	8767,22	1078,33	0,4634417	-1,319235	5,124	210,0816	88,27259
0902 Blue (RAW)	7209,00	15747,00	9163,39	1111,92	0,42	-0,99	0,42	12,95	79,57
0902 Blue (Clouds)	7322	16561	8767,22	1078,33	2,74	11,46	8,04	10,87	119,40
0902 Blue (CAL)	-0,23278	-0,0477	-0,0758	0,0271	-16	256	4,116062E-05	0	-882,8569
0817 Green (GT)	7107	18384	9379,03	1752,15	1,313564	1,39661	5,075	215,528	101,9079
0902 Green (RAW)	7397	17354	9882,01	1607,12	0,4228909	-1,098504	5,251	261,4717	74,05874
0902 Green (Clouds)	7107	18384	9379,11	1752,14	4,110254	20,51869	8,235	7,974093	155,9716
0902 Green (CAL)	-0,269496	-0,0424258	-0,88176	0,03528	-1,005904	-2,01581	1,69935E-36	0	-2,351482E-13
0817 Red (GT)	6814	20302	9546,25	2359,88	4,250454	21,74095	4,783	175,4047	166,5431
0902 Red (RAW)	6901	19670	9954,50	2167,75	0,6614615	-0,2947815	5,24	261,3707	76,79214
0902 Red (Clouds)	6814	20302	9546,25	2359,88	5,372637	31,52498	8,107	5,664251	224,7959
0902 Red (CAL)	-0,3081158	-0,0365261	-0,0915437	0,0475176	4,150801	20,44218	4,825	187,5293	160,9074
0817 NIR (GT)	6963	24043	12701,38	4937,12	4,684846	26,57049	4,395	65,85089	211,9441
0902 NIR (RAW)	7254	23791	13200,92	4627,98	1,175427	0,6356589	4,914	138,2284	114,8425
0902 NIR (Clouds)	6963	24043	12701,38	4937,12	4,990276	26,52615	8,09	5,645483	218,6962
0902 NIR (CAL)	-0,38344	-0,03953	-0,1551	0,0994	4,589816	25,45077	4,417	64,9601	207,8226
0817 SWIR-1 (GT)	7161	28426	13059,75	5045,67	5,647227	36,80826	4,561	0	207,7635
0902 SWIR-1 (RAW)	7819	26775	13122,42	4390,82	2,200439	5,741605	4,947	169,4318	122,3979
0902 SWIR-1 (Clouds)	7161	28426	13059,75	5045,67	5,909307	37,1919	8,405	4,870568	238,4439
0902 SWIR-1 (CAL)	-0,471698	-0,0435131	-0,1622883	0,101598	5,452909	33,84052	4,599	104,7003	201,775
0817 SWIR-2 (GT)	7275	26227	11370,86	3576,71	5,814809	38,90756	4,627	132,7594	203,7823
0902 SWIR-2 (RAW)	7849	22507	11410,05	2974,66	2,190589	5,398779	4,974	184,3207	119,964
0902 SWIR-2 (Clouds)	7275	26227	11370,86	3576,71	6,321866	42,70411	8,296	4,959209	251,768
0902 SWIR-2 (CAL)	-0,4274197	-0,0458086	-0,1282814	0,072019	5,708649	37,05582	4,69	146,0719	195,6877
0910 CoAe (RAW)	7029	15133	8788,61	1207,68	1,090714	0,9542914	5,228	268,7501	81,66327
0910 CoAe (Clouds)	7011	15192	8472,85	983,45	1,17318	2,906377	5,148	0	89,78762
0910 CoAe (CAL)	0,0671775	0,340464	0,1160107	0,0328523	0,7627213	-0,9094495	5,094	217,4795	95,62494
0910 Blue (RAW)	7266	16284	9109,72	1250,12	0,6874725	-0,7131403	5,216	259,4163	80,8569
0910 Blue (Clouds)	7322	16561	8767,22	1078,33	1,492116	8,879081	5,276	269,5273	72,94277
0910 Blue (CAL)	0,0775664	0,38619542	0,12584418	0,03602173	0,3793291	-1,373921	5,175	231,5339	82,45927
0910 Green (RAW)	7273	17216	9730,17	1766,45	0,7585656	-0,8400399	5,197	258,6482	84,49055
0910 Green (Clouds)	7107	18384	9379,11	1752,14	1,205485	1,113891	5,165	245,6592	91,02322
0910 Green (CAL)	0,07038437	0,44709274	0,146154970	0,0585541	1,274189	1,351546	5,127	237,3757	95,98484
0910 Red (RAW)	6823	19062	9775,01	2340,26	1,521981	2,74975	5,149	249,1007	95,05257
0910 Red (Clouds)	6814	20302	9546,25	2359,88	4,058175	19,66943	4,86	194,4631	155,3401
0910 Red (CAL)	0,0605967	0,511163592	0,1518676	0,0788318	4,150838	20,44056	4,825	187,5302	160,9183
0910 NIR (RAW)	7017	25147	12956,56	4855,17	1,531736	2,084467	4,914	192,1148	111,1682
0910 NIR (Clouds)	6963	24043	12701,38	4937,12	5,108715	31,81885	4,215	0	237,2898
0910 NIR (CAL)	0,06557403	0,6361317634	0,257264712	0,16492465	4,589816	25,45077	4,417	64,9601	207,8226
0910 SWIR-1 (RAW)	7352	26876	12950,48	4670,12	2,055878	7,804224	5,03	176,3704	106,8967
0910 SWIR-1 (Clouds)	7161	28426	13059,75	5045,67	5,804482	38,77759	4,489	92,33521	218,6328
0910 SWIR-1 (CAL)	0,07218822	0,7825498	0,2692360	0,16855083	5,452909	33,84052	4,599	104,7003	201,775
0910 SWIR-2 (RAW)	7425	22856	11344,75	3254,85	1,80901	5,908038	5,092	204,8656	99,28675
0910 SWIR-2 (Clouds)	7275	26227	11370,86	3576,71	5,572141	35,20622	4,701	148,687	193,212
0910 SWIR-2 (CAL)	0,07599639	0,709088325	0,212818632	0,11948001	5,708649	37,05582	4,69	146,0719	195,6877

Chart 11. Key statistics to two decimal places.

	ϵ	Ω	μ	σ	γ	κ	H	$\bar{G}$	Cv
Ni	49	49	49	49	49	49	49	49	49
min	-0.471698	-0.0477	-0.88176	0.0198	-16	-2.01581	1.7E-36	0	-882.8569
max	7849	28426	13200.92	5045.67	6.321866	256	8.405	269.5273	251.768
$\Sigma_{i=1}^{n} a_i$	250388.2	730275.5	370058.3	96523.71	105.3935	1208.499	246.8051	6341.85	4892.689
μ	5109.963	14903.58	7552.21	1969.872	2.150888	24.66325	5.036838	129.4255	99.85079
$\bar{\sigma}_x$	467.4466	1468.067	720.5652	258.2919	0.6171654	7.214547	0.2764394	14.00261	29.75748
σ^2	1.070681E07	1.056058E08	2.544149E07	3269020	18.66376	2550.435	3.744519	9607.575	43389.89
σ	3272.126	10276.47	5043.956	1808.043	4.320158	50.50183	1.935076	98.01824	208.3024
M	7011	17216	9379.03	1607.12	2.190589	8.879081	5.03	146.0719	119.4
P_{50}	0.07409231	0.67261	0.2350417	0.1422023	0.8058592	0.7949752	4.613	10.80814	86.38157
P_{75}	7269.5	23917	11370.86	3576.71	5.049496	32.82969	5.222	212.8048	201.775
γ	-0.9645762	-0.5072941	-0.6877186	0.5290379	-3.071365	4.125047	-0.7101162	-0.1345193	-4.172452
κ	-1.093407	-1.228123	-1.17715	-1.100732	11.67268	17.62181	2.130896	-1.52992	18.0435
$\bar{G}$	0	0	0	114.7255	0	0	0.5612674	0	0
Cv	64.03424	68.95301	66.78781	91.78482	200.8546	204.7655	38.41847	75.73332	208.6137

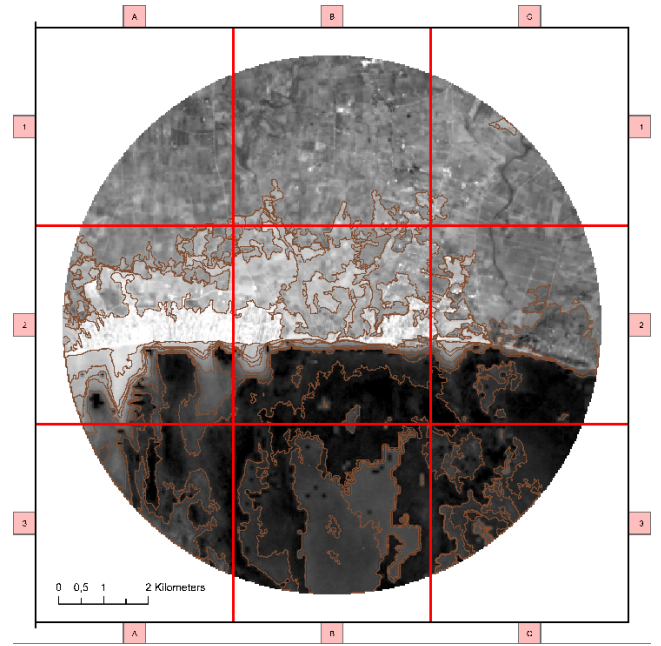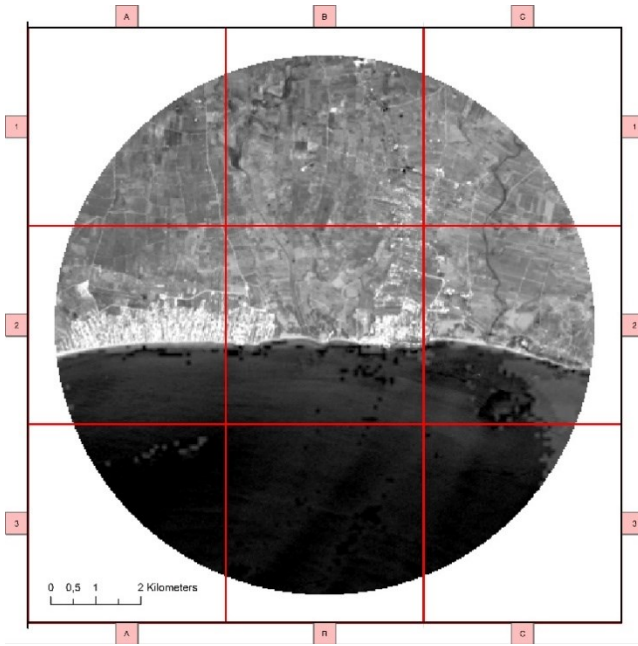**Chart 12.** Contingency table of the multi-spectral solutions deployed.

Fig. 45. 0.435-0.451 µm blue band from baseline data Ground Truth 17th August.
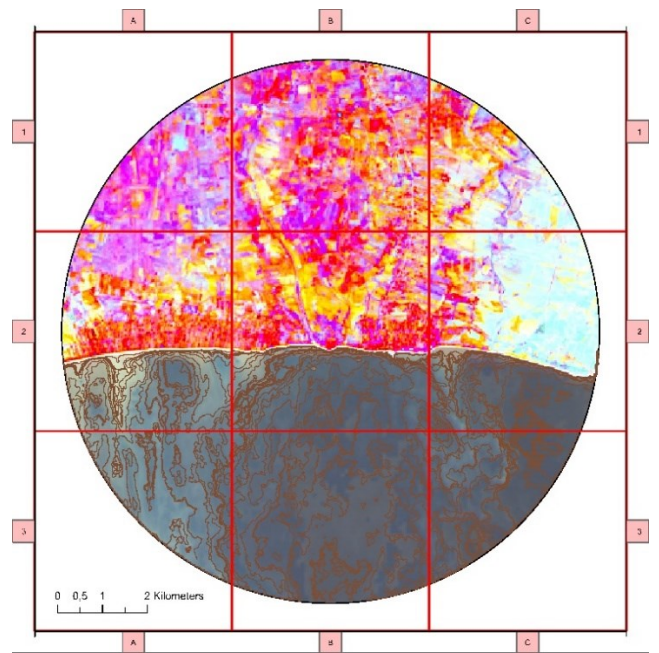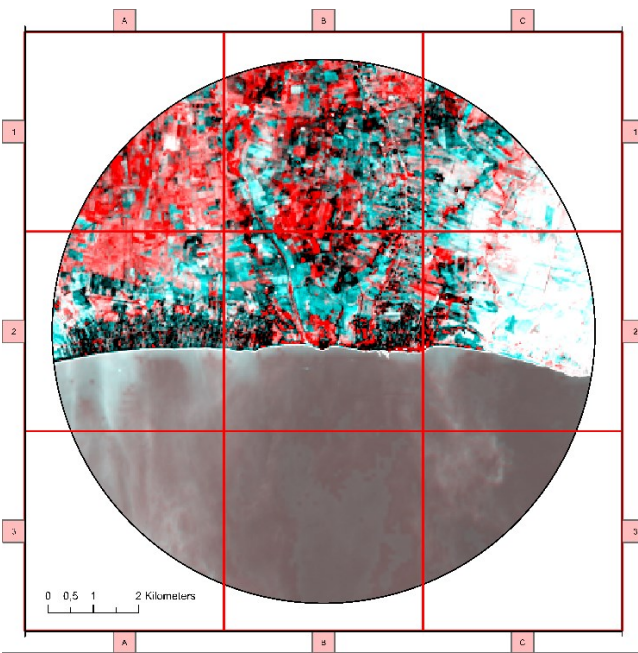**Fig. 46.** 0.435-0.451 µm blue band from 10th September.

**Fig. 47.** Colour Infrared solution from 10th September.
Fig. 48. Red-*NIR-SWIR* 1 from 10th September.

In the domain of remote sensing, particularly in the processing of Landsat 8 imagery, the conversion of raw satellite data to Top of Atmosphere (TOA) reflectance is a critical step: this process is encapsulated in the formulation of:

$$\rho'_{\lambda} = M_{\rho\lambda} \times Q_{cal} + A_{\rho\lambda} \times \frac{\int_{-\infty}^{+\infty} e^{-x^2}}{\sqrt{2\pi}} + \lim_{n \to \infty}\left(\frac{1}{n}\sum_{i=1}^{n}f(i)\right) - \nabla \cdot \vec{F}$$

Equation 6. Correction factors and calibration.

Where ρ'_λ represents the TOA planetary reflectance prior to any correction for the solar angle. The coefficients $M_{\rho\lambda}$ and $A_{\rho\lambda}$ are the multiplicative and additive rescaling factors, instrumentally trusted in transforming the Quantized and Calibrated Standard Product Pixel Values, denoted as Q_{cal}, into a reflectance value that is scientifically usable for further analysis, albeit uncorrected for the angle of solar illumination; additionally the formula approaches the Gaussian integral, a fundamental integral in probability theory and statistics, a limit expression, representing the average of a function $f(i)$ over an infinite sequence, hereby subtracted to add depth and complexity and a divergence term $\nabla \cdot \vec{F}$ to introduce a vector calculus element.
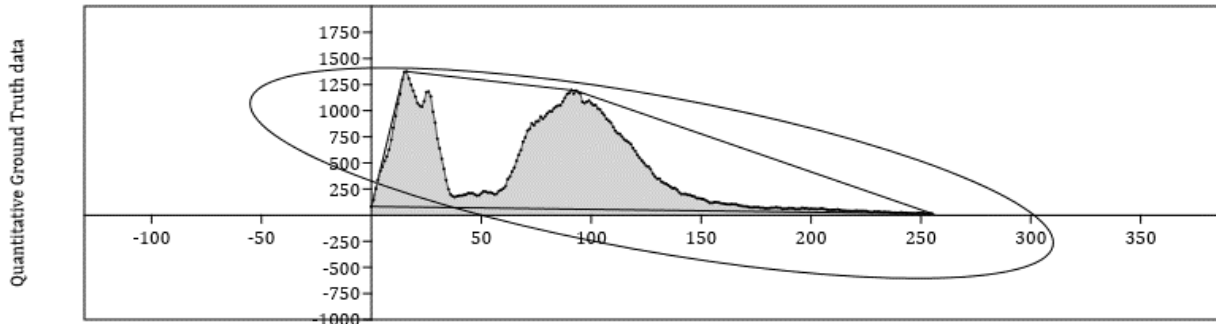
Pixel value in Landsat OLI_TIRS 8 Band 1: August 18th LC08_L2SP_190034_20230817_20230822_02_T1

Fig. 49. Reference sensing data: Short-wave blue.
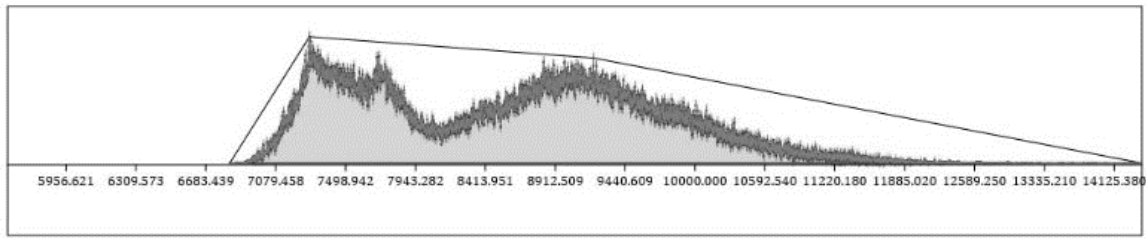
Pixel value in Landsat OLI_TIRS 8 Band 1: September 2nd LC08_L2SP_190034_20230902_20230912_02_T1

Fig. 50. Short-wave 0.435-0.451 μm from 2nd September ($\gamma = 2{,}41$; $\kappa = 7{,}93$; $\bar{G} = 10{,}75$; $C_v = 129{,}22$).

Pixel value dynamics in Landsat OLI_TIRS 8 Band 1: September 2nd Raw data vs Cloud-Removed data distribution
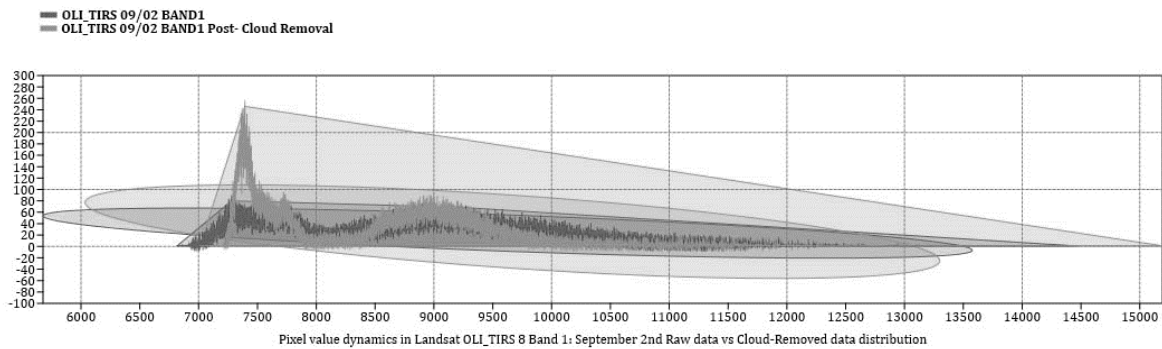
Fig. 51. Sensing comparison: data distribution resulted from TOA-Cloud operations (Zhou, Guanhua et al., 2023).

Pixel value distribution Post-TOA Calibration of Landsat 8 OLI_TIRS Band 1 on September 2nd
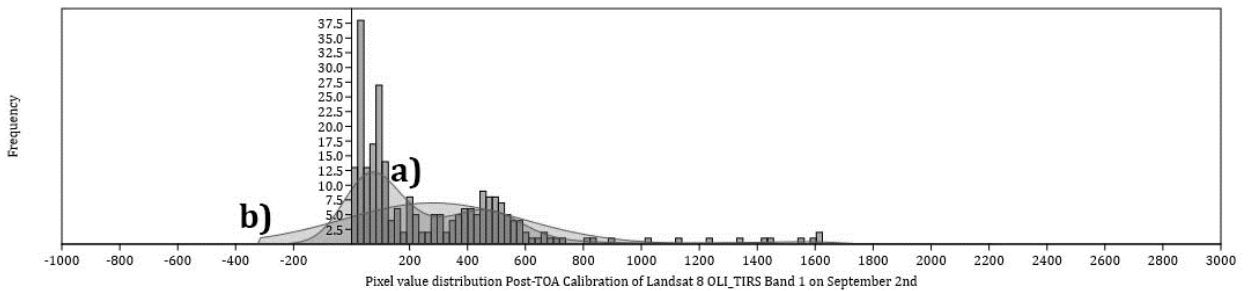
Fig. 52. A) kernel density b) normal distribution.

3.3. DEM sites: EW Eigen-Response Potentiality Measures (ERPM)

In the realm of antenna installation planning, the meticulous analysis of Digital Elevation Models (DEMs) derived from Voronoi confinements is indispensable: this analysis, grounded in data from Interferometric Synthetic Aperture Radar (InSAR) computations, reveals critical insights into the terrain subsidence of various areas, crucial for strategic antenna placements. The data from Sentinel-1A spans a range of demographics, Dem1 through Dem13, each presenting unique elevation profiles.

Dem1 showcases a relatively consistent terrain, with elevation values ranging from a minimum of 16 to a maximum of 56. This suggests a relatively uniform landscape, potentially ideal for straightforward antenna placements.

Dem5, in stark contrast, exhibits a broad elevation spectrum, ranging from 35 to a whopping 489. Such dramatic topographical diversity could present both challenges and opportunities, necessitating careful site selection to optimize coverage and signal strength.

Dem3 and Dem10 stand out with their high median values of 122 and 280, respectively, and wide ranges (8 to 193 for Dem3 and 9 to 457 for Dem10). These areas likely present varied and complex landscapes, potentially offering multiple viable sites for antenna installations, each with its unique advantages and challenges.

Dem6 and Dem7 display remarkably narrow elevation ranges (3 to 9), indicating highly uniform terrains. Such consistency could simplify the process of antenna siting, though it might limit options for elevation-based optimization.

Dem9 and Dem11, with their very low ranges (1 to 4 and 1 to 9, respectively), might represent more homogenous areas, possibly with limited topographical variation, which could streamline the site selection process but might also limit the opportunities for leveraging elevation for signal propagation.

Dem13 presents a particularly intriguing case with its wide range (2 to 338) and high median value of 108: this scenario suggests a complex terrain with significant elevation differences, which could impact the feasibility and performance of antenna installations.

Hence, Sentinel-1A InSAR data provides an indispensable tool in this analysis, offering precise measurements of terrain movement and alteration over time: the integration of this data with topographical understanding is crucial for making informed decisions about antenna installations.

It's not just limited within a numerical evaluation, whether the highest or most stable point available: it's about understanding the entirety of the landscape, its changes, and how these factors interact with the technological and environmental aspects of antenna installation; this analysis transcends the mere mathematical accomplishments, necessitating human expertise and environmental consideration to ensure sustainable and effective antenna placement strategies.
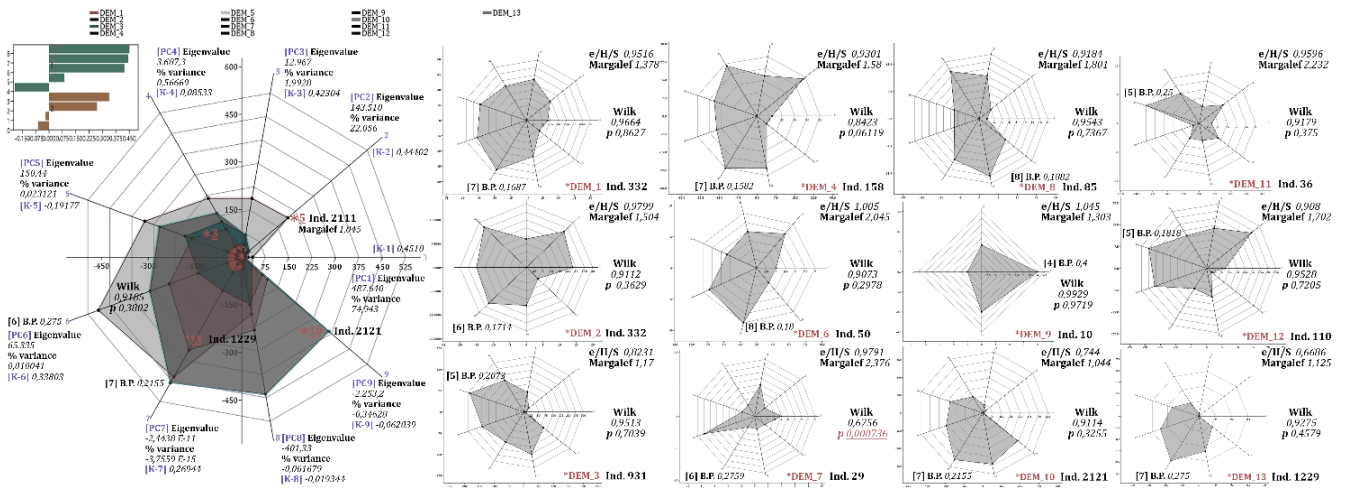
Fig. 53. EW Eigen-Response Potentiality Measures (ERPM). Ψ reduction – Ω multiscale evaluation.

In the case of the Digital Elevation Model (DEM) data derived from Interferometric Synthetic Aperture Radar (InSAR), PCA can be particularly insightful: this analysis focuses on the eigenvalues and the percentage variance explained by each principal component (PC), along with the loadings of each DEM site on these components.

The eigenvalues and the percentage of variance explained by the first nine principal components (PC 1 to PC 9) show a steep decline in their values.
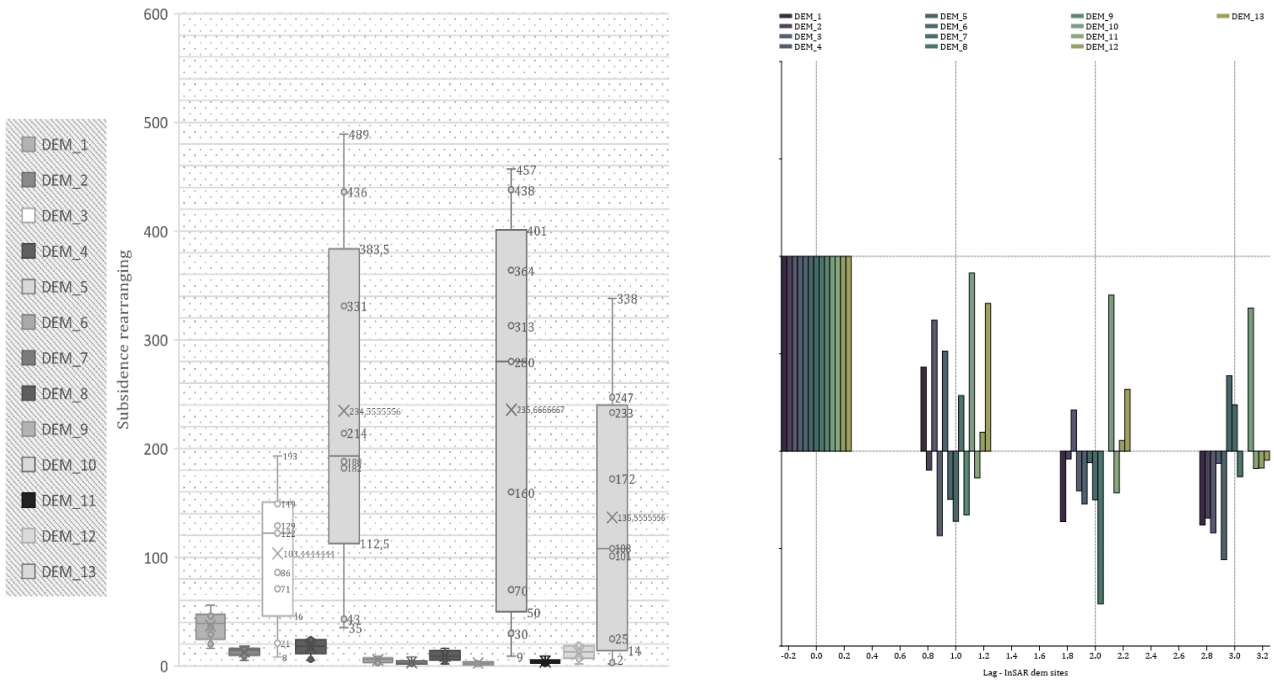
Fig. 54. Bar Charts and Box Plots for DEM sites InSAR Categorization. **Fig. 55.** Autocorrelation subsidence.
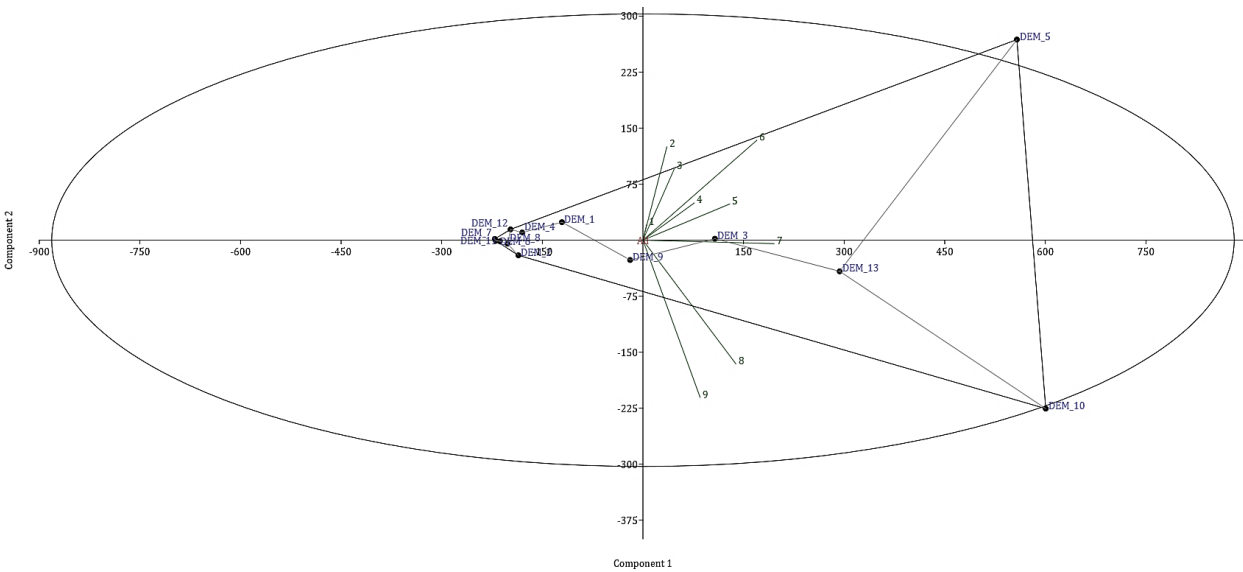
Fig 56. Principal Components Analysis. DEM sites Loadings of subsidence values within 95% ellipses. In the realm of Geographic Information Systems (GIS) and remote sensing, Principal Component Analysis (PCA) is a powerful statistical tool used to reduce the dimensionality of large datasets while preserving most of the variance in the data.

The first principal component (PC 1) has an eigenvalue of 89446.2, accounting for a significant 87.347% of the total variance. This suggests that PC 1 captures most of the variability in the dataset.

The second component (PC 2) explains 10.321% of the variance with an eigenvalue of 10569.4, followed by much smaller contributions from the remaining components (PC 3 to PC 9), which cumulatively contribute to less than 2.5% of the total variance.

The loadings of each DEM site (DEM_1 to DEM_13) on these principal components provide insights into the spatial variability and patterns within the dataset. For instance, DEM_1 has a negative loading on PC 1 (-120.74) and a positive loading on PC 2 (24.1), indicating its unique topographic characteristics compared to other sites. Similarly, each DEM site shows a distinct pattern of loadings across all nine components, reflecting the complex and varied nature of the terrain captured by these DEM sites.

This analysis underscores the utility of PCA in distilling large and complex geospatial datasets into a more manageable form, enabling easier interpretation and identification of key patterns and variations in the data.

3.3.1. Sites Analysis: short-term variation with spectral mixing issues

Evaluating rapid changes in landscapes by overcoming spectral mixing complexities for the antennas allocations, requested higher precision of short-term environmental site analysis as follows.
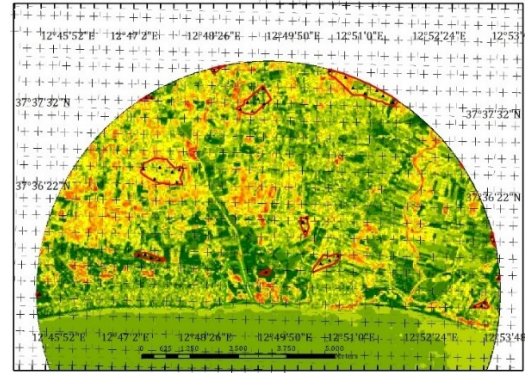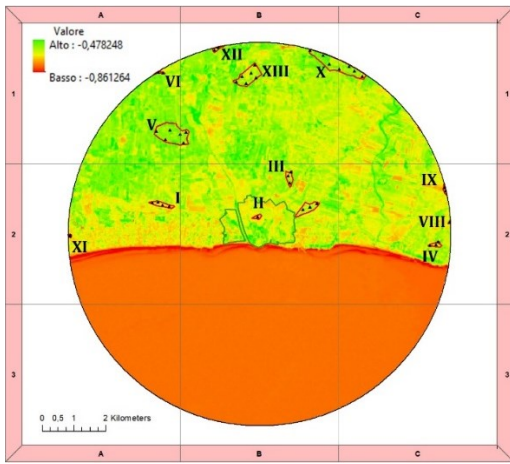
Fig 57. *d*NDVI From -0,478248 to -0,861264. **Fig 58.** *d*NDVI values across nine classes, with OBJECTID 1 (Value 1, Count 5799) to OBJECTID 9 (Value 9, Count 334), highlighting significant variations in vegetation; OBJECTID 3 shows the highest frequency (Value 3, Count 65846), indicating prevalent vegetation changes in this category.
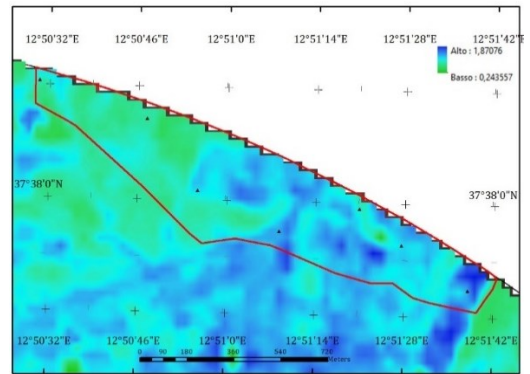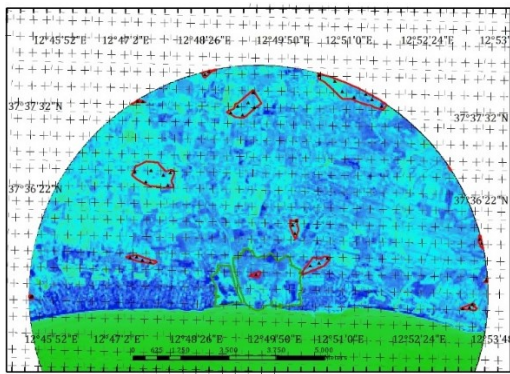
Fig 59. *d*MNDWI at two time frames: Using Landsat's Green Band (Band 3, 0.53-0.59 μm) and *SWIR* Band (Band 6, 1.57-1.65 μm), *d*MNDWI is calculated for two different dates. These dates are chosen based on the period of interest for monitoring short-term changes in water bodies. **Fig 60.** *d*MNDWI for Juliett AOR.
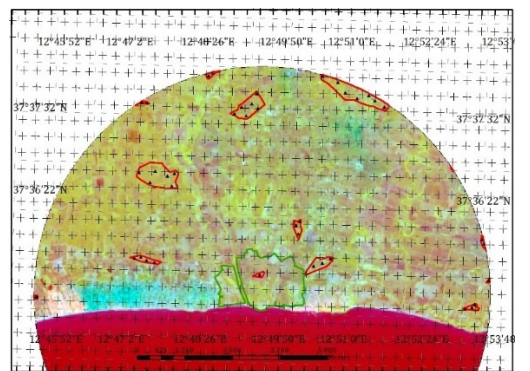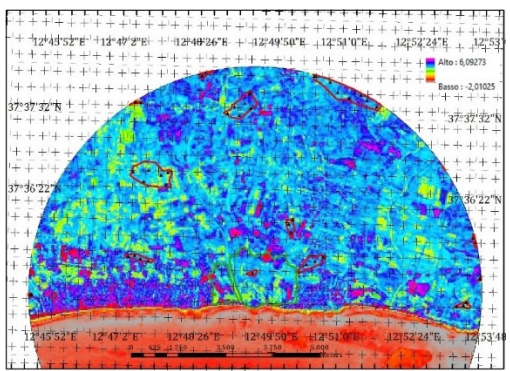
Fig 61. Δ Enhanced Vegetation Index (850 to 880 nm-Red-Blue bands). **Fig. 62.** *d*EVI and *C*-SAR (3,75 to 7,5 cm).
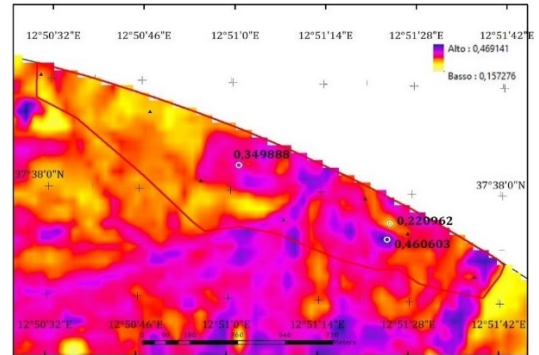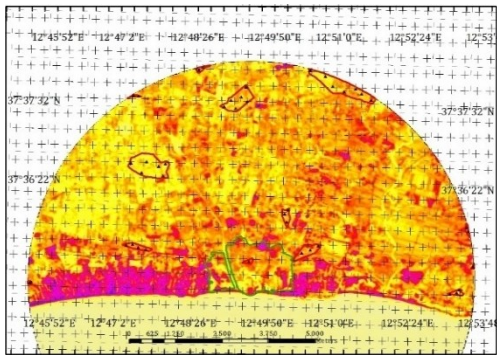
Fig. 63. Δ Soil Adjusted Vegetation Index [*NIR*-Red (L=0,5)]. **Fig. 64.** *d*SAVI Juliett AOR.
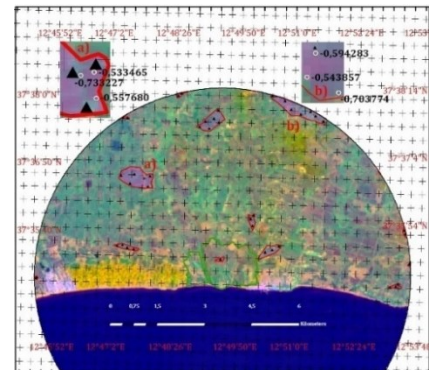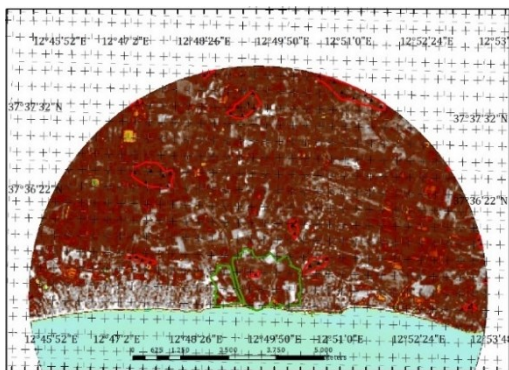
Fig. 65. *d*NDBI. **Fig. 66.** 0.636-0.673 μm-0.851-0.879 μm-1.566-1.651 μm-*C*-SAR vis 0.636-0.673 -0.851-0.879 -*C-SAR.*
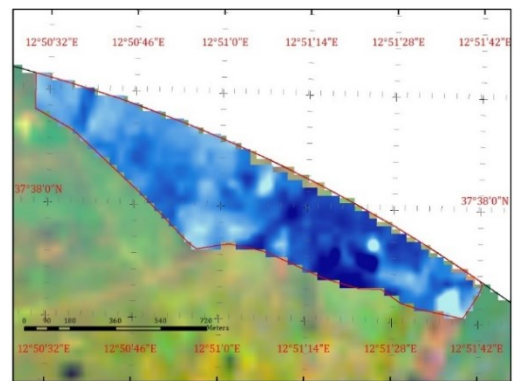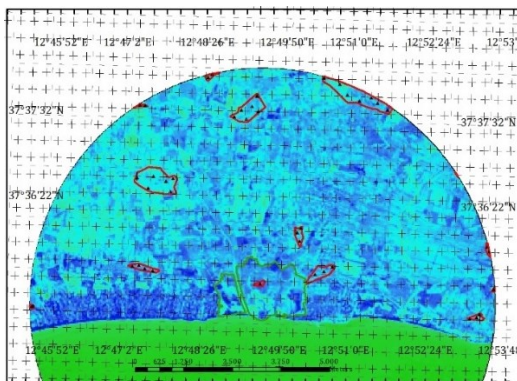
Fig. 67. *d*NDWI 530 to 590 nm-850 to 880 nm. **Fig. 68.** *d*NDWI Juliett AOR.
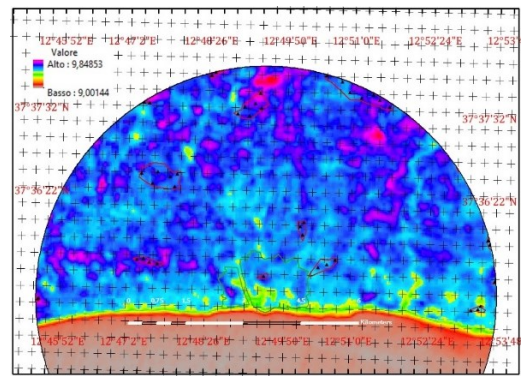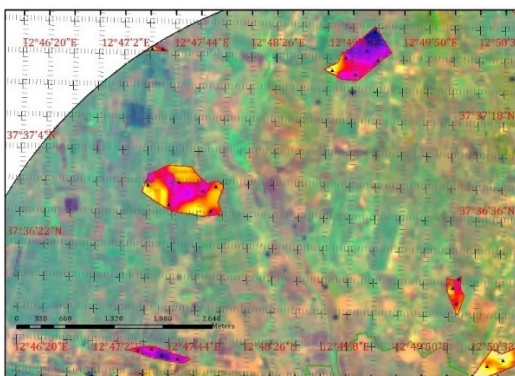
Fig. 69. *d*LST **Fig. 70.** Band 4 (640-670 nm), along with Bands 5 (850-880 nm) and 6 (*SWIR*) vis InSAR-4-5.

3.3.2. Site Modeling : multi-index distribution of indexes values based on Abundance variation

The approach is rooted in the objective of achieving a deeper, more integrated understanding of site-specific environmental characteristics, where the fusion of advanced mathematical constructs and environmental data is established for consistent insights into multi-scalar and replicabile phenomena (DEM VII and IX npt included this time due to raster limitations).

Dominance_D	I	II	III	IV	V	VI	VIII	X	XI	XII	XIII
Taxa_S	0,0901	0,0901	0,0901	0,0901	0,0901	0,09015	0,09015	0,0901	0,09027	0,0901	0,09015
Individuals	0,5457	0,6182	0,571	0,6243	0,5663	0,3863	0,3863	0,4069	0,3588	0,6	0,302

Chart 13. Ecological insights of DEM designations.

Median	I	II	III	IV	V	VI	VIII	X	XI	XII	XIII
Shannon	4,513	4,613	4,488	4,582	4,434	4,556	4,702	4,573	5,119	4,506	4,626

Chart 14. Central tendency insights of DEM designations [H'=−∑(pi×ln pi].

Mean	I	II	III	IV	V	VI	VIII	X	XI	XII	XIII
AC Estimator	99,76	100,44	99,62	99,74	99,54	99,48	99,59	100,24	1889,87	99,57	100,68
Chao-1	99,77	103,45	99,59	99,86	99,54	99,32	99,27	116,77	1889,86	99,54	99,60

Chart 15. Species richness insights of DEM designations.
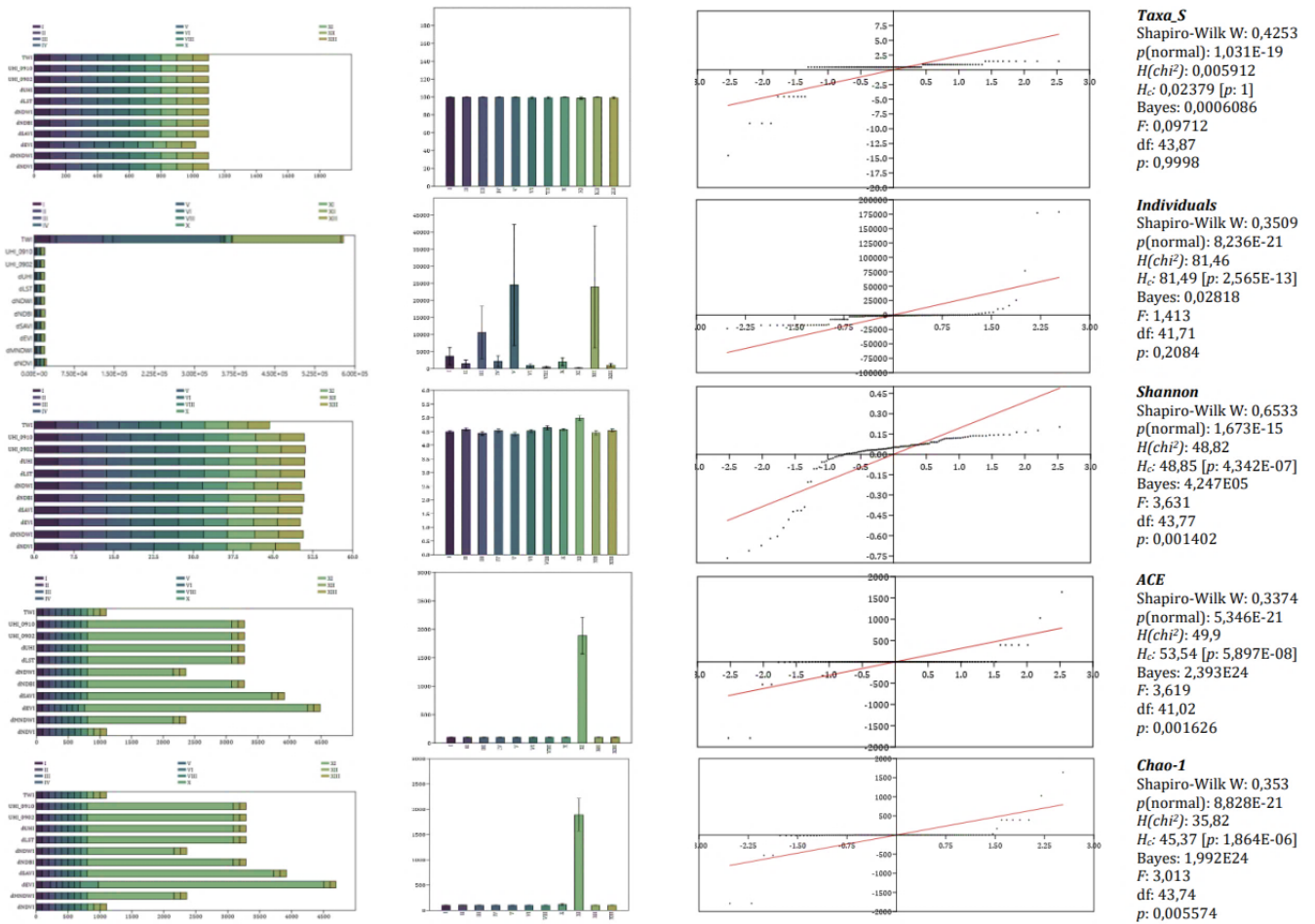
Figures 71. Comprehensive statistical analysis of ecological data from DEM designations.
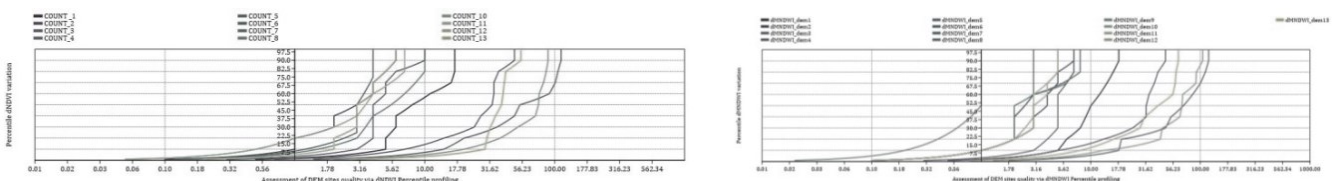
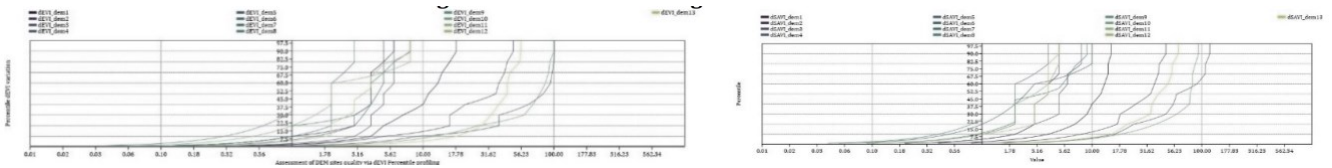**Fig. 72.** Percentile dNDVI. **Fig. 73.** Percentile dMNDWI.

Fig. 74. Percentile dEVI. **Fig. 75.** Percentile dSAVI.
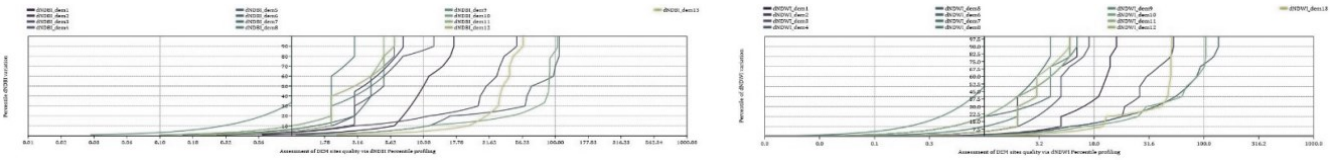

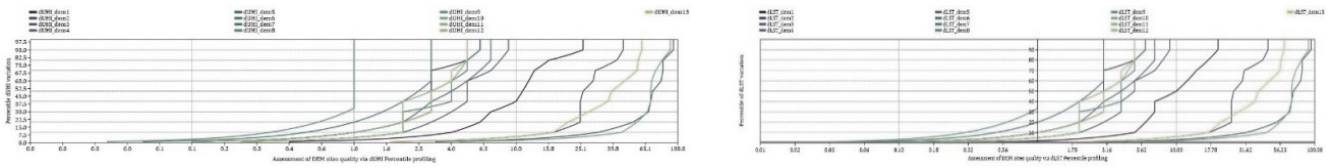**Fig. 76.** Percentile dNDBI. **Fig. 77.** Percentile dNDWI.

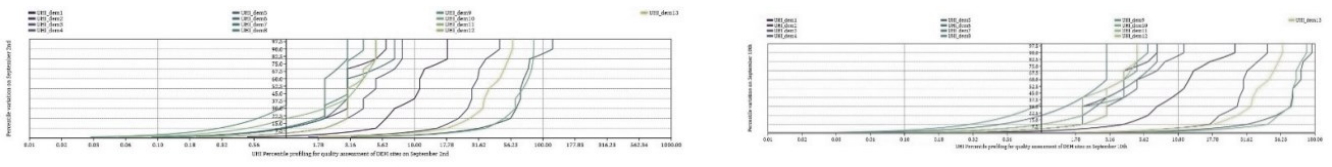**Fig. 78.** Percentile dUHI. **Fig 79.** Percentile dLST.

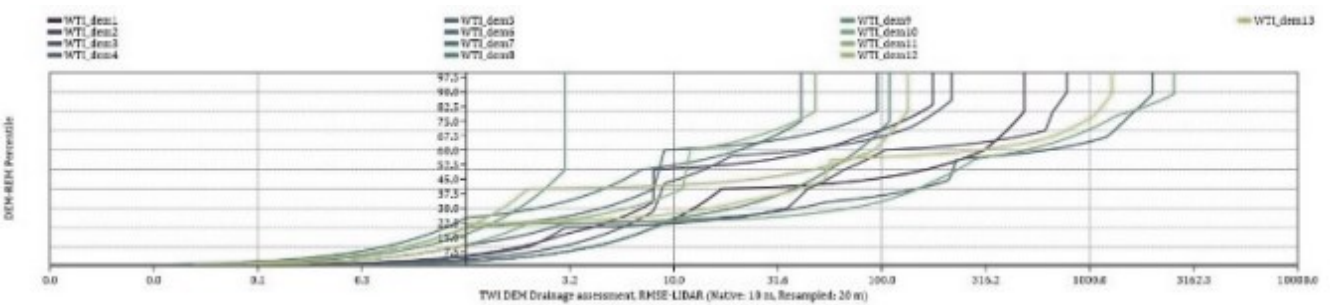**Fig. 80.** Percentile UHI (September 2nd). **Fig. 81**. Percentile UHI (September 10th).

Fig. 82. Percentile WTI.

The p-th percentile of each dataset, which is the value below which p% of the data falls, has been expressed as $P_p = X_{[p(n+1)/100]}$, where for each P_p, each X set has been ordered according to this Region of Intest (ROI) translated into n number of observations, matricially structured (Zekri A., 2014) under $[\cdot]$ ceiling function; the referred transpose was singularly accounted for $(A^T)_{ij}$ equivalent to a_{ij}.

3.3.3. Abundance variation of site modeling: Cross-Tabulating of differential indexes

The incorporation of scaled log abundance in the analysis of differenced sensings within terrain modeling serves to normalize data across diverse densities, aiding in mitigating skewness in the data; this level of detailed spatial analysis provides a complete view of terrain modeling and ecological dynamics, crucial for informed decision-making in environmental stewardship refining land-use planning and conservation within such restricted designations.
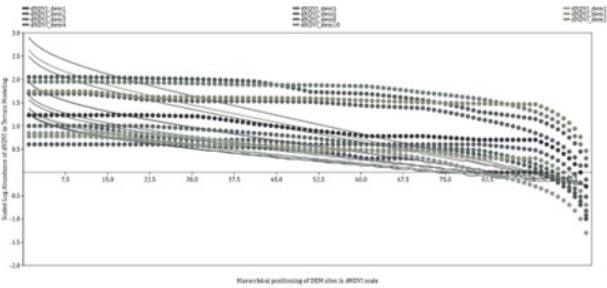
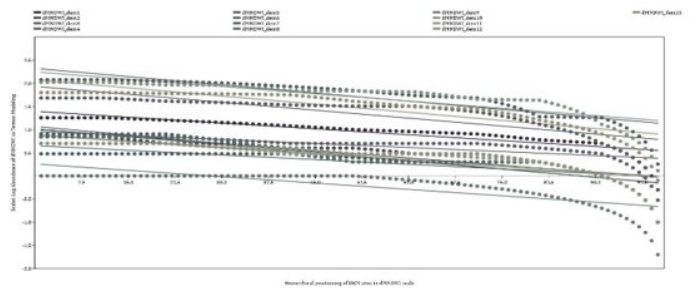**Fig. 83.** Crosstab Logarithmic dNDVI scale. **Fig 84.** Crosstab Logarithmic dMNDWI scale.
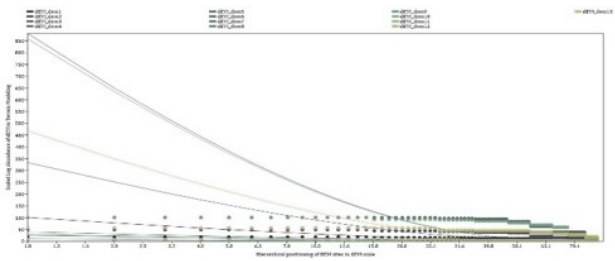
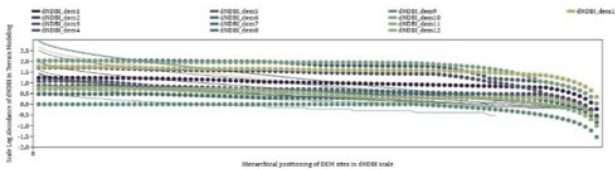**Fig. 85.** Crosstab Logarithmic dEVI scale. **Fig 86.** Crosstab Logarithmic dSAVI scale.
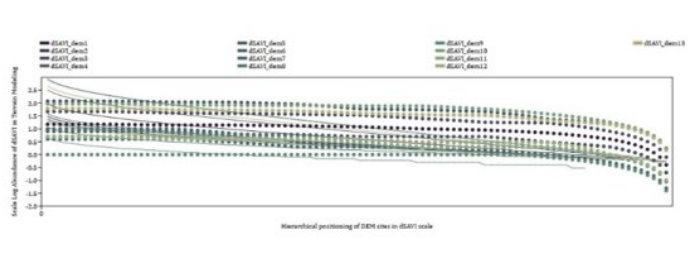

Fig. 87. Crosstab Logarithmic dNDBI scale. **Fig 88.** Crosstab Logarithmic dNDWI scale.
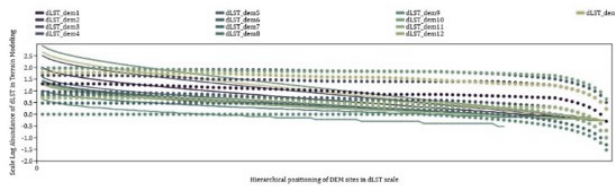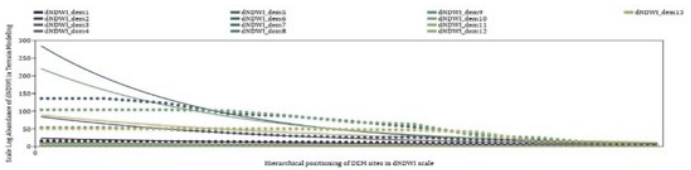

Fig. 89. Crosstab Logarithmic dLST scale. **Fig. 90.** Crosstab Logarithmic dUHI scale.
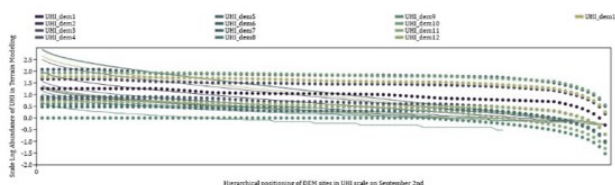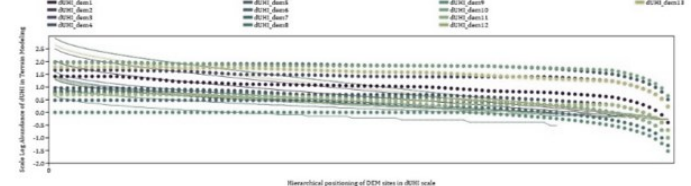

Fig. 91. Crosstab Logarithmic UHI (September 2nd) scale. **Fig. 92.** Crosstab Logarithmic UHI (September 10th) scale.
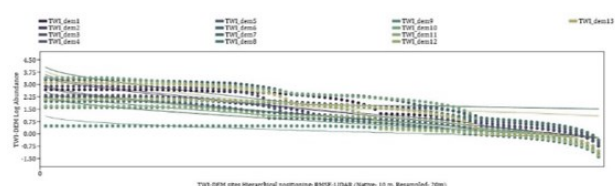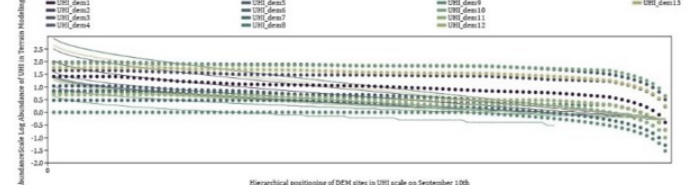

Fig. 93. Crosstab Logarithmic RMSE-LIDAR scale; $I_d = I_{t2} - I_{t1}$ where I_{t2} and I_{t1} denote the index values at times $t2$ and $t1$; $P(x) = \frac{number\ of\ values\ in\ D\ less\ than\ x}{total\ number\ of\ values\ in\ D}$ x 100; all records are combined as such: $C(log(I_{a,d}), log(I_{b,d}))$.

3.3.4. Differential analysis of Land Surface Temperature *Γ-Σ Λ-Δ* multiplicative factors

In the differential Land Surface Temperature (*d*LST) analysis, calibration and scaling factors used in thermal imaging are emphasized. The grid cell size for both reflective and thermal data is uniformly 30.00 units. Radiometric rescaling employs an additive factor (1000*E*-04) and a multiplicative factor (3.3420*E*-04) for converting spectral radiance. For brightness temperature conversion, thermal constants are detailed for TIRS (L2SP) bands 10 and 11, with distinct *K1* and *K2* constants for each band.

     Land Surface Emissivity (LSE) values, represented by Epsilon0902 and Epsilon0910, exhibit minimal variability, indicating consistent surface characteristics. The Proportional Vegetation (PV) values, namely PV02 and PV10, show a broad range but maintain low mean values, signifying limited vegetation cover.

     Lastly, the analysis presents the minimum, maximum, mean, and standard deviation for Land Surface Temperature (LST) during two periods (0902 and 0910), revealing notable temperature fluctuations. The Urban Heat Island (UHI) effect is calculated as the normalized difference between surface temperature (T_S) and mean temperature (T_M), divided by the standard deviation (SD), thus offering a metric for the temperature disparity between urban and rural areas.

GROUP		LEVEL1_RADIOMETRIC_RESCALING	Radiance Scaling Conversion
RADIANCE_ADD_BAND	10-11	1000E-04	Additive scaling factor DN to spectral radiance
RADIANCE_MULT_BAND	10-11	3.3420E-04	Multiplicative factor DN to spectral radiance

Chart 16. *Γ-Σ Λ-Δ* multiplicative (*Λ*) factors.

GROUP		LEVEL1_THERMAL_CONSTANTS	Brightness Temperature Conversion
*K1*_CONSTANT_BAND	10	774.8853	Calibration costant 1 to TIRS band 10
*K2*_CONSTANT_BAND	10	1321.0789	Calibration costant 2 to TIRS band 10
*K1*_CONSTANT_BAND	11	480.8883	Calibration costant 1 to TIRS band 11
*K2*_CONSTANT_BAND	11	1201.1442	Calibration costant 2 to TIRS band 11

Chart 17. *Ω-Θ* calibration.

	Ω	ε	μ	σ
0902(LSE)	0,9860000014305115	0,9900000095367432	0,9872591681037526	0,0007194885775269832
0910(LSE)	0,9900000095367432	0,9860000014305115	0,986910324751142	0,0006715207645538647

Chart 18. *μ-σ.*

	Ω	ε	μ	σ
PV02	1	2,69967e-13	0,3147916464103485	0,179872130262345
PV10	0,9999988079071045	7,95510779103524e-14	0,2275808147060041	0,1678801508871896

Chart 19. PV.

	ε	Ω	μ	σ
LST_0902	55,94025039672852	71,49307250976563	62,19439088848231	5,360355192647313
LST_0910	66,22560882568359	82,62550354003906	72,81779460778476	5,650677602488692

Chart 20. Sensed heat (Celsius).

3.4. Field Reference from differentials : commission errors across user's accuracies

The data presented encompasses a comprehensive analysis of various differential indices like *d*NDVI, *d*EVI, *d*SAVI, *d*NDBI, *d*MNDWI, *d*LST, and *d*TWI, all sampled in three reclassifications - Regeneration, Equilibrium, and Degradation. These indices are used as baseline references for joint examinations, comparing them against field references like unburnt areas, low and high severity zones, and others.

     For example, in the *d*NDVI analysis using *d*EVI as a baseline, the majority of data points fall under the Degradation category, with high commission and omission errors, resulting in a low kappa coefficient of 0.048. This indicates a moderate agreement beyond chance.

     In contrast, the examination with *d*LST as a baseline, using *d*UHI values, shows a perfect agreement with a kappa coefficient of 1.0. All data points are accurately categorized with no commission or omission errors, highlighting an exceptionally precise classification.

     Similarly, the joint examination with *d*MNDWI as a baseline reflects substantial discrepancies in the classification, as indicated by the high overall error (64.29%) and a very low kappa coefficient of 0.016. This suggests a poor agreement beyond chance in categorizing *d*NDWI values.

The *d*SAVI analysis, using *d*NBI values as a reference, shows a moderate overall map accuracy (57.14%) with a relatively higher kappa coefficient (0.337) compared to *d*NDVI and *d*MNDWI analyses. This implies a fair level of agreement in classifying the data.

Lastly, the analysis with InSAR as a baseline for *d*TWI values shows a mixed level of accuracy. While the kappa coefficient is negative (-0.077), indicating less than chance agreement, some categories like Stability show a higher level of user accuracy (53.85%).

		Joint Examination with *d*EVI as baseline reference					
		Regeneration	Equilibrium	Degradation	Total	Commission Error (%)	Users' Accuracy
*d*NDVI values	Regrowth	1	8	7	16	93,75	6,25
	Stability	4	7	1	12	41,67	58,33
	Degradation	2	4	6	12	50,00	50,00
	Total	7	19	14	40	Overall Map Accuracy (%)	35,00
	Omission Error (%)	85,71	63,16	57,14		Overall Error (%)	65,00
	Producers Accuracy (%)	14,29	36,84	42,86		Kappa coefficient	0,048

Chart 21. Integrated Matrix of *d*NDVI and *d*EVI data as the reference standard from Landsat-8/9 data.

		Joint Examination with *d*LST as baseline reference					
		Regeneration	Equilibrium	Degradation	Total	Commission Error (%)	Users' Accuracy
*d*UHI values	Regrowth	16	0	0	16	0	100,00
	Stability	0	16	0	16	0	100,00
	Degradation	0	0	10	10	0	100,00
	Total	16	16	10		Overall Map Accuracy (%)	100,00
	Omission Error (%)	0,00	0,00	0,00		Overall Error (%)	0,00
	Producers Accuracy (%)	100,00	100,00	100,00		Kappa coefficient	1.0

Chart 22. Integrated Matrix of *d*UHI and *d*LST data as the reference standard from Landsat-8/9 data.

		Joint Examination with *d*MNDWI as baseline reference					
		Regeneration	Equilibrium	Degradation	Total	Commission Error (%)	Users' Accuracy
*d*NDWI values	Regrowth	2	4	0	6	81,82	33,33
	Stability	6	6	10	22	57,14	27,27
	Degradation	3	41	7	14	58,82	50,00
	Total	11	14	17		Overall Map Accuracy (%)	35,71
	Omission Error (%)	66,67	72,73	50,00		Overall Error (%)	64,29
	Producers Accuracy (%)	18,18	42,86	41,18		Kappa coefficient	0,016

Chart 23. Integrated Matrix of *d*NDWI and *d*MNDWI data as the reference standard from Landsat-8/9 data.

		Joint Examination with *d*SAVI as baseline reference					
		Regeneration	Equilibrium	Degradation	Total	Commission Error (%)	Users' Accuracy
*d*NBI values	Regrowth	4	4	0	8	60,00	50,00
	Stability	3	8	4	15	50,00	53,33
	Degradation	3	4	12	19	25,00	63,16
	Total	10	16	16	42	Overall Map Accuracy (%)	57,14
	Omission Error (%)	50,00	46,67	38,64		Overall Error (%)	42,86
	Producers Accuracy (%)	40,00	50,00	75,00		Kappa coefficient	0,337

Chart 24. Integrated Matrix of *d*NBI and *d*SAVI data as the reference standard from Landsat-8/9 data.

		Joint Examination with *InSAR* as baseline reference					
		Fast=3	Equilibrium	Slow=1	Total	Commission Error (%)	Users' Accuracy
dTWI values	Fast=3	4	5	1	10	81,82	22,22
	Stability	12	14	5	31	36,36	53,85
	Slow=1	1	0	0	1	100,00	0,00
	Total	17	19	6		Overall Map Accuracy (%)	42,86
	Omission Error (%)	77,78	46,15	100,00		Overall Error (%)	57,14
	Producers Accuracy (%)	18,18	63,64	0,00		Kappa coefficient	-0,077

Chart 25. Integrated Matrix of d*TWI* and InSAR data as the reference standard from Landsat-8/9 data.

1			2			3		
1	2	3	4	5	6	7	8	9
-2,045753e+15	-1,149115e+15	-7,229898e+14	-5,454376e+14	-4,122735e+14	-2,879870e+14	-1,9033333e+14	-83.802.057.470	22.729.232
-1,149115e+15	-7,229898e+14	-5,454376e+14	-4,122735e+14	-2,879870e+14	-1,903333e+14	-83.802.057.470	22.729.232	2,180366e+14

Chart 26. *C*-SAR resampling.

In*SAR*	*d*NDVI	*d*EVI	*d*SAVI	*d*NDBI	*d*MNDWI	*d*LST
1	3	3	2	4	2	5

Chart 27. InSAR rescaled values.

	In*SAR*	*d*NDVI	*d*EVI	*d*SAVI	*d*NDBI	*d*MNDWI	*d*LST	Row_sum
In*SAR*	1	1/3	1/3	1/2	1/4	1/2	1/5	3,12
*d*NDVI	3	1	1	2	4	2	5	18,00
*d*EVI	3	1	1	2	4	2	5	18,00
*d*SAVI	2	1/2	1/2	1	2	1	½	7,50
*d*NDBI	4	1/4	1/4	1/2	1	1/3	1/5	6,53
*d*MNDWI	2	1/2	1/2	1	3/2	1	1/3	6,83
*d*LST	5	1/5	1/5	2	5	3	1	16,40
Col_sum	20,00	3,78	3,78	9,00	17,75	9,83	12,23	-

Chart 28. Priorities of assigned differential values.

	Shannon	Menhinick	Brillouin	Berger-Parker	Kolmogorov-Smirnov	Row_sum	Col_sum
Row_sum	1,836	0,801	1,515	0,2357	D	*P (same distance)*	0,88275
Col_sum	1,836	0,801	1,46	0,2619	(Two-sample tests)	*P (same d. Mt Carlo)*	0,898

Chart 29. Diversity analysis employing ecological indices:
robust tests highlighting balanced differential value distribution.

	In*SAR*	*d*NDVI	*d*EVI	*d*SAVI	*d*NDBI	*d*MNDWI	*d*LST
Priority Weights	0,052	0,248	0,248	0,104	0,071	0,098	0,178

Chart 30. Prioritization of remote sensing indices.

Coeherency Index (CI)	Consistency Relationship (CR)
0,142	0,101

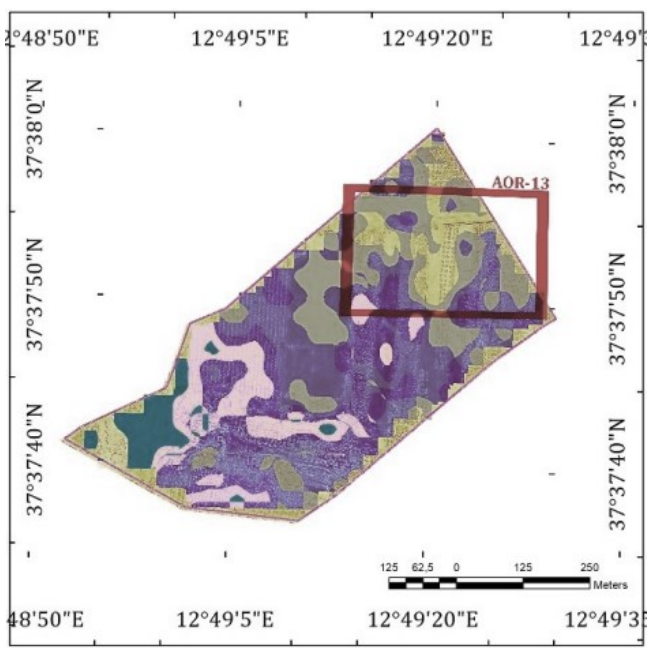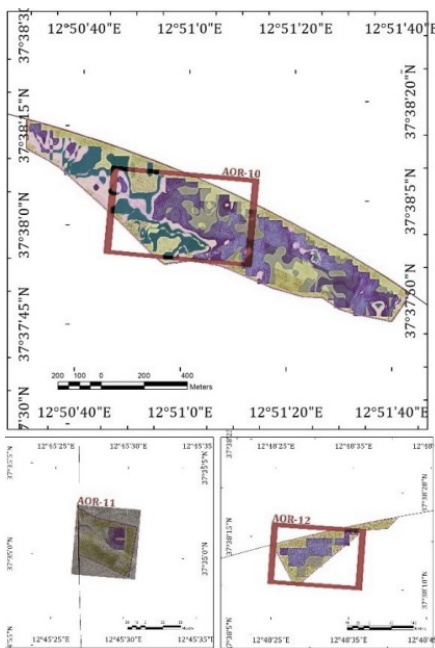**Chart 31.** Coherence in final Data analysis.

Figures 94-95-96.
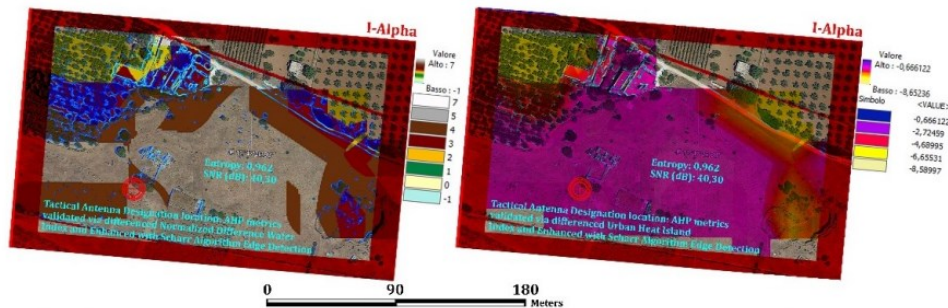Tactical Area Matrix for area designation.
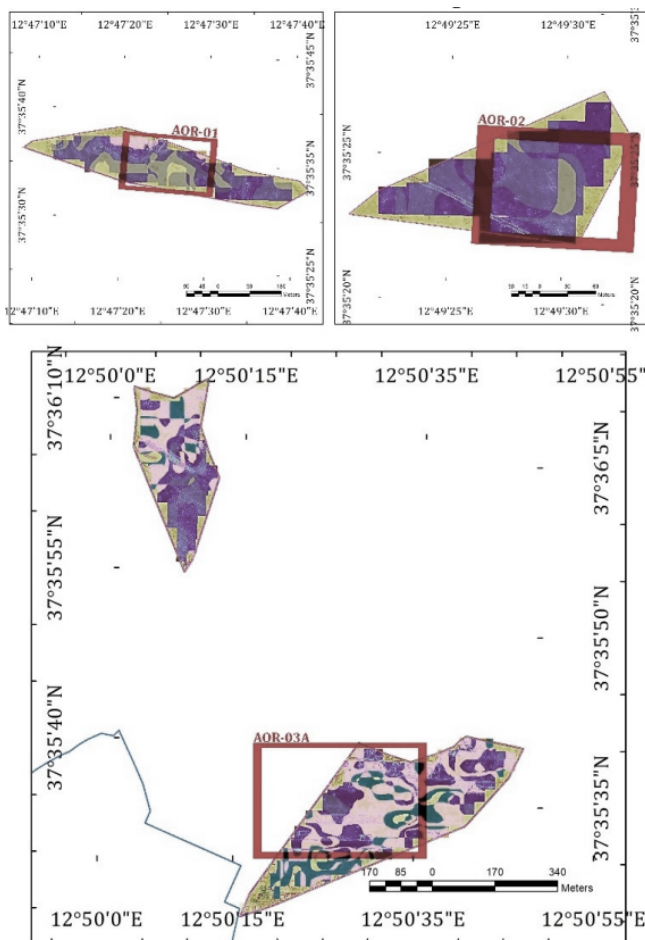
Figures 97-98-99-100-101-102.
Tactical Area Matrix for area designation.
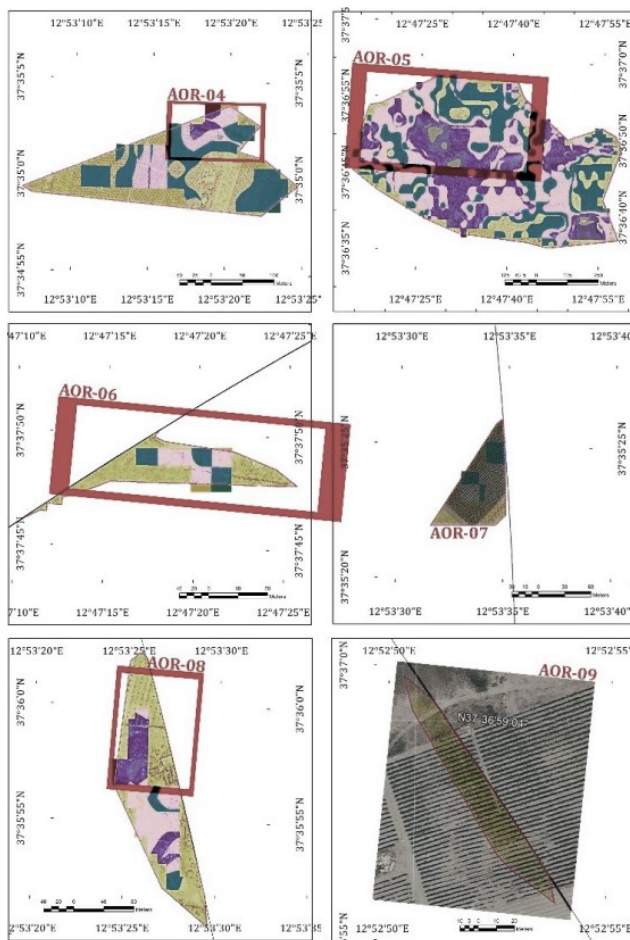
Figures 103-104-105-106 (right) .
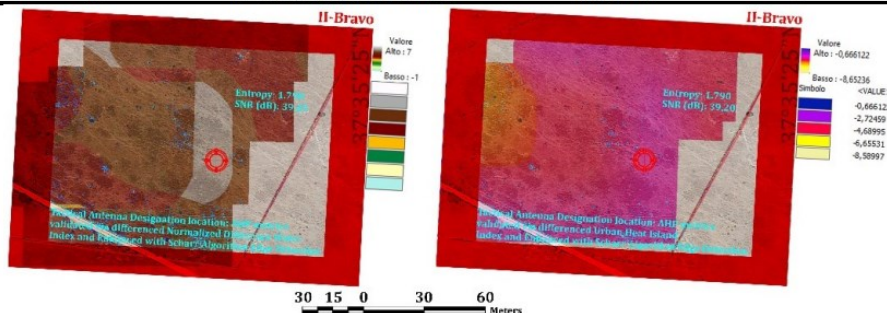Tactical Area Matrix for area designation.

Location	AOR	GPS	Weighted	dNDWI	dUHI
Alpha	01	37°35′34.35″N 12°47′25.16″E	66,000000	4	-3,738289

	Average gradient intensity		Edge orientation (x-axis)	Edges		Mean contrast (edge pixels and surrounding areas)	Density features	SNR	Edges density
Edge detection Operator	Mean	Max	3,51°	Number	Length	0,0933	135.648 units (2.61%)	0,0186 (variance 0,0023) - Factor: 8.19	72.665 pixels 0,0261 (pixel edges - sum pixels)
	0.0138	1.0155		7.231	87.464,76				
	Uniformity		Connectivity metrics			Edges coherence		Co-occurrence	Contrast variation
	Std dev	Shannon entropy	Components	Ramification		1.783 edges > 75° percentile (24,66% sum)		(GLCM)	
	0,1713	0,3937	20.723	761				0,584	35,11

Bravo	02	37°35′23,788″N 12°49′30.42″E	68,000000	5	-3,624619	

	Average gradient intensity		Edge orientation (x-axis)	Edges		Mean contrast (edge pixels and surrounding areas)	Density features	SNR	Edges density
Edge detection Operator	Mean	Max	2,55°	Number	Length	0,0754	130.065 (4,67%)	0,0155 (variance 0,0035 – Factor: 4,47)	130.065 0,0467 (pixel edges - sum edges)
	0,0215	0,9990		17,776	179.419,38				
	Uniformity		Connectivity metrics			Edges coherence		Co-occurrence	Contrast variation
	Std dev	Shannon entropy	Components	Ramification		4.295 edges > 75° percentile (24,16%)		(GLCM)	
	0,1515	0,5588	45.609	1.360				0,626	58,41

Charlie	03	37°35′34.73″N 12°50′27.50″E	57,000000	4	-4,614380	

	Average gradient intensity		Edge orientation (x-axis)	Edges		Mean contrast (edge pixels and surrounding areas)	Density features	SNR	Edges density
Edge detection Operator	Mean	Max	-1,55°	Number	Length	0,1816	52.654 (5.90%)	0.0604 (variance 0.0112 – Factor: 5.39)	52.654 0.0590 (pixel edges - sum edges)
	0.0562	1.0356		2.313	73.079,44				
	Uniformity		Connectivity metrics			Edges coherence		Co-occurrence	Contrast variation
	Std dev	Shannon entropy	Components	Ramification		559 edges > 75° percentile (24.17%)		(GLCM)	
	0.229	0.323	12.785	737				172,09	0,641

Delta	04	37°35'03,19"N 12°53'18,79"E	61,000000	3	-4,480659

Edge detection Operator	Average gradient intensity		Edge orientation (x-axis)	Edges		Mean contrast (edge pixels and surrounding areas)	Density features	SNR	Edges density
	Mean	Max		Number	Length			156,57 (Mean Signal) variance 8.807,18 – Factor: 1,67	2.875 0,103 (pixel edges - sum edges)
	163,51	4.424,01	160,40°	236	498,88	1.479,31	2.783.232 (0,00848)		
	Uniformity		Connectivity metrics			Edges coherence	Co-occurrence		Contrast variation
	Std dev	Shannon entropy	Components	Ramification		3.955,32 > 75° percentile (25,05%)	(GLCM)		
	93,85	2,25	236	2,06			0,578		112,344

Echo	05	37°36'53,42"N 12°47'32,03"E	72,000000	5	-2,680717

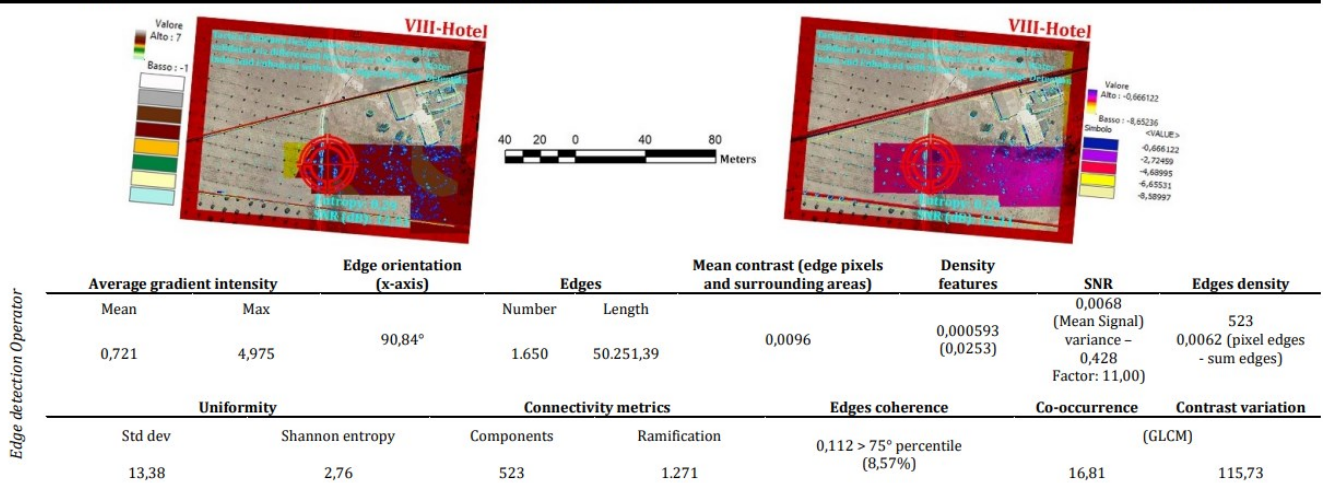| Edge detection Operator	Average gradient intensity		Edge orientation (x-axis)	Edges		Mean contrast (edge pixels and surrounding areas)	Density features	SNR	Edges density
	Mean	Max		Number	Length			0,579 (Mean Signal) variance 0,206 – Factor: 4,95	377.709 0,1357 (pixel edges - sum edges)
	0,0609	1,137	0°	32.371	125.267,68	0,1179	377.709 (13,57%)		
	Uniformity		Connectivity metrics			Edges coherence	Co-occurrence		Contrast variation
	Std dev	Shannon entropy	Components	Ramification		0,809 > 75° percentile (25,00%)	(GLCM)		
	0,454	3,516	8,263	16.015			0,583		616,10

Foxtrot	06	37°37'49,34"N 12°47'19,05"E	48,000000	2	N/A

Edge detection Operator	Average gradient intensity		Edge orientation (x-axis)	Edges		Mean contrast (edge pixels and surrounding areas)	Density features	SNR	Edges density
	Mean	Max		Number	Length			0,9142 (Mean Signal) variance 0,0718 – Factor: 4,36	1.266.584 0,455 (pixel edges - sum edges)
	0,0121	1,1334	-0,25°	77	23.339,96	0,1438	377.709 (1,75%)		
	Uniformity		Connectivity metrics			Edges coherence	Co-occurrence		Contrast variation
	Std dev	Shannon entropy	Components	Ramification		0,806 > 75° percentile (25,00%)	(GLCM)		
	0,2834	1,0005	1,685	1,858			0,992		132,98

Golf	07	37°35'23,10"N 12°53'33,85"E	N/A	N/A	-7,559898

Edge detection Operator	Average gradient intensity		Edge orientation (x-axis)	Edges		Mean contrast (edge pixels and surrounding areas)	Density features	SNR	Edges density
	Mean	Max		Number	Length			0,8543 (Mean Signal) variance 0,1113 – Factor: 4,77)	200.494
	0,0318	1,1366	-3,83°	1.623	56.054,48	0,174	0,01745 (0,2043)		0,072 (pixel edges - sum edges)
	Uniformity		Connectivity metrics			Edges coherence		Co-occurrence	Contrast variation
	Std dev	Shannon entropy	Components	Ramification		2.356 > 75° percentile (27,04%)		(GLCM)	
	87.925	1,808	430	0				0,9783	333,65

Hotel	08	37°35'58,89"N 12°53'26,15"E	58,000000	3	-4,573219

Edge detection Operator	Average gradient intensity		Edge orientation (x-axis)	Edges		Mean contrast (edge pixels and surrounding areas)	Density features	SNR	Edges density
	Mean	Max		Number	Length			0,0068 (Mean Signal) variance – 0,428 Factor: 11,00)	523
	0,721	4,975	90,84°	1.650	50.251,39	0,0096	0,000593 (0,0253)		0,0062 (pixel edges - sum edges)
	Uniformity		Connectivity metrics			Edges coherence		Co-occurrence	Contrast variation
	Std dev	Shannon entropy	Components	Ramification		0,112 > 75° percentile (8,57%)		(GLCM)	
	13,38	2,76	523	1.271				16,81	115,73

India	09	37°36'58,94"N 12°52'51,31"E	N/A	N/A	N/A

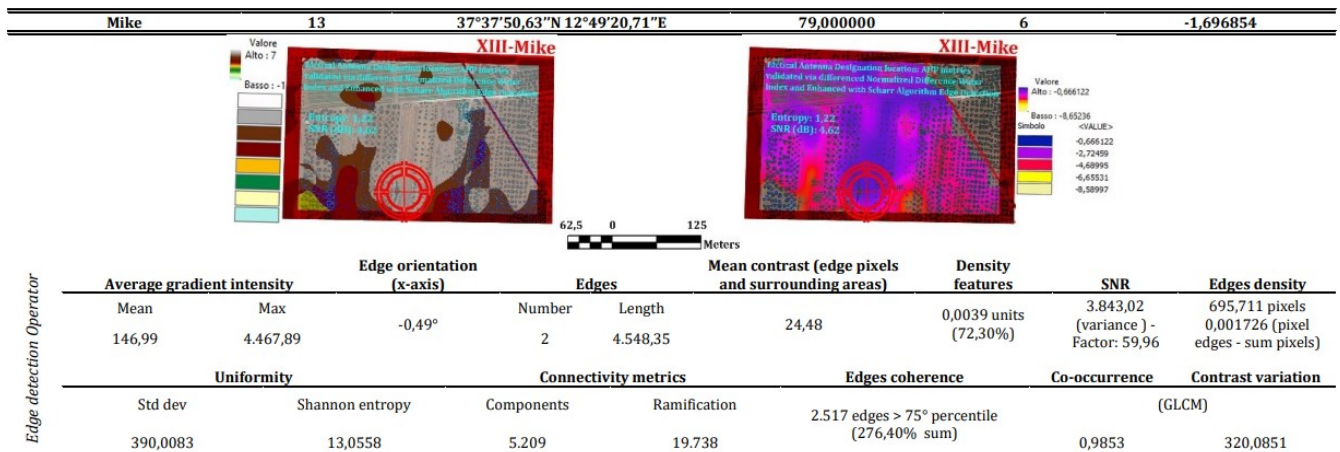
Edge detection Operator	Average gradient intensity		Edge orientation (x-axis)	Edges		Mean contrast (edge pixels and surrounding areas)	Density features	SNR	Edges density
	Mean	Max		Number	Length			0,00235 variance 0,808 - Factor: 14,65	125,176 pixels
	40,28	245,89	-0,34°	1.248	56.500,91	0,0077	21.476,97 (0,045)		0,044975 (pixel edges - sum pixels)
	Uniformity		Connectivity metrics			Edges coherence		Co-occurrence	Contrast variation
	Std dev	Shannon entropy	Components	Ramification		21.476,97 > 75° percentile (0,00 % sum)		(GLCM)	
	0,228	0,802	1.113	36.655				0,9995	0,00097

Juliett	10	37°37'58,98"N 12°51'07,04"E	-1,651711	4	-1,651711

Edge detection Operator	Average gradient intensity		Edge orientation (x-axis)	Edges		Mean contrast (edge pixels and surrounding areas)	Density features	SNR	Edges density
	Mean	Max	5,73°	Number	Length	0,0733	135.648 units (4.87%)	0,0155 (variance 0,0053) - Factor: 2,90	135,648 pixels 0,0487 (pixel edges - sum pixels)
	0,0273	1,028		21,500	111.304,59				
	Uniformity		Connectivity metrics			Edges coherence		Co-occurrence	Contrast variation
	Std dev	Shannon entropy	Components	Ramification		5.203 edges > 75° percentile (24,2% sum)		(GLCM)	
	0,128	2,037	45.405	56				0,552	48,78

Kilo	11	37°35'00,04"N 12°45'28,43"E	84,000000	N/A	-1,736488

Edge detection Operator	Average gradient intensity		Edge orientation (x-axis)	Edges		Mean contrast (edge pixels and surrounding areas)	Density features	SNR	Edges density
	Mean	Max	5,73°	Number	Length	34,52	0,95 units (94,96%)	0,124 (variance 1.081,20) - Factor: 1,84	55.634 pixels 0,00071 (pixel edges - sum pixels)
	44,01	10.345,03		476	55.634				
	Uniformity		Connectivity metrics			Edges coherence		Co-occurrence	Contrast variation
	Std dev	Shannon entropy	Components	Ramification		0,886 edges > 75° percentile (34,02% sum)		1,00	32,92
	37,14	0,37	1.789	1,65					

Lima	12	37°38'15,26"N 12°48'29,47"E	73,000000	5	-2,705910
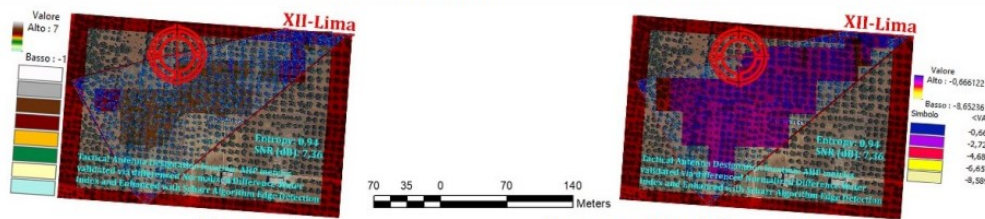
Edge detection Operator	Average gradient intensity		Edge orientation (x-axis)	Edges		Mean contrast (edge pixels and surrounding areas)	Density features	SNR	Edges density
	Mean	Max	0,139°	Number	Length	118,90	0,0136 units (1,362%)	2.401 (variance 1,0) - Factor: 9,28	0,0136 pixels 0,0547 (pixel edges - sum pixels)
	390,50	11.818,29		37.910	152.347				
	Uniformity		Connectivity metrics			Edges coherence		Co-occurrence	Contrast variation
	Std dev	Shannon entropy	Components	Ramification		13.822 edges > 75° percentile (0,0072% sum)		(GLCM)	
	0,0886	2,1385	13.822	0,098				0,8016	347,86

Mike	13	37°37'50,63"N 12°49'20,71"E	79,000000	6	-1,696854

62,5   0   125 Meters

Edge detection Operator

	Average gradient intensity		Edge orientation (x-axis)	Edges		Mean contrast (edge pixels and surrounding areas)	Density features	SNR	Edges density
	Mean	Max		Number	Length				
	146,99	4.467,89	-0,49°	2	4.548,35	24,48	0,0039 units (72,30%)	3.843,02 (variance) - Factor: 59,96	695,711 pixels 0,001726 (pixel edges - sum pixels)
	Uniformity		Connectivity metrics		Edges coherence		Co-occurrence	Contrast variation
	Std dev	Shannon entropy	Components	Ramification			(GLCM)	
	390,0083	13,0558	5.209	19.738	2.517 edges > 75° percentile (276,40% sum)		0,9853	320,0851

The Gray-Level Co-occurrence Matrix (GLCM) is a fundamental tool in remote sensing, initially developed for image analysis (Haralick, Robert M. et al., 1973) for texture feature extraction, $P(i,j)$, examining the frequency of pixel intensity pairs , i and j, at specified distances d and orientations θ; by providing essential metrics such as contrast, $C = \sum_{i,j}(i - j)^2 P(i,j)$, correlation for the mean, μ, standard deviation σ, energy (angular second moment) with higher values indicating more homogeneous textures (particularly appreciated in this evaluation due to its detection of pixel pairing), and homogeneity (for smoother textures with less variation between neighbouring pixel intensities), which characterize spatial relationships and texture patterns, each element has been and converted into a theoretical model addressed to Signal to Noise Ratio propagation.

These metrics are crucial for evaluating connectivity, edge coherence, and co-occurrence, contributing to a detailed understanding of spatial structures. Connectivity metrics gauge the degree of regional contiguity, while edge coherence measures the consistency of edge directions, with GLCM features like correlation and homogeneity offering insights into these aspects.

Co-occurrence is directly represented by the GLCM, revealing texture patterns and spatial relationships. Contrast variation, indicating intensity differences, and the Signal-to-Noise Ratio (SNR), inferred through the energy feature, are essential for assessing image quality and detail.

The mean signal variance is elucidated by GLCM contrast and correlation, indicating pixel intensity variability. Edge density, reflecting the number of edges in an area, and density features, describing pixel intensity compactness, are inferred from GLCM's contrast and homogeneity metrics.

Mean contrast between edge pixels and surrounding areas is directly related to the GLCM contrast feature. Additionally, edges, marked by significant intensity changes, are highlighted by GLCM's contrast and energy, while edge orientation and average gradient intensity, though not directly measured by GLCM, are supported through detailed texture analysis; in the context of rapid detection of hotspots in orthophotos (Zhao, Jinling et al., 2021), the proposed research similarly applied a corresponding division of 50 x 50 meter cells (Klemmt, H. et al., 2020) for analysis.

Utilizing datasets from InSAR and Landsat over brief temporal intervals enhanced the detection of ground deformation, structural changes, merging pertinent spatial and spectral variations (Zhao, J. et al., 2021), except from important number of training samples, making these features invaluable for critical applications, particularly for site designation to place antennas; the appreciation of such fine-tuned integration aids in identifying optimal antenna placement sites by ensuring stable, interference-free locations.

3.5. Decibel mapping from cosine angles and adversarial Λ Path Loss augmentation

In the realm of Electronic Warfare for Heritage Park defense, the strategic application of mathematical formulas creates a formidable electronic defense system; this conceptualized system begins with the Path Loss Equation, $L = L_0 + 10\,n \log_{10}(d) + X$, which is fundamental for determining signal strength and range within the park. Here, L_0 denotes the initial path loss, n the path loss exponent indicating environmental impact, d the signal travel distance, and X encompasses additional losses. Understanding this attenuation is crucial for optimizing a respectful placement and physical effectiveness of surveillance equipment.

The geometric Law of Cosines, $c^2 = a^2 + b^2 - 2\,a\,b\,cos(\gamma)$, was considered as a critical role in the triangulation process, essential for pinpointing the origins of potential electronic threats. In this formula, a, b, and c represent the sides of a triangle, and γ the angle between them, forming the basis for spatial analysis in signal tracking.

For signal analysis and differentiation, the Cosine Similarity formula (Sidorov G. et al., 2014) whereby Cosine Similarity $(A, B) = (A \cdot B) / (||A||\,||B||) = (\Sigma\,A_i^2\,\Sigma\,B_i^2) / \Sigma\,A_iB_i$ from i=1 to n, is instrumental; this equation, by measuring the cosine of the angle between two signal vectors A and B, aids in classifying signals, effectively distinguishing between those that are benign and potentially malicious.

$$\text{PathlossTotal}\,(dB) = \text{FSPL}\,(dB) + \Lambda_{\text{shadow}} + \Lambda_{\text{aspect}} + \Lambda_{\text{hillshade}} + \Lambda_{\text{spectral}} + \Lambda_{\text{Fresnel}}$$
$$\Lambda_{\text{environmental}} + 10\log_{10}\left(\sin(C)\sqrt{AB}\right)$$

Equation 7. Total Path Loss: whereby specialized factor tailored for specific conditions or system characteristics are attributed case depending. The logarithmic function suggests a decibel scale, and the inclusion of a sine function and a square root term ($\sqrt{AB}$) indicates a trigonometric and possibly geometric component.

Eq. 7 integrates multiple factors affecting signal propagation; Free Space Path Loss (FSPL), environmental elements like terrain shadowing, aspect, and hillshade effects, along with spectral characteristics, all objects of Atmospheric Electromagnetic Interference (EMI) and Fresnel zone impacts (catch-all for any additional losses that are not explicitly covered by the other coefficients).

The target designation has necessitated triangulating a network, encompassing signal behavior under various conditions, which is key to maintaining robust communication and surveillance systems in Heritage Park and beyond its borders.
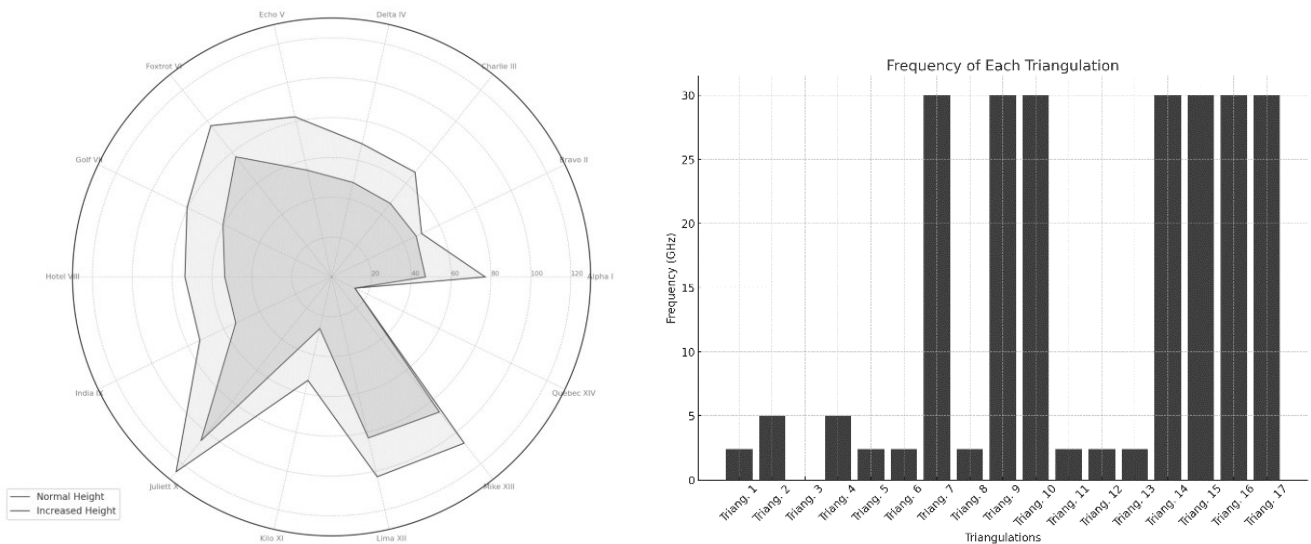
Fig. 107. EW Shield: Antenna heights mapping for target designations [meters]. [FSPL (dB), Λ shadow, Λ aspect, Λ hillshade, Λ spectral, Λ Fresnel, Λ environmental and $10\log10(\chi)$]. **Fig. 108.** EW Shield: Antenna frequency mapping for target designations [$\phi_{\text{FSPL}}(dB)$, Λ shadow, Λ aspect, Λ hillshade, Λ spectral, Λ Fresnel, Λ environmental and $10\log10(\chi)$].

3.5.1. Electronic Atmospheric Target Designation (EATD) : Λ degradation rescaling

Equations 4-5-7 are recognized at enhancing the following antennas triangulations targets for Electronic Atmospheric Target Designation as also proven as sites designation' decibels detailed in FSPL.
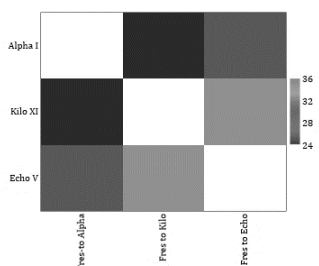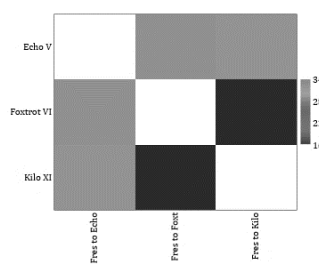

Fig. 109. EATD sub-category I.
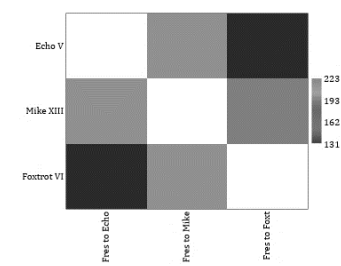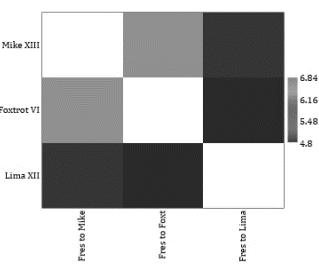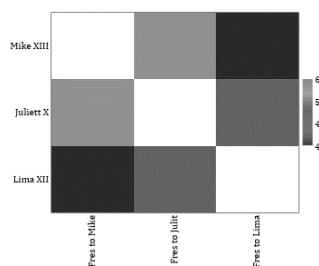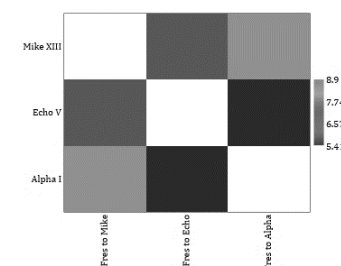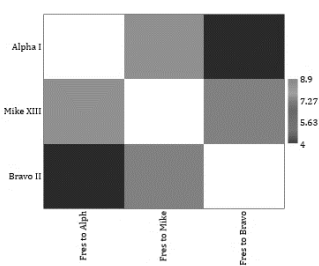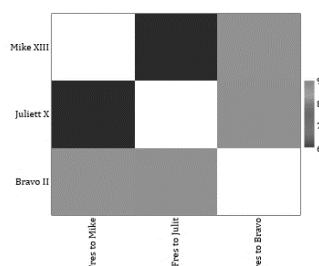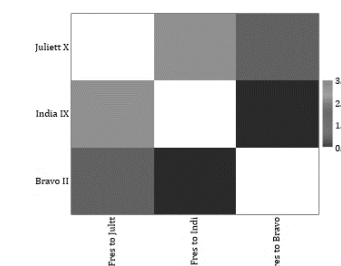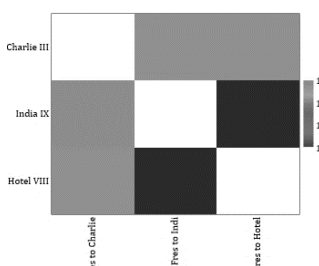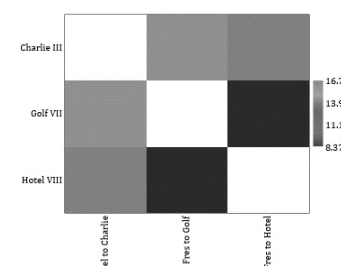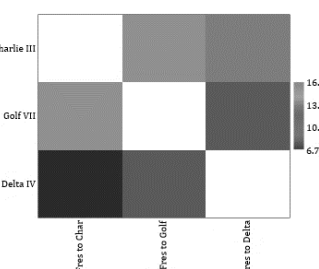

Fig. 110. EATD sub-category II.

Fig. 111. EATD sub-category III.

Fig. 112. EATD sub-category IV.

Fig. 113. EATD sub-category V.

Fig. 114. EATD sub-category VI.

Fig. 115. EATD sub-category VII.

Fig. 116. EATD sub-category VIII.

Fig. 117. EATD sub-category IX.
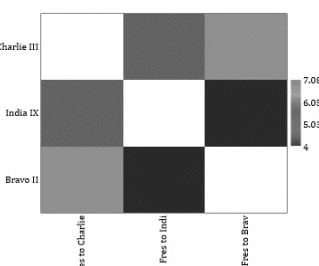
Fig. 118. EATD sub-category X.

Fig. 119. EATD sub-category XI.

Fig. 120. EATD sub-category XII.

Fig. 121. EATD sub-category XIII.
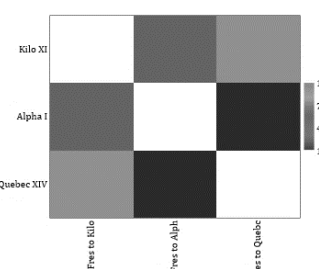
Fig. 122. EATD sub-category XIV.
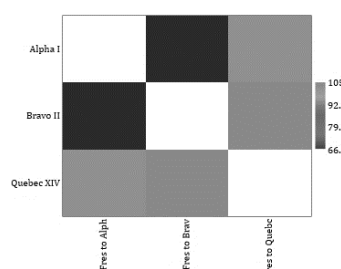
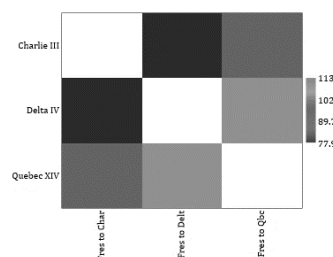**Fig. 123.** EATD sub-category XV.
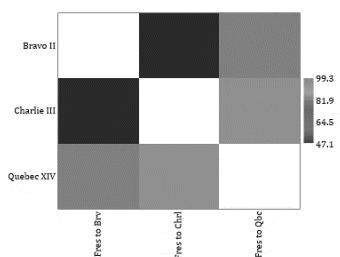
Fig. 124. EATD sub-category XVI.

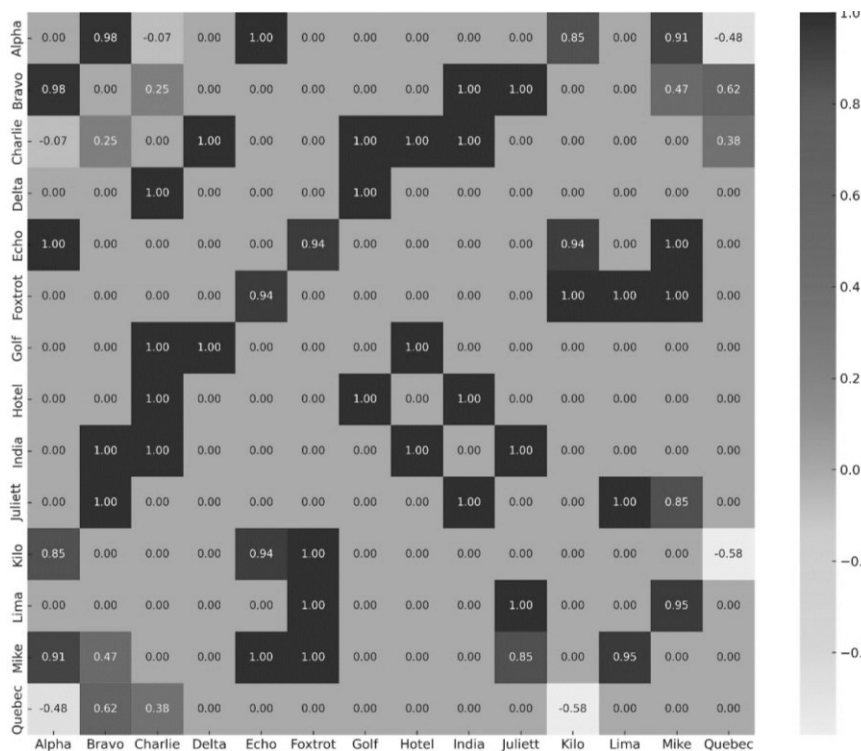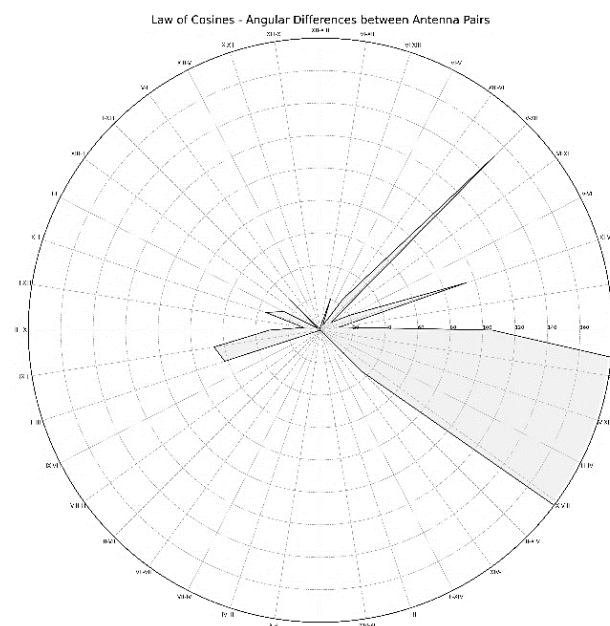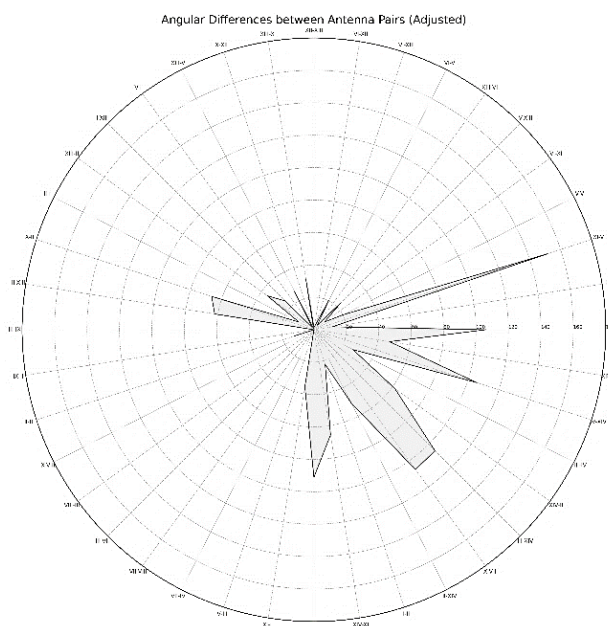**Fig. 125.** EATD sub-category XVII.

Fig. 126. Fresnel *dB* levels heat map. **Figures. 127-128.** Error minimization: target location in 3D space to improve accuracy in non-ideal conditions.
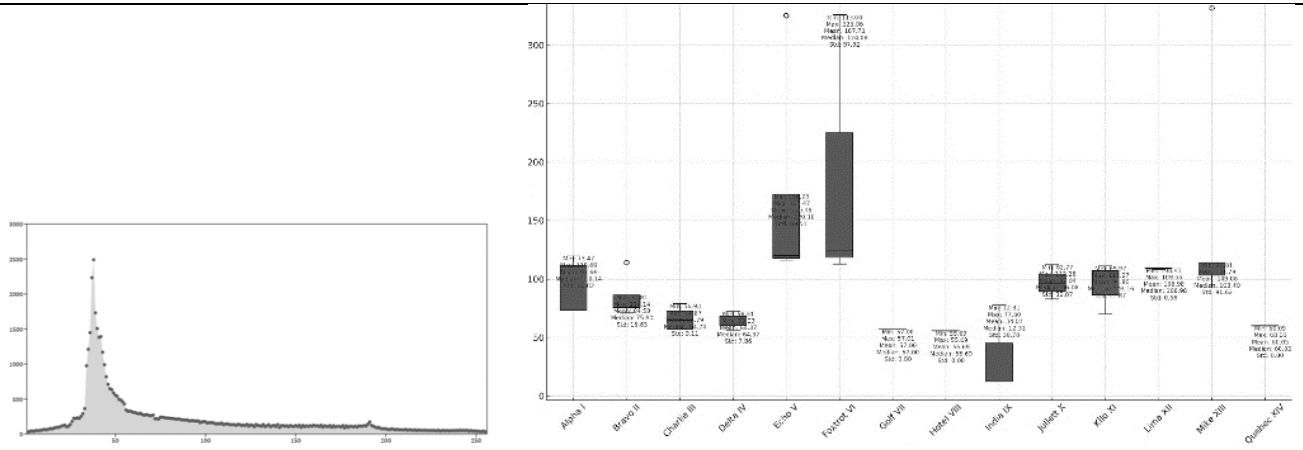
Fig. 129. Path Loss graphical benchmark.

Fig. 130. GHz station antenna power of maximizing power efficiency: Foxtrot-India P_T-P_R prospects.
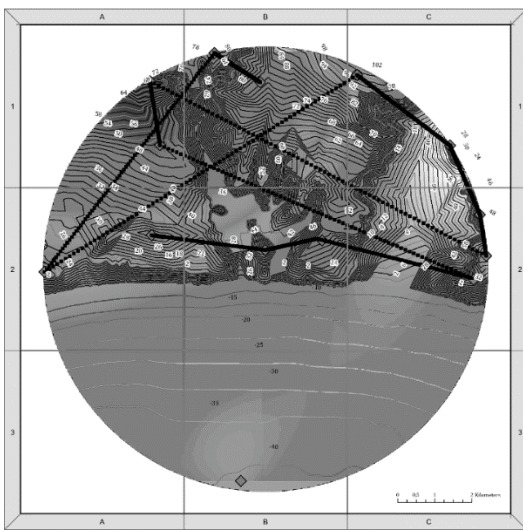

Fig. 131. ν transmission: across stations (ε)-(ρ, σ). **Fig. 132.** Aircraft trajectory. The analysis of flight data over the archaeological park of Selinunte has yielded significant findings, as evidenced by the statistical tests conducted on the collected data. The Kruskal-Wallis test, as a non-parametric method for assessing the differences between group medians, yielded a chi-square value of 2423, with a tie-corrected value of 2426, leading to a *p*-value of essentially zero. This indicates a statistically significant distinction between the group medians, suggesting variable flight characteristics or environmental conditions during the survey operations.
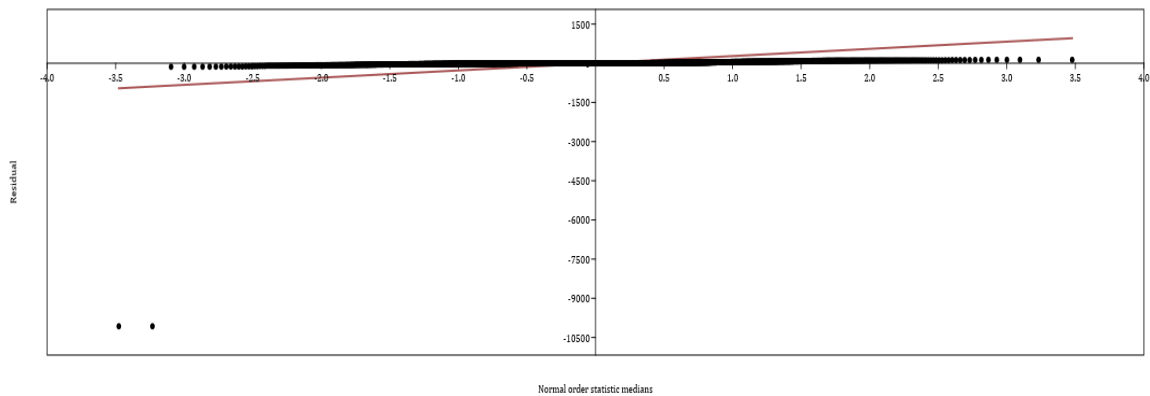

Fig. 133. The Bayes factor, exceeding 10^{11}, offers decisive evidence supporting the presence of unequal means among the surveyed flights. The synthesis of these statistical insights paints a complex portrait of the operational dynamics during the flights over Selinunte, highlighting the influence of various factors on the collected data. Such

disparities in flight data are crucial for the interpretation of aerial surveys, as they affect the accuracy and reliability of archaeological findings.
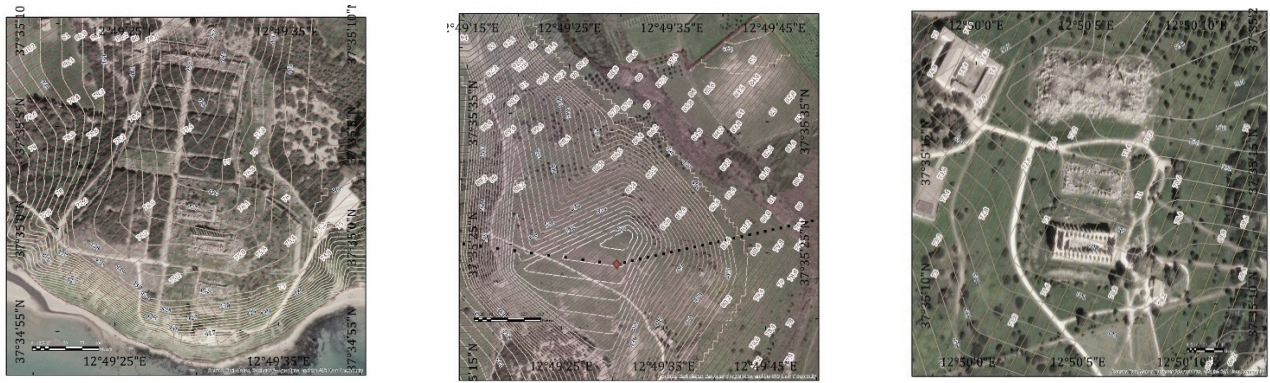

Fig. 134. Electronic signatures strategy. *Acropolis* (Temples: A-B-C-D-O-*Polluce* Tower). **Fig. 135.** Tower *Manuzza-Necropolis*. **Fig. 136.** Eastern side (Temples E-F-G-*Antiquarium*).
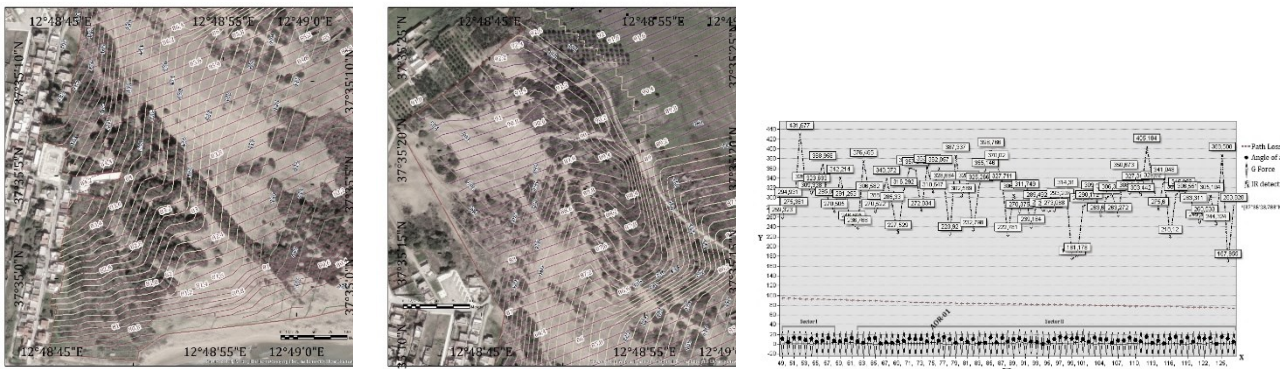

Fig. 137. Western side (*Malophoros* temple). **Fig. 138.** *Antiquarium*.
Fig. 139. Retrieved Data Fusion analysis : sampling avionics from the initial test.

4. Discussion : replicability from the lesson of Paul Virilio for future orientations

In the complex interplay of Vitruvian principles and Paul Virilio's dromological theory, the efforts of *Ordine Architetti Napoli* are poised to refine advanced methodologies addressing emerging challenges in the preservation of heritage sites (ICOMOS, 1964, 1990, 2021) across the Mediterranean area (Kathem, M. et al., 2020): this initiative places a specific focus on the role of Electronic Warfare (EW) in safeguarding historical and archaeological sites, envisioning the transformation of the built environment into a bastion of Signal Intelligence (SIGINT) and agility.

These pursuits underscore a sophisticated matrix that transcends a mere functional view of technology in the realm of EW; instead, technology is acknowledged as a critical component, imbued with political, aesthetic, and practical significance. This perspective aligns with the views of thinkers like Paul Virilio, who highlighted the intrusive nature of technology as a political and military expression (Schofield John, 2009), far from being neutral (Chudoba E., 2017). Similarly, the work of Prof. Leonardo Di Mauro, monitoring the presence of state architecture as a continuous legacy in context of volatile information, e.g. servers and sensors in Heritage sites, aligns with newer paradigms of industrial archaeology and military architecture (Knauer, Birgit. (2023), including decommissioned radio systems.

The interpretation of protection, both in times of war (Legnér M., 2022) and peace (Krauss, J., n.d.), acknowledges the omnipresence, versatility, and scalability of EW. This is a continuous objective for the professional order, aiming to provide a vision for its members and the broader Italian architectural community. The research will emphasize the need to stay attuned to rapid changes, reflecting the narrative that is always open and in step with social (Murphy D., 2001), cultural (Manacorda S. and Visconti A., 2013), geopolitical (Margottini C. 2014), and technological dynamics.

This approach by Ordine Architetti Napoli exemplifies a proactive stance in integrating modern warfare technology and architectural preservation: the importance of evolving the role of architects and preserving professionals in responding to the challenges posed by modern technologies. By aligning with the dynamic principles of Vitruvian architecture and Virilio's theory, the Order not only contributes to the physical preservation (Langfield

Michele, Logan William and Craith Nic Máiréad, 2010) of heritage sites but also engages in a broader discourse on their role and significance in a rapidly changing domain.

5. Conclusion: evidence of EW compatibility from this initial series of fine-tuned evaluations

The elucidation of the data, quintessentially entrenched within the Electronic Warfare (EW) paradigm, highlights critical deficits in regional interception capabilities of low-altitude Unmanned Aerial Vehicles (UAVs) or flights surveilling the Selinunte archaeological expanse, for which we plan future orientations.

EW, characterized by its dynamic state of fluxional advancement, manifests outcomes corroborated by Bayesian inferential statistics: the Bayes factor, exponentially surpassing 10^{11}, furnishes empirical substantiation for the hypothesis postulating non-uniform mean vectors ($\vec{\mu}$) in the scrutinized flight vector field ($\vec{F}$).

This statistical amalgamation, through a matrix ($\vec{M}$) of complex data points, renders the operational dynamics over Selinunte, thereby accentuating the multifarious influences on the aerial data matrix ($\vec{D}$). Perturbations in flight data matrices are fundamental for aerial reconnaissance interpretation, thereby influencing the integrity and precision of archaeological deductions.

In the analytical domain, the profound scrutiny of Selinunte's aerial data employs the Kruskal-Wallis test, a robust non-parametric method, to discern variations among group median vectors ($\overrightarrow{Mg}$). This yields a chi-square (χ^2) statistic of 2423, adjusted to 2426 considering ties, converging towards a p-value near infinitesimal limits. This statistically significant heterogeneity among the median vectors suggests variabilities in flight characteristic matrices ($\overrightarrow{Cf}$) or ambient condition matrices ($\overrightarrow{Ca}$) during surveillance operations.

The antenna's detection within Selinunte's heritage compass is expressed via coordinates and signal strength matrices: Bravo 02 37°35'23.788"N 12°49'30.42"E, matrix element [68,000000, 5, -3.624619].

Acknowledgments

Conflict of Interests

The author declares no conflict of interest. The numerical conclusions, as well as their numerical processing, have not accountability in the role, design, collection, or interpretation of data but aims at demonstrating adequate and fine-tuned methodologies in favour of "*Valutazione Impatto Ambientale*" (VIA) (Environmental Impact Assessment (EIA), "*Valutazione Impatto Strategica*" (VAS) (Strategic Environmental Assessment, SEA), that are derived from three branches in the process of Training and Internationalization c/o the *Ordine degli Architetti Pianificatori Paesaggisti Conservatori di Napoli e Provincia*: architecture of landscape, engineering for the territory and agronomy whose international commitment was inaugurated by former President Arch. Raffaele Sirica (1995-1997) in occasion of the Habitat II program by the second United Nations Conference on Human Settlements, taken place from June 3 to 14, 1996, in Istanbul, Turkey. The Department does not promote any misconduct, e.g., 95/46/EC and Regulation (EC) No 45/2001 (EC) No 45/2001, by endorsing: the reintroduction of historical components ecologically suitable, a sustainable land use perspective and data extraction techniques without animal experimentation and environmental invasive footprint in accordance with the rigorous Italian legislation for the landscape. No research institution, e.g., university teaching, has ever been involved in the research.

Data availability statement

The data that support the findings of this study are available on request from the lead researcher, Ing. Arch. Salvatore Polverino, at formazione@napoli.archiworld.it. Access to the data will be granted upon request and approval by the Institutional Review Board c/o *Ordine Architetti Napoli PPC* and will be subject to a data sharing agreement that ensures the confidentiality and anonymity of the participants. Requests for access to the data will be considered on a case-by-case basis and will require a clear explanation of the intended use and analysis of the data.

Ethics statements

This study was conducted in accordance with the principles of the European code of ethics for scientific research ruled by the Declaration of Helsinki (2013) and was approved by the Institutional Review Board. Participants were informed of their right to withdraw from the study at any time without penalty. The research ensured no harm or risk to participants, and all gathered data were exclusively utilized for understanding the built environment in relation to Military and Heritage Architecture from the past. All data provided are rigorously unclassified and released into the public domain without any copyright infringement. Any questions or concerns regarding the study can be directed to the lead researcher at: *Ordine Architetti PPC Napoli*, Department Training and Internationalization, Piazzetta Matilde Serao 7, 80132, Napoli, Italy, or formazione@napoli.archiworld.it. We express appreciativeness to Prof. Arch. Ahmad Nia in the guise of external expert and representative for the Mediterranean area on behalf of *Ordine Architetti Napoli PPC*.

Credit author statement

The author, Ing. Arch. Salvatore Polverino, confirms unique contributions to his corresponding membership from the *Ordine Architetti Napoli PPC* affiliation while collaborating within the Training Department; specifically: Prof. Leonardo Di Mauro, who provided invaluable insights into the historical dimensions, e.g. focusing on Military Archaeology in this special issue, and its implications on Landscape interpretation and President Prof. Arch. Lorenzo Capobianco who confirmed the research scope and governmental bodies data orientation, following the path indicated by Presidents Raffaele Sirica and (honorary) Paolo Pisciotta. Secretary Ing. Arch. Salvatore Polverino directed in the quality of sole author, the entire research.

References

Barakat, Sultan. (2021). «Necessary Conditions for Integrated Approaches to the Post-Conflict Recovery of Cultural Heritage in the Arab World». *International Journal of Heritage Studies* 27, n. 5: 433–48. https://doi.org/10.1080/13527258.2020.1799061.

Belal, A., e E. Shcherbina. (2019). «Heritage in Post-War Period Challenges and Solutions». *IFAC-PapersOnLine* 52, n. 25: 252–57. https://doi.org/10.1016/j.ifacol.2019.12.491.

Beven, K. J., e M. J. Kirkby. (1979). «A Physically Based, Variable Contributing Area Model of Basin Hydrology / Un Modèle à Base Physique de Zone d'appel Variable de l'hydrologie Du Bassin Versant». *Hydrological Sciences Bulletin* 24, fasc. 1: 43–69. https://doi.org/10.1080/02626667909491834.

Bronshtein, I.N., K.A. Semendyayev, Gerhard Musiol, e Heiner Mühlig. (2015). *Handbook of Mathematics*. Berlin, Heidelberg: Springer Berlin Heidelberg. https://doi.org/10.1007/978-3-662-46221-8.

Brosché, Johan & Legnér, Mattias & Kreutz, Joakim & Ijla, Akram. (2016). Heritage under attack: motives for targeting cultural property during armed conflict. International Journal of Heritage Studies. 23. 1-13. 10.1080/13527258.2016.1261918.

Carrier, Jill, and Mark Aronoff. (1979). «Word Formation in Generative Grammar». *Language* 55, fasc. 2: 415. https://doi.org/10.2307/412595.

Cheng-Zhi Qin Tao, Zhu A-Xing, Yang Lin, Luo Ming, Li Baolin, e Zhou Chenghu. (2010). «Mapping Soil Organic Matter Using the Topographic Wetness Index: A Comparative Study Based on Different Flow-Direction Algorithms and Kriging Methods». *Ecological Indicators* 10, fasc. 3: 610–19. https://doi.org/10.1016/j.ecolind.2009.10.005.

Chudoba, Ewa. (2017). «What Controls and What is Controlled?: Deweyan Aesthetic Experience and Shusterman's Somatic Experience». *Contemporary Pragmatism* 14, fasc. 1 : 76–92. https://doi.org/10.1163/18758185-01401005.

Craith, Máiréad Nic. (2008). «Intangible Cultural Heritages». *Anthropological Journal of European Cultures* 17, fasc. 1: 54–73. https://doi.org/10.3167/ajec.2008.01701004.

Crooke, Elizabeth, e Tom Maguire. (2018). a c. di. *Heritage after Conflict: Northern Ireland*. 1ª ed. Routledge. https://doi.org/10.4324/9781351164320.

Cunliffe, E. (2020). No Strike Lists – From Use to Abuse? *Heritageinwar*. [PDF]. Retrieved from document URL: https://www.heritageinwar.com/single-post/2020/01/24/trump-and-iranian-cultural-property-heritage-destruction-war-crimes-and-the-implications. (Accessed: September 2023).

Falconer, Kenneth. (2003). *Fractal Geometry: Mathematical Foundations and Applications*. 1ª ed. Wiley. https://doi.org/10.1002/0470013850.

Freedberg, Sydney. (2012). "Will Stealth Survive as Sensors Improve? F-35, Jammers at Stake," Aol Defense. http://defense.aol.com/2012/11/27/will-stealth-survive-assensors-improve-f-35-jammers-at-stake/ (accessed March 6, 2013).

Fuqin Li et al. (2004). «Deriving Land Surface Temperature from Landsat 5 and 7 during SMEX02/SMACEX». *Remote Sensing of Environment* 92, fasc. 4: 521–34. https://doi.org/10.1016/j.rse.2004.02.018.

Giammusso, Federico Maria. (2012). «Surveying, analysis and 3D modeling in archaeological virtual reconstruction: The inner colonnade of the naos of Temple G of Selinunte». In *2012 18th International Conference on Virtual Systems and Multimedia*, 57–64. Milan, Italy: IEEE. https://doi.org/10.1109/VSMM.2012.6365907.

Gonzalez, Rafael C., Richard E. Woods, e Barry R. Masters. (2009). «Digital Image Processing, Third Edition». *Journal of Biomedical Optics* 14, fasc. 2 : 029901. https://doi.org/10.1117/1.3115362.

Guidoboni, E. (2002). «A Case Study in Archaeoseismology. The Collapses of the Selinunte Temples (Southwestern Sicily): Two Earthquakes Identified». *Bulletin of the Seismological Society of America* 92, fasc. 8 : 2961–82. https://doi.org/10.1785/0120010286.

Haralick, Robert M., K. Shanmugam, e Its'Hak Dinstein. (1973). «Textural Features for Image Classification». *IEEE Transactions on Systems, Man, and Cybernetics* SMC-3, fasc. 6 : 610–21. https://doi.org/10.1109/TSMC.1973.4309314.

Hu, J., Z.W. Li, X.L. Ding, J.J. Zhu, L. Zhang, e Q. Sun. (2014). «Resolving Three-Dimensional Surface Displacements from InSAR Measurements: A Review». *Earth-Science Reviews* 133 : 1–17. https://doi.org/10.1016/j.earscirev.2014.02.005.

Huete, A.R. (1988). «A Soil-Adjusted Vegetation Index (SAVI)». *Remote Sensing of Environment* 25, fasc. 3: 295–309. https://doi.org/10.1016/0034-4257(88)90106-X.

ICOMOS. (1964). The Venice charter for the conservation and restoration of monuments and sites. Paris.

ICOMOS (1990). The charter for the protection and management of the archaeological heritage. Paris.

ICOMOS. (1994). The Nara document on authenticity. Paris.

ICOMOS. (2002). Principles for the conservation of heritage sites in China. Los Angeles: The Getty Conservation Institute.

ICOMOS. (2021). Guidelines on Fortifications and Military Heritage: Final draft for distribution to the ICOMOS membership in view of submission for adoption to the 2021 Annual General Assembly (GA 2021 6-1, Ver. 04/30/2020). [PDF]. Retrieved from document URL: AGA_202111_61_ICOMOS_Guidelines_Fortifications _MilitaryHeritage_2021_EN.pdf (Accessed: September 2023).

International Committee of the Red Cross. (n.d.). Rule 17. https://ihl-databases.icrc.org/en/customary-ihl/v1/rule17. Accessed October 2023.

Interpol. Creating a National Cultural Heritage Unit. (2019). The value of a national unit dedicated to fighting crimes against cultural heritage and the illicit traffic of cultural property. https://www.journalchc.com/wp-content/uploads/2020/09/Creating-National-Cultural-Heritage-Unit-2019-01-EN-LR.pdf. Accessed October 2023.

Isakhan, Benjamin, e Sofya Shahab. (2020). «The Islamic State's Destruction of Yezidi Heritage: Responses, Resilience and Reconstruction after Genocide». *Journal of Social Archaeology* 20, n. 1: 3–25. https://doi.org/10.1177/1469605319884137.

Jaafar, H. & Woertz, Eckart. (2016). Agriculture as a funding source of ISIS: A GIS and remote sensing analysis. Food Policy. 64. 14-25. 10.1016/j.foodpol.2016.09.002.

Joint Force Quarterly (JFQ). (2014). Resilient command and control, diversity in PME, medical diplomacy. *Joint Force Quarterly*, 74(3). Retrieved from http://ndupress.ndu.edu Issue 74, 3rd Quarter 2014

Juhász, Attila. (2007). «A Special GIS Application – Military Historical Reconstruction». *Periodica Polytechnica Civil Engineering* 51, n. 1: 25. https://doi.org/10.3311/pp.ci.2007-1.04.

Juhász, A., e H. Neuberger. (2016). «REMOTELY SENSED DATA FUSION IN MODERN AGE ARCHAEOLOGY AND MILITARY HISTORICAL RECONSTRUCTION». *ISPRS - International Archives of the Photogrammetry, Remote Sensing and Spatial Information Sciences* XLI-B5: 281–86. https://doi.org/10.5194/isprsarchives-XLI-B5-281-2016.

Kathem, M., Antonelli, G. F., Selter, E., Helly, D., & Desmidt, S. (2020). *The role of the European Union in the protection and enhancement of cultural heritage in conflict and post-conflict contexts in the Middle East region: The example of Iraq*. [PDF]. Retrieved from document URL: https://www.cultureinexternalrelations.eu/cier-data/uploads/2020/10/Report-Cultural-Heritage-1Oct2020.pdf (Accessed: September 2023).

Keane David. (2004). The Failure to Protect Cultural Property in Wartime, 14 DePaul J. Art, Tech. & Intell. Prop. L. 1 Available at: https://via.library.depaul.edu/jatip/vol14/iss1/2

Khalaf, Roha W. (2017). «A Viewpoint on the Reconstruction of Destroyed UNESCO Cultural World Heritage Sites». *International Journal of Heritage Studies* 23, n. 3: 261–74. https://doi.org/10.1080/13527258.2016.1269239.

Klemmt, Hans-Joachim, Rudolf Seitz, e Christoph Straub. (2020). «Application of Haralick's Texture Features for Rapid Detection of Windthrow Hotspots in Orthophotos». *Forests* 11, fasc. 7: 763. https://doi.org/10.3390/f11070763.

Knauer, Birgit. (2023). «From Reconstruction to Urban Preservation: Negotiating Built Heritage After the Second World War». *Urban Planning* 8, n. 1. https://doi.org/10.17645/up.v8i1.6133.

Krieger, Gerhard, Irena Hajnsek, Konstantinos Panagiotis Papathanassiou, Marwan Younis, e Alberto Moreira. (2010). «Interferometric Synthetic Aperture Radar (SAR) Missions Employing Formation Flying». *Proceedings of the IEEE* 98, fasc. 5: 816–43. https://doi.org/10.1109/JPROC.2009.2038948.

Krzyżanowska, Natalia. (2016). «The Discourse of Counter-Monuments: Semiotics of Material Commemoration in Contemporary Urban Spaces». *Social Semiotics* 26, fasc. 5: 465–85. https://doi.org/10.1080/10350330.2015.1096132.

Koskinen-Koivisto, Eerika. (2023). Contested and Ambivalent Heritage: Revisiting Responses to the Second World War Heritage of Finnish Lapland from the Perspective of Affects. 10.24834/isbn.9789178773862.

Kossiakoff Megan. (2004).The Art of War: The Protection of Cultural Property during the "Siege" of Sarajevo (1992-95), 14 DePaul J. Art, Tech. & Intell. Prop. L. 109.

Krauss, J. (n.d.). CULTURAL HERITAGE IN CONFLICT & POST-CONFLICT SETTINGS: A WEAPON FOR WAR & A TOOL FOR PEACE. [PDF]. Retrieved October 2023, from https://law.wm.edu/academics/intellectuallife/researchce nters/postconflictjustice/student-programs/student-international-papers/papers/cultural-heritage-in-conflict--post-conflict-settings-.pdf

Langfield Michele, Logan William and Craith Nic Máiréad. (2010). Cultural Diversity, Heritage and Human Rights. *Key Issues in Cultural Heritage.* Routledge Taylor & Francis Group.

Leturcq J. Gabriel. (2009). "Heritage-making and Policies of Identity in the "Post-conflict Reconstruction" of Sudan", *Égypte/Monde arabe* [Online], 5-6 |, Online since 31 December 2010, connection on 07 July 2022. URL: http://journals.openedition.org/ema/2904 ; https://doi.org/10.4000/ema.2904

Legnér, Mattias. (2018). «Post-Conflict Reconstruction and the Heritage Process». *Journal of Architectural Conservation* 24, n. 2: 78–90. https://doi.org/10.1080/13556207.2018.1463663.

Legnér, M. (2022). The protection of movable cultural property in wartime: Pre-conflict planning in Sweden. International Journal of Cultural Property, 29(3), 265–281. https://doi.org/10.1017/s0940739122000212

Lin, e Yuanzhi Zhang. (2011). «Urban Heat Island Analysis Using the Landsat TM Data and ASTER Data: A Case Study in Hong Kong». *Remote Sensing* 3, fasc. 7: 1535–52. https://doi.org/10.3390/rs3071535.

Li, Zhao-Liang, Hua Wu, Si-Bo Duan, Wei Zhao, Huazhong Ren, Xiangyang Liu, Pei Leng, et al. (2023). «Satellite Remote Sensing of Global Land Surface Temperature: Definition, Methods, Products, and Applications». *Reviews of Geophysics* 61, fasc. 1: e2022RG000777. https://doi.org/10.1029/2022RG000777.

Silliman, Stephen W. (2007). «Archaeology as a Tool of Civic Engagement. Barbara J. Little and Paul A. Shackel, Editors. AltaMira Press, Lanham, MD. 286 Pp. $29.95 (Paper), ISBN-13 978-0-7591-1060-1.» *American Antiquity* 73, fasc. 4 (ottobre 2008): 794–95. https://doi.org/10.1017/S0002731600047442.

Lixinski, L., & Schreiber, L. (n.d.). The limits of framing in international law: the shortcomings of international heritage protection in the ISIS conflicts. Adelaide Law School Research Unit on Military Law and Ethics. RUMLAE Research Paper No. 17-04.

LIU, H.Q. and HUETE, A.R., (1995). A feedback based modification of the NDVI to minimize canopy background and atmospheric noise. IEEE Transactions on Geoscience and Remote Sensing, 33, pp. 457–465.

Lo Brutto, M., & Fazio, L. (2020). 3D survey for the archaeological study and virtual reconstruction of the "Sanctuary of Isis" in the ancient Lilybaeum (Italy). Virtual Archaeology Review, 11(22), 1-14. https://doi.org/10.4995/var.2020.11928

Loulanski, Tolina. (2006). «Revising the Concept for Cultural Heritage: The Argument for a Functional Approach». *International Journal of Cultural Property* 13, n. 02. https://doi.org/10.1017/S0940739106060085.

Lowry, J. (2022). Disputed Archival Heritage. Routledge. https://doi.org/10.4324/9781003057765

Manacorda, S., & Visconti, A. (2013). Protecting cultural heritage as a common good of humanity: A challenge for criminal justice. In Proceedings of the *International Conference on "Protecting Cultural Heritage as a Common Good of Humanity: A Challenge for Criminal Justice"*. ISPAC. International Scientific and Professional Advisory Council of the United Nations Crime Prevention and Criminal Justice Programme.

Margottini, C. (Ed.). (2014b). Properties of local material. In: After the destruction of Giant Buddha statues in Bamiyan (Afghanistan) in 2001: A UNESCO's emergency activity for the recovering and rehabilitation of cliff and niches (pp. 153–171). New York: Springer.

Mather, Paul M., e Magaly Koch. (2011). *Computer Processing of Remotely-Sensed Images: An Introduction*. 1ª ed. Wiley. https://doi.org/10.1002/9780470666517.

McDonald, L. (1998). Restitution of archives: Archival claims, legal issues. In Proceedings of the twenty-ninth, thirtieth and thirty-first *International Conference of the Round Table on Archives*. Special Issue JANUS (pp. 209-268). International Council on Archives.

McKenna, Phillip, Stuart Phinn, e Peter Erskine. (2018). «Fire Severity and Vegetation Recovery on Mine Site Rehabilitation Using WorldView-3 Imagery». *Fire* 1, fasc. 2: 22. https://doi.org/10.3390/fire1020022.

Meyer, Susanne Adina. (2013). «Are there various Riegls? Museo, storia dell'arte e conservazione in Alois Riegl». *IL CAPITALE CULTURALE. Studies on the Value of Cultural Heritage*, 199-210 Paginazione. https://doi.org/10.13138/2039-2362/614.

Ministero della Cultura, Direzione generale Educazione, ricerca e istituti culturali. (2016). Tutelare il Patrimonio – Il ruolo del TPC nella tutela del patrimonio culturale. Retrieved October 2023, from https://dgeric.cultura.gov.it/tutelare-il-patrimonio-il-ruolo-del-tpc-nella-tutela-del-patrimonio-culturale/

Ministero della Cultura. (2023). Tutelare il Patrimonio – Il ruolo del TPC nella tutela del patrimonio culturale. Attività formativa riservata al personale MiC. DIREZIONE GENERALE EDUCAZIONE, RICERCA E ISTITUTI CULTURALI. https://dgeric.cultura.gov.it/en/corsi-di-formazione/il-ruolo-del-tpc-nella-tutela-del-patrimonio-culturale/ (Accessed October 2023).

Moxham, Oliver. (2023). «Camouflaged War Heritage: Brecciated War Heritage Sites in Kyoto». In *War Memory and East Asian Conflicts, 1930–1945*, a cura di Eveline Buchheim e Jennifer Coates, 95–131. Cham: Springer International Publishing. https://doi.org/10.1007/978-3-031-23918-2_5.

Muller, N. (2015). Heritage under attack. DW. Retrieved October 2023, from https://www.dw.com/en/italy-appeals-for-un-force-to-protect-heritage-sites-from-islamic-state-siege/a-18331370

Mumtaz, Faisal, Yu Tao, Gerrit De Leeuw, Limin Zhao, Cheng Fan, Abdelrazek Elnashar, Barjeece Bashir, et al. (2020). «Modeling Spatio-Temporal Land Transformation and Its Associated Impacts on Land Surface Temperature (LST)». *Remote Sensing* 12, fasc. 18 : 2987. https://doi.org/10.3390/rs12182987.

Murphy, K. (2000). Memory and modernity: Viollet-le-Duc at Vézelay. University Park: Pennsylvania State University Press.

Murphy, D. (2001). Slowly, families accept the ruins as burial ground. The New York Times, B1, B10.

Nagaoka, M. (2020). The Future of the Bamiyan Buddha Statues. In The Future of the Bamiyan Buddha Statues: Heritage Reconstruction in Theory and Practice. UNESCO Publishing. https://doi.org/10.1007/978-3-030-51316-0_17

Ngoepe, Mpho, e Lekoko Kenosi. (2022). «Confronting Jenkinson's Canon: Reimagining the 'Destruction and Selection of Modern Archives' through the Auditor-General of South Africa's Financial Audit Trail». *Archives and Records* 43, fasc. 2: 166–76. https://doi.org/10.1080/23257962.2022.2048639.

Osmanoglu, Batuhan, Timothy H. Dixon, e Shimon Wdowinski. (2014). «Three-Dimensional Phase Unwrapping for Satellite Radar Interferometry, I: DEM Generation». *IEEE Transactions on Geoscience and Remote Sensing* 52, fasc. 2: 1059–75. https://doi.org/10.1109/TGRS.2013.2247043.

O'Keefe, R., Péron, C., Musayev, T., Ferrari, G. (2016). Protection of Cultural Property Military Manual. United Nations Educational, Scientific and Cultural Organization & International Institute of Humanitarian Law. Paris, France; Sanremo, Italy. ISBN: 978-92-3-100184-0. Available at https://unesdoc.unesco.org/ (Accessed: September 2023).

Ostwald, J. (2007). Vauban under siege. Engineering efficiency and Martial Vigor in the War of the Spanish Succession. The Netherlands: Brill Academic.

Parrulli, F. (2018). Fragilità dei Beni Culturali – il lavoro del Comando Carabinieri per la Tutela del Patrimonio Culturale. Kunsthistorisches Institut in Florenz – Max-Planck-Institut. Retrieved October 2023, from https://www.khi.fi.it/it/aktuelles/veranstaltungen/2018/05/parrulli-fragilita-dei-beni-culturali.php

Petrauskas, Gediminas & Petrauskienė, Aistė & Vaitkevičius, Vykintas. (2018). Archaeology of Modern Conflict: The War after the War in Lithuania and Battle of Užpelkiai Forest, 1949.

Petzet, M. (2009b). Anastylosis or reconstruction – Considerations on a conservation concept for the remains of the Buddhas of Bamiyan (2002), pp. 46–51. In Petzet, M. (Ed.) (2009), The Giant Buddhas of Bamiyan, Safeguarding the Remains. Berlin: Bässler.

Pietroni, Eva, e Daniele Ferdani. (2021). «Virtual Restoration and Virtual Reconstruction in Cultural Heritage: Terminology, Methodologies, Visual Representation Techniques and Cognitive Models». *Information* 12, fasc. 4: 167. https://doi.org/10.3390/info12040167.

Pike, Richard J. (1988). «The Geometric Signature: Quantifying Landslide-Terrain Types from Digital Elevation Models». *Mathematical Geology* 20, fasc. 5: 491–511. https://doi.org/10.1007/BF00890333.

Poulain, Maxime, Marc Brion, e Arne Verbrugge, a c. di. 2022. *The Archaeology of Conflicts: Early modern military encampments and material culture*. First. BAR Publishing. https://doi.org/10.30861/9781407359618.

Regional Conference on Authenticity and Historic Reconstruction in Relationship with Cultural Heritage. (2000). Riga Charter on Authenticity and Historic Reconstruction in Relationship with Cultural Heritage, Riga.

Rennie, K. (2021). Index. The Destruction and Recovery of Monte Cassino, 529–1964</i> (pp. 241-246). Amsterdam University Press.

Renshaw, Layla. (2013): *The Archaeology and Material Culture of Modern Military Death*. Oxford University Press. https://doi.org/10.1093/oxfordhb/9780199569069.013.0042.

Richards, J., Brimblecombe, P. (2022). The transfer of heritage modelling from research to practice. *Herit Sci* **10**, 17. https://doi.org/10.1186/s40494-022-00650-4

Ritchey, T. (2006). «Problem Structuring Using Computer-Aided Morphological Analysis». *Journal of the Operational Research Society* 57, fasc. 7: 792–801. https://doi.org/10.1057/palgrave.jors.2602177.

Rouse JW, Haas RH, Schell JA, Deering DW (1974). Monitoring vegetation systems in the Great Plains with ERTS. Proc Third Earth Resources Technology Satellite-1 Symp, December 10–15 1974, Greenbelt, MD, 3:301–317, NASA, Washington, D.C.

Rubio-Campillo, Xavier, Francesc Xavier Hernàndez Cardona, e Maria Yubero-Gómez. (2015). «The Spatiotemporal Model of an 18th-Century City Siege». *Social Science Computer Review* 33, fasc. 6: 749–65. https://doi.org/10.1177/0894439314558559.

Scammell R. (2015). Create UN military unit to protect ancient sites from ISIS, says Italy. The Guardian. https://www.theguardian.com/science/2015/mar/19/create-un-military-unit-to-protect-ancient-sites-from-isis-says-italy

Scott, D. D., & McFeaters, A. P. (2010). The Archaeology of Historic Battlefields: A History and Theoretical Development in Conflict Archaeology. Journal of Archaeological Research, 19(1), 103–132. https://doi.org/10.1007/s10814-010-9044-8

Schofield, John. (2009). «Introduction Considering Virilio's (1994) Bunker Archeology». In *Aftermath*, di John Schofield, 1–13. New York, NY: Springer New York. https://doi.org/10.1007/978-0-387-88521-6_1.

Schwellenbach, Iris, Klaus-G. Hinzen, Gesa Maria Petersen, e Carla Bottari. (2020). «Combined Use of Refraction Seismic, MASW, and Ambient Noise Array Measurements to Determine the near-Surface Velocity Structure in the Selinunte Archaeological Park, SW Sicily». *Journal of Seismology* 24, fasc. 4 : 753–76. https://doi.org/10.1007/s10950-020-09909-4.

Shackel, P., & Chambers, E. (2004). Places in mind. Public archaeology as applied anthropology. New York: Routledge

Sidorov, Grigori, Alexander Gelbukh, Helena Gómez-Adorno, e David Pinto. (2014). «Soft Similarity and Soft Cosine Measure: Similarity of Features in Vector Space Model». *Computación y Sistemas* 18, fasc. 3. https://doi.org/10.13053/cys-18-3-2043.

Sospedra-Roca, R.afael, Francesc Xavier Hernàndez-Cardona, Isabel Boj-Cullell, e David Íñiguez. «Virtual Approach to a Battlefield: Fatarella Ridge 1938. Spanish Civil War». *Cogent Arts & Humanities* 10, fasc. 1 (31 dicembre 2023): 2172807. https://doi.org/10.1080/23311983.2023.2172807.

Sozinov, P.A., G.I. Andreev, V.A. Tikhomirov, e M.E. Zamarin. (2023). «The concept of protecting a multifunctional aircraft with an electronic warfare system». *Radioengineering* 10. https://doi.org/10.18127/j00338486-202310-01.

Stanley-Price, N. (Ed.). (2005). Cultural heritage in postwar recovery. Papers from the ICCROM FORUM held on October 4-6, 2005. ICCROM Conservation Studies. ICCROM.

Stig Sørensen, M. L., & Viejo-Rose, D. (2015). War and Cultural Heritage: Biographies of Place. Cambridge: Cambridge University Press.

Stone, Peter. (2022). «Preface: The Blue Shield and the Protection of the World's Cultural Property – Preparing in Peace for Conflict». In *Safeguarding Cultural Property and the 1954 Hague Convention*, a cura di Emma Cunliffe e Paul Fox, 1º ed., xvii–xxii. Boydell and Brewer Limited,. https://doi.org/10.1017/9781800104273.001.

Stovel, H. (1998). Risk preparedness: A management manual for world cultural heritage. ICCROM. ISBN 92-9077-152-6. International Centre for the Study of the Preservation and Restoration of Cultural Property.

Sun, Xinyao, Aaron Zimmer, Navaneeth Kamballur Kottayil, Subhayan Mukherjee, Parwant Ghuman, e Irene Cheng. (2023). «A Benchmark InSAR Simulator for Phase Filtering and Coherence Estimation». In *Selected Studies in Geotechnics, Geo-Informatics and Remote Sensing*, a cura di Zeynal Abiddin Ergüler, Riheb Hadji, Helder I. Chaminé, Jesús Rodrigo-Comino, Amjad Kallel, Broder Merkel, Mehdi Eshagh, et al., 11–13. Advances in Science, Technology & Innovation. Cham: Springer Nature Switzerland. https://doi.org/10.1007/978-3-031-43759-5_3.

Szabó, Szilárd, Zoltán Gácsi, e Boglárka Balázs. (2016). «Specific features of NDVI, NDWI and MNDWI as reflected in land cover categories». *Landscape & Environment* 10, fasc. 3–4: 194–202. https://doi.org/10.21120/LE/10/3-4/13.

Tarquini S., I. Isola, M. Favalli, A. Battistini, G. Dotta (2023). TINITALY, a digital elevation model of Italy with a 10 meters cell size (Version 1.1). Istituto Nazionale di Geofisica e Vulcanologia (INGV). https://doi.org/10.13127/tinitaly/1.1.

Tarquini, Simone, e Luca Nannipieri. (2017). «The 10 M-Resolution TINITALY DEM as a Trans-Disciplinary Basis for the Analysis of the Italian Territory: Current Trends and New Perspectives». *Geomorphology* 281: 108–15. https://doi.org/10.1016/j.geomorph.2016.12.022.

Toubekis, G., Mayer, I., Döring-Williams, M., Maeda, K., Yamauchi, K., Taniguchi, Y., Morimoto, S., Petzet, M., Jarke, M., & Jansen, M. (2011). Preservation and management of the UNESCO World Heritage Site of Bamiyan: Laser SCAN documentation and virtual reconstruction of the destroyed Buddha fgures and the archaeological remains. In E. Stylianidis, P. Patias, & M. Q. Santana (Eds.), CIPA Heritage documentation: Best practise and applications, Series 1, 2007 & 2009 (pp. 93–100). DOI: 10.18154/RWTH-CONV-185618

UNESCO. (2015). *State of conservation of World Heritage properties*. World Heritage Committee, Thirty-ninth session, Bonn, Germany. Document code: WHC-15/39.COM/7. Available at https://unesdoc.unesco.org/ (Accessed: September 2023).

UNESCO Kabul. (2016). Draft concept note. The future of the Bamiyan Buddha statues: Technical considerations & potential effects on authenticity and outstanding universal value

UNESCO. (2017). UNESCO Heritage Director calls on Armed Forces to Help in Safeguarding Measures. Retrieved October 2023, from https://whc.unesco.org/en/news/1646

UNESCO & UNITAR. (2018). Five years of conflict: The state of cultural heritage in the Ancient City of Aleppo; A comprehensive multi-temporal satellite imagery-based damage analysis for the Ancient City of Aleppo. Paris, France; Geneva, Switzerland. ISBN: 978-92-3-100284-7. Available at https://unesdoc.unesco.org/ark:/48223/pf0000265826 (Accessed: September 2023).

UNESCO (2018). Background Document on the Challenges of World Heritage Recovery – The Refection on Reconstruction within World Heritage Properties as a Complex Multi-disciplinary Process, Paris.

UNESCO. (2018c). Warsaw recommendation on recovery and reconstruction of cultural heritage. Paris: UNESCO

UNESCO. (2023). Examination of the draft Model Provisions on the Prevention and Fight Against the Illicit Trafficking of Cultural Property. Meeting of States Parties to the Convention on the Means of Prohibiting and Preventing the Illicit Import, Export and Transfer of Ownership of Cultural Property, 7th, Paris. Document code: C70/23/7.MSP/8. Available at https://unesdoc.unesco.org/ark:/48223/pf0000385247 (Accessed: September 2023).

UNESCO. (2023). Meeting of States Parties to the Convention on the Means of Prohibiting and Preventing the Illicit Import, Export and Transfer of Ownership of Cultural Property. Examination of the draft Model Provisions on the Prevention and Fight Against the Illicit Trafficking of Cultural Property. Seventh Meeting. Paris: UNESCO. Document code: C70/23/7.MSP/8. Available at https://unesdoc.unesco.org/ark:/48223/pf0000385247 (Accessed: September 2023).

United Nations. (2017). Security Council condemns destruction, smuggling of cultural heritage by terrorist groups, unanimously adopting Resolution 2347. Retrieved October 2023, from Security Council Condemns Destruction, Smuggling of Cultural Heritage by Terrorist Groups, Unanimously Adopting Resolution 2347 (2017) | UN Press

Unraveling the Complexities of Land Transformation and Its Impact on Urban Sustainability through Land Surface Temperature Analysis». *Applied Geomatics* 15, fasc. 3: 719–41. https://doi.org/10.1007/s12518-023-00521-y.

Uys, Duan. (2016). «InSAR: An Introduction». *Preview* 2016, fasc. 182 : 43–48. https://doi.org/10.1071/PVv2016n182p43.

Viejo-Rose, Dacia. (2013). «Reconstructing Heritage in the Aftermath of Civil War: Re-Visioning the Nation and the Implications of International Involvement». *Journal of Intervention and Statebuilding* 7, n. 2: 125–48. https://doi.org/10.1080/17502977.2012.714241.

Vincent, L.M., & Soille, P. (1991). Watersheds in Digital Spaces: An Efficient Algorithm Based on Immersion Simulations. *IEEE Trans. Pattern Anal. Mach. Intell., 13*, 583-598.

Wahba, S., Bandarin, F., Eiweida, A., Assomo, L., Dubois, D., Iamandi, C., Brotsis, C., Amirtahmasebi, R., Chun, Y., Garcia, B., Ugarte, S., & Massali, I. (2018*). Culture in City Reconstruction and Recovery*. United Nations Educational, Scientific and Cultural Organization (UNESCO) and The World Bank. ISBN 978-92-3-100288-5. [Open Access License: Attribution-ShareAlike 3.0 IGO (CC-BY-SA 3.0 IGO)].

Weiss, T. G., & Connelly, N. (2020). Cultural Cleansing and Mass Atrocities: Protecting Cultural Heritage in Armed Conflict Zones. J. Paul Getty Trust Occasional Papers in Cultural Heritage Policy. J. Paul Getty Trust. eISBN: 978-1-60606-672-0. Available at: https://www.getty.edu/publications/pdfs/CulturalCleansing_Weiss_Connelly (Accessed: September 2023).

Wu, Songbo, Bochen Zhang, Xiaoli Ding, Lei Zhang, Zhijie Zhang, e Zeyu Zhang. (2023). «Radar Interferometry for Urban Infrastructure Stability Monitoring: From Techniques to Applications». *Sustainability* 15, fasc. 19: 14654. https://doi.org/10.3390/su151914654.

Xu, Hanqiu. (2006). «Modification of Normalised Difference Water Index (NDWI) to Enhance Open Water Features in Remotely Sensed Imagery». *International Journal of Remote Sensing* 27, fasc. 14: 3025–33. https://doi.org/10.1080/01431160600589179.

Xu, Hao, Bao Shu, Qin Zhang, Yuan Du, Jing Zhang, Tuo We, Guohua Xiong, Xiaolei Dai, e Li Wang. (2023). «Site Selection for Landslide GNSS Monitoring Stations Using InSAR and UAV Photogrammetry with Analytical Hierarchy Process». *Landslides*. https://doi.org/10.1007/s10346-023-02188-3.

Yang, Ying-Hui, Hao-Liang Li, Qiang Chen, Jing Chen, Jyr-Ching Hu, Xiao-Yun Li, e Qiang Xu. (2023). «Inferring Faulting Model Using InSAR Deformation Differencing Vector: Application to the 2014 Napa Earthquake». *Journal of Geodesy* 97, fasc. 7: 65. https://doi.org/10.1007/s00190-023-01755-9.

Y., J. Gao, e S. Ni. (2003). «Use of Normalized Difference Built-up Index in Automatically Mapping Urban Areas from TM Imagery». *International Journal of Remote Sensing* 24, fasc. 3: 583–94. https://doi.org/10.1080/01431160304987.

Yun, Jieheerah. (2022). «Bunkers as Difficult Heritage: Imagining Future for Underground Spaces in Seoul». *Journal of Asian Architecture and Building Engineering* 21, fasc. 4: 1211–22. https://doi.org/10.1080/13467581.2021.1941980.

Zaghloul, Amir & Weiss, S.J. & Coburn, William. (2010). Antenna developments for military applications. 25. 41-53.

Zekri, Ahmed Sherif. «Enhancing the Matrix Transpose Operation Using Intel Avx Instruction Set Extension». *International Journal of Computer Science and Information Technology* 6, fasc. 3 (30 giugno 2014): 67–78. https://doi.org/10.5121/ijcsit.2014.6305.

Zhang, Xixiang, Kaiqi Xiao, e Jie Gu. (2022). *Theory to Countermeasures Against New Radars*. Singapore: Springer Nature Singapore. https://doi.org/10.1007/978-981-16-6715-2.

Zhang, Xin, Jintian Cui, Weisheng Wang, e Chao Lin. (2017). «A Study for Texture Feature Extraction of High-Resolution Satellite Images Based on a Direction Measure and Gray Level Co-Occurrence Matrix Fusion Algorithm». *Sensors* 17, fasc. 7: 1474. https://doi.org/10.3390/s17071474.

Zhao, Jinling, Lei Hu, Yingying Dong, Linsheng Huang, Shizhuang Weng, e Dongyan Zhang. (2021). «A Combination Method of Stacked Autoencoder and 3D Deep Residual Network for Hyperspectral Image Classification». *International Journal of Applied Earth Observation and Geoinformation* 102: 102459. https://doi.org/10.1016/j.jag.2021.102459.

Zhou, Guanhua, Chen Tian, Chunyue Niu, Guifei Jing, Haoyu Miao, e Zhifeng Li. (2023). «Short Time Cloud-Free Image Reconstruction Based on Time Series Images». *IEEE Journal of Selected Topics in Applied Earth Observations and Remote Sensing* 16 : 51–65. https://doi.org/10.1109/JSTARS.2023.3290679.